

An Advanced Glazing System

Izaac Bailey

A thesis submitted to Auckland University of Technology
in fulfilment of the requirements for the degree of
Master of Engineering (ME)

2022

Abstract

Building-integrated photovoltaics (BIPV) have the potential to rapidly decarbonize new and existing building stock, to accelerate the development of BIPV new avenues for manufacturing must be explored that lower the barrier to entry, improve aesthetics, and reduce end-user costs.

This research aims to investigate whether semi-transparent glass-glass BIPV modules can be manufactured within a laminated glass production line using conventional glass lamination equipment.

An investigation of laminated glass manufacturing and commercial photovoltaic technologies was conducted with specific focus on the fabrication processes used to create transparency in commercial and emerging photovoltaics. The relative advantages of each technology were assessed with respect to their performance as multi-functional BIPV devices as well as the unique manufacturing challenges that must be overcome to allow parallel production of both BIPV devices and laminated glasses.

The international and local standards, guidelines and design procedures pertaining to the design of glass-glass building integrated photovoltaics at the module level were analysed and an initial prototype was designed with respect to these standards. Fabrication was carried out using vacuum bag only process by a local laminated glass manufacturer,

A testing methodology using dark I-V curve analysis was developed to extract the photovoltaic cells electrical parameters and determine if the lamination process was negatively affecting the cells performance. Dark I-V curve analysis proved to be a simple and cost effective method for assessing the condition of photovoltaic cells before and after lamination.

Experimental results revealed that base lamination parameters caused mechanical damage to the photovoltaic cells during lamination, evidence in literature determines the two most likely causes to be cell bending stress induced during lamination warm-up stage, and non-uniform thermal contraction during laminate cool down.

This research concludes that single-chamber vacuum bag only lamination of glass-glass crystalline silicon BIPV modules requires modification to the process parameters in order to prevent mechanical cell damage, further work is needed to verify the effectiveness of the proposed process alterations.

Table of Contents

Abstract.....	1
Table of Contents	2
List of Figures.....	5
List of Tables	9
Attestation of Authorship.....	11
Acknowledgements	12
Intellectual Property Rights.....	12
COVID-19 Impact Statement	13
1 Introduction.....	14
1.1 Global Energy Status	14
1.2 Building and Construction Emissions.....	15
1.3 Building Integrated Photovoltaics.....	16
1.3.1 BIPV Applications	17
1.3.2 Glass-glass BIPV	19
1.4 Research Motivation and Objectives	20
1.5 Thesis Layout.....	21
2 Glass Lamination	22
2.1 Float glass	22
2.1.1 Heat Treated Glass	23
2.2 Laminated Glass.....	24
2.2.1 Interlayers	25
2.2.2 Shear Transfer	26
2.2.3 Manufacturing Processes	27
2.3 Glass-glass Photovoltaic Lamination.....	29
2.3.1 Encapsulants	29
2.3.2 Lamination Process	31
3 Crystalline Silicon Photovoltaics	33
3.1 Cell Technology	33

3.2	Cell Interconnection.....	34
3.3	Manufacturing Process.....	38
3.4	Semi-Transparent Crystalline Silicon Modules	40
3.4.1	Spatial Segmentation.....	41
3.4.2	Luminescent Solar Concentrator.....	43
4	Thin-film Photovoltaics	45
4.1	Film Structure and Manufacturing.....	45
4.1.1	Amorphous Silicon	48
4.1.2	Cadmium Telluride	50
4.1.3	Copper Indium Gallium Selenide	51
4.2	Semi-Transparent Thin-Film Photovoltaics.....	52
4.2.1	Aperture Type	52
4.2.2	Ultra-Thin Film.....	54
4.2.3	Selective Absorptance.....	55
5	BIPV Performance & Feasibility.....	57
5.1	Power Conversion Efficiency	57
5.2	Temperature Dependence	59
5.3	Irradiance Dependence.....	60
5.3.1	Angle of Incidence.....	60
5.3.2	Low Irradiance & Spectral Response.....	62
5.3.3	Shading	64
5.4	Module Degradation	65
5.5	Embodied Energy and Emissions	67
5.6	Manufacturing Feasibility	68
5.6.1	Crystalline Silicon.....	68
5.6.2	Copper Indium Gallium Selenide	68
5.6.3	Cadmium Telluride	69
5.6.4	Amorphous Silicon	70
5.7	Summary	71
6	Prototype Development	72

6.1	BIPV Compliance and Guidelines	72
6.1.1	Laminated Glass Design Methods	74
6.2	Prototype Design.....	76
6.2.1	Module Type Classification	76
6.2.2	Insulation Class	77
6.2.3	Photovoltaic Cells	79
6.2.4	Cell Interconnection.....	80
6.2.5	Encapsulant	82
6.2.6	Module Glass	82
6.2.7	Excluded Components	83
6.2.8	Fabrication Procedure	84
7	Experimental Testing.....	85
7.1	Testing Overview.....	85
7.1.1	Prototypes Manufactured	85
7.2	Physical Inspection	87
7.3	Cell Characterization.....	91
7.3.1	Testing Methodology	93
7.3.2	Double-Diode Model	94
7.3.3	Algorithm.....	94
7.3.4	Results.....	98
7.3.5	Discussion	100
7.3.6	Proposed Changes to Methodology	103
8	Conclusions.....	105
8.1	Future Work	105
	References.....	106
A	Market Analysis and Product Overview.....	119
B	Laminated Glass Modelling	122
C	Cell Characterization Results	126

List of Figures

Figure 1: World electricity generation by source (IEA, 2021)	14
Figure 2: Global energy-related CO ₂ emissions share 2020 (UNEP, 2021)	15
Figure 3: Common integration methods for BIPV (Corti et al., 2020)	17
Figure 4: Conventional vs glass-glass photovoltaic module (Sinha et al., 2021)	19
Figure 5: BIPV market forecast by segment (Ballif et al., 2018).....	20
Figure 6: Float glass process (G.James Glass & Aluminium, 2007)	22
Figure 7: Stress field of heat-strengthened glass (G.James Glass & Aluminium, 2007)	23
Figure 8: Example configurations of PVB laminated glass (Carrot et al., 2015)	24
Figure 9: Laminated glass shear transfer behaviour (Kuntsche et al., 2019)	27
Figure 10: Nip-roll & autoclave process for laminated glass (Carrot et al., 2015)	28
Figure 11: Oven temperature profile during VBO lamination (Folienwerk Wolfen, 2014).	29
Figure 12: Cross section of glass-glass module with edge seal	31
Figure 13: Double-chamber laminator (Drabczyk & Panek, 2012).....	32
Figure 14: Appearance of mono- and poly-crystalline silicon PV cell (Smith et al., 2021).	33
Figure 15: 5BB and 12BB solar cells with discrete rear contacts (ENF Solar, n.d.)	35
Figure 16: Conventional (left) and back contact (right) cell stringing (Mat Desa et al., 2016)..	35
Figure 17: CAD model section depicting bus ribbon connection to the end of a cell sub-string	36
Figure 18: Common 3-string diode topology for 60 cell modules with bypass diode activated (Vieira et al., 2020).	37
Figure 19: Example of alternative interconnect methods for rear contact cells (Borgers et al., 2017)	38
Figure 20: Schematic of a c-Si module turnkey line (Lange et al., 2011)	38
Figure 21: Glass-foil module manufacturing process (Woodhouse et al. 2019).....	40
Figure 22: Spatially segmented c-Si BIPV modules integrated into overhead glazing (K. Lee et al., 2020a; Polysolar., 2021a).....	41
Figure 23: Examples of semi-transparent modules using modified c-Si cells.	42
Figure 24: Examples of PV cells and modules with modified appearances	42

Figure 25: Dual UV/IR absorption LSC schematic	43
Figure 26: Cross-section of a generalised superstrate deposited thin-film PV	45
Figure 27: Superstrate deposited CdTe film structure showing the P1, P2, and P3 laser scribes. (Başol & McCandless, 2014)	46
Figure 28: CIGS scribe lines with individual pulses visible (Rekow et al., 2010)	47
Figure 29: Crystalline and thin-film glass module construction (Carrot et al., 2015).	48
Figure 30: Superstrate deposited micromorph cell structure	49
Figure 31: Standard superstrate deposited CdTe device structure (HRT = High Resistivity Transparent layer)	50
Figure 32: CIGS device structure (Klinkert, 2015).....	51
Figure 33: a-type thin-film BIPV of varying transparencies and colours (Corti et al. 2020)	52
Figure 34: Examples of aperture-type film (a), and effect of removed absorber material on transmittance (b). (Z. Li et al., 2021)	53
Figure 35: Optical comparison of a-type (See-through) and UTF (Translucent) a-Si solar cells (Takeoka et al., 1993)	54
Figure 36: UTF a-Si module with modified colour (Yeop Myong & Won Jeon., 2015).....	55
Figure 37: PCE vs VLT for transparent research cells, indicating the high potential of perovskite and organic cells over the full transparency range. Data from Almora et al. (2020), K. Lee et al. (2020a) & (2020b), Z. Li et al. (2021), and Sidali et al. (2018).....	56
Figure 38: Electricity cost sensitivity of grid-connected BIPV systems (Corti et al., 2020	57
Figure 39: Efficiency data for commercially available semi-transparent PV modules at STC (Data sources listed in Appendix A; Table 21)	58
Figure 40: Example of variation in reflectance (left), and in total received power (right)	61
Figure 41: Contour plot of relative yearly insolation received by orientation and tilt angle in the northern hemisphere (Roberts & Guariento, 2009).....	62
Figure 42: Normalized spectral response of PV technologies	63
Figure 43: Efficiency vs irradiance, parameters from Mavromatakis et al. (2017)	64
Figure 44: Shading effects on generic c-Si vs thin-film modules (Current travels horizontally in the thin-film diagrams so worst case mismatch losses occur in the case on the right)	65

Figure 45: Minimum selling price for commercial module technologies (Smith et al., 2020) ...	69
Figure 46: Creepage (solid line) vs clearance (dotted line) distances between 2 conductors (BSI, 2018a)	78
Figure 47: Locations for minimum creepage distance	79
Figure 48: Prototype cell interconnect 2D CAD drawing with minimum insulation requirements dimensioned	81
Figure 49: Soldered PV cells	84
Figure 50: Defective annealed prototype with fractured glass and disconnected cell area	89
Figure 51: Prototype with minor void defect	90
Figure 52: Prototype module showing edge pinch	90
Figure 53: EL Image of a PV module showing cracks in multiple cells, dark regions indicate inactive areas (Sinha et al., 2021)	92
Figure 54: Dark I-V test circuit configuration	93
Figure 55: Double-diode equivalent circuit with no photo-generated current	94
Figure 56: Regression line for equation 8 using all possible combinations of data pairs to obtain a strong fit	96
Figure 57: Shunt region showing linear relation of approximate shunt current ($I-I_2$) at low voltage, note that ignoring I_1 has negligible effect	97
Figure 58: Fitted curve for prototype D14-T pre-lamination	98
Figure 59: Dark I-V curve before and after lamination	99
Figure 60: Difference in pressure application between VBO single and double-chamber lamination	102
Figure 61: Stress concentration in PV cells during lamination (Song et al., 2018)	103
Figure 62: PV technologies used in commercial STPV products (Table 21)	120
Figure 63: Interlayer materials used in commercial STPV products (Table 21)	120
Figure 64: Interlayer thicknesses in commercial STPV product (Table 21)	121
Figure 65: Polymer stiffness dependence on temperature	122
Figure 66: Shear modulus master curve for EVALAM Visual UV+	124
Figure 67: Shear coefficient vs temperature	124

Figure 68: Stress effective thickness vs temperature 125

Figure 69: Maximum glass stress vs temperature 125

List of Tables

Table 1: BIPV application categories as defined in IEC 63092-1:2020 (IEC, 2020).	18
Table 2: Interlayer properties from literature and product data sheets (Sulkis, 2019; Pujol Group, 2020; Martin et al., 2020; Sinha et al., 2021; Kuraray, 2022)	26
Table 3: STC efficiencies of opaque and commercial transparent PV modules and cells (^[1] Green et al., 2021; ^[2] Table 21).....	58
Table 4: Temperature coefficients and expected power losses of transparent PV products (^[1] Virtuani et al., 2010; ^[2] Table 21)	59
Table 5: PV module durability and average degradation rates	66
Table 6: Warranty provided by encapsulant material for glass-glass semi-transparent PV (Data from Table 21)	66
Table 7: EPBT & embodied CO ₂ equivalent emissions of PV technologies (Ogbomo et al., 2017; Ghosh, 2020).....	67
Table 8: Comparative benefits of PV technologies for BIPV manufacturing.....	71
Table 9: Requirements from IEC 63092-1:2020 for BIPV modules containing at least one glass pane, application categories refer to those in Table 1 (IEC, 2020)	73
Table 10: Summary of key PV standards and guidelines relevant to glass-glass BIPV in NZ...	74
Table 11: Comparison of stress effective design thickness of laminated glass under short term (Standards New Zealand, 2008; Kuntsche et al., 2019).....	75
Table 12: Summary of prototype classification according to IEC 61730-1:2018.....	77
Table 13: Lamination cycle parameters	84
Table 14: Testing methodology	85
Table 15: Prototype identification.....	86
Table 16: List of fabricated prototypes and manufacturing outcomes.....	87
Table 17: Fabricated prototype defects.....	88
Table 18: Measured and expected prototype thicknesses	91
Table 19: Electrical parameters before and after lamination	99
Table 20: Average change in electrical parameters after lamination	100

Table 21: Commercial semi-transparent PV module manufacturers	119
Table 22: Variable and values used in shear bonding calculations.....	123
Table 23: Complete cell characterization results	126

Attestation of Authorship

I hereby declare that this submission is my own work and that, to the best of my knowledge and belief, it contains no material previously published or written by another person (except where explicitly defined in the acknowledgements), nor material which to a substantial extent has been submitted for the award of any other degree or diploma of a university or other institution of higher learning.

Izaac Bailey

A handwritten signature in black ink, appearing to read 'Izaac Bailey', written over a horizontal line.

May 2022

Acknowledgements

I would like to express my gratitude to my supervisor Dr. Timothy Anderson for not only providing me guidance and support throughout this project but for helping me discover my passion in photovoltaics during my undergraduate degree.

I would like to thank Viridian Glass New Zealand for offering this research project and providing manufacturing capabilities, special thanks to Geoff Rasmussen at Viridian for organizing all the prototype fabrication and providing advice and feedback.

I would also like to thank Stephen Hartley at AUT for organizing equipment and laboratory space for the experiments and teaching me how to use all the necessary equipment.

Finally, I would like to thank Callaghan Innovation for providing a grant for this research and giving me the chance to work on such an interesting project, I am very grateful to have had this opportunity.

Intellectual Property Rights

The author of this work acknowledges that any material created in the course of providing the research, whether independently or in collaboration with others, is the exclusive property of Viridian Glass GP Limited.

COVID-19 Impact Statement

Disruptions due to lockdowns affected several key decisions during the development of this research, particularly during the later stages where manufacturing and testing were involved.

Restrictions on access to laboratory space/equipment and manufacturing equipment were in place for a significant period of the research and several delays had to be made to the fabrication, manufacturing and testing of prototypes. Once these activities were able to continue it was in a limited capacity due to the COVID-19 protocols of the relevant entities, as well as reduced access to manufacturer equipment due to changes in production schedules. Furthermore the reduced period of time available for these phases of the project greatly increased the difficulty of dealing with manufacturer errors and delays.

Due to the extended period spent under lockdown PV cell testing methodologies were reassessed and changes were made to utilize only equipment that could be made readily available under the conditions at hand. These testing method alterations were done under the assumption that lockdowns may extend for such a period of time that equipment would need to be used and operated independently off-premises, hence an effort was made to design tests that utilized equipment that could be operated without the assistance of an expert, without additional specialist safety equipment, and in the case of indefinite lockdown periods, could be either delivered to an accessible location, or purchased within the project budget.

This involved both modifying and removing several PV cell testing methodologies from the project plan as they involved equipment that could not reasonably be accessed under the conditions mentioned, primarily these changes were the removal of a tensile load test for assessment of encapsulant adhesion, and alteration of PV cell damage detection from an electroluminescence imaging method to dark I-V.

Despite these changes the testing methodology developed was highly applicable and the restrictions imposed arguably led to the development of a more innovative, cheaper, and more accurate solution for detecting PV cell damage in the form of Dark I-V testing.

In summary the main reduction of the initial scope due to COVID-19 impacts occurred due to a lack of access to both testing and manufacturer equipment both reducing the variety of testing that could be carried out and significantly delaying the production of prototypes. This in turn led to reduced time available to conduct tests, and no opportunities to vary the manufacturing process or design for further prototype development. If this research were to be carried out in full capacity it would be expected to arrive at similar conclusions only with a larger array of supporting evidence.

1 Introduction

1.1 Global Energy Status

The Paris Agreement was adopted in 2015 with the intention of limiting global temperature increase to well below 2 °C compared to pre-industrial levels by reducing the quantity of man-made atmospheric emissions (United Nations Framework Convention of Climate Change [UNFCCC], 2016). Signatories of the treaty agree to set nationally determined contributions (NDCs) to declare their intended emission reduction targets and strategies, as of late 2021 a total of 194 parties have submitted their first NDC with the most frequently mentioned action being the use of renewable energy in the electricity sector (United Nations Environment Programme [UNEP], 2021).

Rapid deployment of renewable energy is a major driving force towards achieving a near carbon neutral energy sector which would be required to meet the current objectives of the Paris Agreement. In the last decade or so global energy generation from renewable sources has increased significantly (See Figure 1), with the electricity generation from hydroelectricity and wind doubling between 2005 and 2019, in the same period photovoltaic (PV) generation has increased by a factor of over 150 due to rapidly increasing efficiencies and decreasing costs, making it a highly competitive source of electricity (International Energy Agency, 2021). An additional 139 GW of PV capacity was deployed in 2020 to reach a total global capacity of 760 GW (Feldman et al., 2021), which accounts for an estimated 3.7% of global electricity generation (Detollenaere et al., 2021), however this number is dwarfed in comparison to the 63% generated from coal, crude oil and natural gas (International Energy Agency [IEA], 2021).

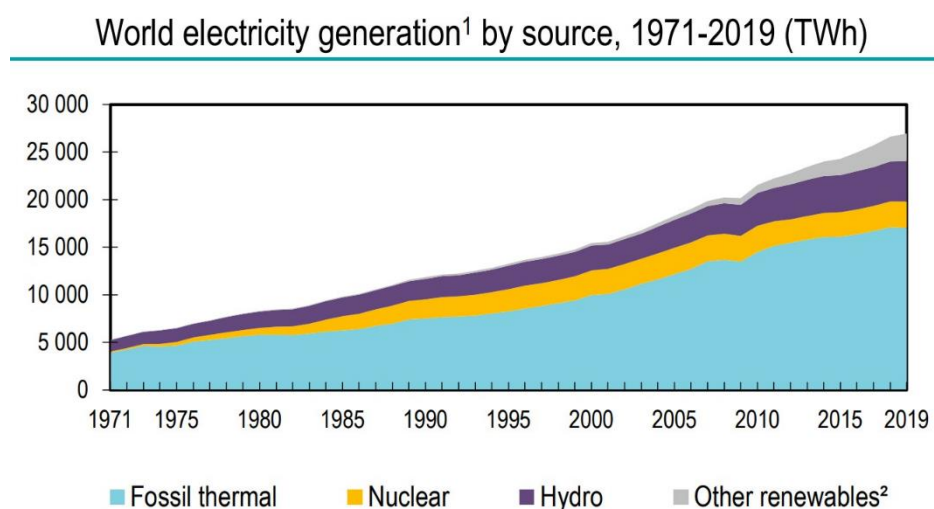


Figure 1: World electricity generation by source (IEA, 2021)

It is vital to fast-track deployment of renewable generation whenever possible, however the task of converting the majority of all global energy consumption to renewable sources is a massive undertaking and may take several decades to fulfil, therefore it is critical to vastly reduce the energy consumption of all industries in the meantime, to limit the emissions produced in the transitional phase while fossil-fuels are still heavily relied on as a primary energy source.

1.2 Building and Construction Emissions

In 2020 the buildings and construction sector accounted for 36% of global energy consumption and 37% of CO₂ emissions (See Figure 2), of which half were indirect emissions from power generation for electricity and heat. Taking immediate action to decarbonize the building and construction sector is critical for achieving the goals of the Paris Agreement, as such the UNFCCC have set goals to halve the emissions of the built environment by 2030 and achieve net zero operational and embodied emissions by 2050 (UNEP, 2021).

Actions targeting emission reductions in the building sector are the second most frequently cited in all currently submitted NDCs and over \$180 billion USD has already been invested into improving building energy efficiency, mostly targeting the reduction of energy and emissions intensity of space heating, cooling and lighting (UNEP, 2021). However, the current rate of improvement falls significantly short of what is necessary to achieve the goals of the UNFCCC, the International Energy Agency (Abergel et al., 2021) reported that building energy intensity (net energy consumed per square metre of floor space) needs to decrease 5 times faster over the next decade than it has in the previous one.

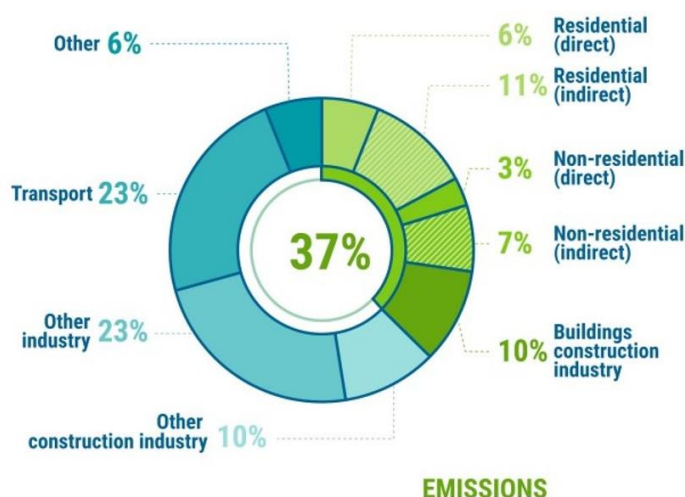


Figure 2: Global energy-related CO₂ emissions share 2020 (UNEP, 2021)

Alongside improvements to energy efficiency of buildings there is significant potential to reduce carbon emissions in the building sector by means of decentralised energy generation. By directly generating some of a building's energy requirement with renewable energy devices

installed on-site the transmission losses of the central grid, which are around 7% in New Zealand (Ministry of Business, Innovation and Employment, 2021), are bypassed and indirect emissions are reduced, while the portion of energy consumption coming from low-emission renewable sources is increased. The installation of on-site generation systems could also increase the portion of national energy consumption from renewable sources at a higher rate due to the faster project turnaround for smaller on-site systems compared to large utility scale systems.

On-site generation in the building sector is best achieved with photovoltaics due to their competitive electricity cost and convenient form factor, however the application of conventional rack-mounted photovoltaics in dense urban areas is limited because the available ground and roof installation areas are insufficient to provide the generation capacity required for high-rise buildings (Meinardi et al., 2017). Therefore the development of photovoltaic devices that can be integrated into not only the roof, but other facets of the building envelope such as windows, cladding and other external features is a critical factor towards reducing carbon emissions from the urban environment, especially for high-rise buildings with large vertical surface areas.

1.3 Building Integrated Photovoltaics

PV devices used in the built environment are classified as building integrated photovoltaics (BIPV) if they are installed as an integral part of a building, provide a building function, and generate energy from solar light or heat, if a BIPV system were to be removed from a building it would need to be replaced by another construction product to maintain the integrity of the buildings functionality (International Electrotechnical Commission [IEC], 2020). Innovations in both the PV and glass industry are allowing for BIPV devices to more closely resemble and function as traditional building materials and are helping to increase the desirability of BIPV systems in some regions. Considerable future growth is expected due to government policies and initiatives and the increasing awareness of green infrastructure (Grand View Research, 2021)

The introduction of national energy and emissions related building policies stemming from the objectives of the Paris agreement could have a large positive influence on local BIPV markets, this impact is evident in Europe where the rapid progression of BIPV technology has largely been driven by the Energy Performance of Buildings Directive (PVSITES, 2016), leading to Europe becoming a core market for BIPV innovation and making up 41.6 % of global roof segment BIPV sales in 2020 (Global Industry Analysts, 2021). As future energy policies become stricter BIPV will likely become a key tool for achieving regulated high energy performance in both new and existing buildings.

1.3.1 BIPV Applications

Photovoltaic devices can be integrated into numerous different products for the building envelope, they are classified below according to some common product archetypes as shown in Figure 3, these product types also fit within application categories that are defined by international standards as shown in Table 1, the application categories are defined by their orientation and accessibility within the building rather than the product type or functionality (IEC, 2020).

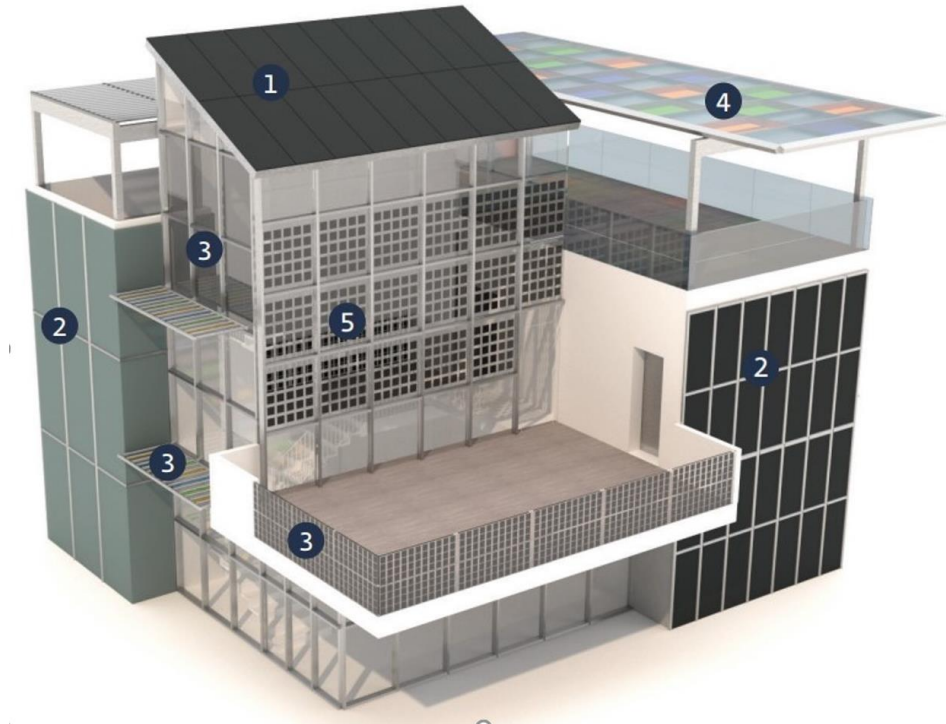


Figure 3: Common integration methods for BIPV (Corti et al., 2020)

1. Roof integrated BIPV: Typically opaque and can be applied in the form of shingles or tiles to form a complete weathertight roof, can be angled or flat. This application has the most variation in module design as there are possibilities for alternate substrates such as flexible foils (Category A/B).
2. Cold façade (Rainscreen): Over-cladding with cavity for ventilation and drainage, the outer wall provides the majority of moisture protection but is not sealed, BIPV can be integrated into the outer cladding. This type of façade is more favourable for BIPV generation as the airgap keeps modules cool and the cladding is typically opaque which allows for the use of conventional PV technologies (Category C).

3. External accessories: External elements such as balconies, parapets, shading systems and partitions. These applications may increase the difficulty in hiding external wiring and power optimizers due to the lack of framing or adjacent material (Category E).
4. Skylights/glazings: Glazing for daylighting in overhead or vertical elements, includes skylights, atria, windows, and insulating glass units (IGUs). Requires some degree of transparency in BIPV products but does not necessitate completely uniform lighting (Categories B/D).
5. Warm façade (Curtain wall): Continuous weather sealed non-ventilated building skin with BIPV integrated into the non-structural outer wall, more challenging integration as the lack of ventilation results in higher operating temperatures which can reduce power output and durability. Additionally both opaque and transparent PV would likely be required for a BIPV curtain wall to provide generation from both the spandrel and vision regions of the façade (Category C).

The BIPV market is currently dominated by roof integrated systems which account for 60% of the market (Grand View Research, 2021), a BIPV product overview by SUSPI (Zanetti et al., 2017) found that about 58% of European BIPV products sampled were roof integrated systems, while the façade systems were classified as predominantly cold façade (13%) and skylights/glazings (12%), with warm façade (7%) and external accessories (6%) proving less common.





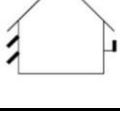
Category A	Sloping, roof-integrated, not accessible from within the building	
Category B	Sloping, roof-integrated, accesible from within the building	
Category C	Non-sloping (vertically) envelope-integrated, not accessible from within the building	
Category D	Non-sloping (vertically) envelope-integrated, accessible from within the building	
Category E	Externally-integrated, accessible or not accessible from within the building	

Table 1: BIPV application categories as defined in IEC 63092-1:2020 (IEC, 2020).

1.3.2 Glass-glass BIPV

In order to increase the available surface area for PV integration the development of BIPV products for all facets of the external building surface is necessary, accordingly BIPV devices must be able to take the place of transparent building materials to allow integration into vision areas of curtain walling and other glazing elements such as skylights and IGUs.

Conventional PV modules are produced by laminating PV cells between a front glass sheet and an opaque polymer backsheet (foil) within a polymeric encapsulant to protect the cells and improve the mechanical properties of the module. The development of bifacial PV cells which can generate energy from the rear-side of the cell necessitated the commercialization of ‘glass-glass’ PV modules, as shown in Figure 4, which have a transparent glass backsheet to allow light transmission and therefore energy generation from the rear of the module.

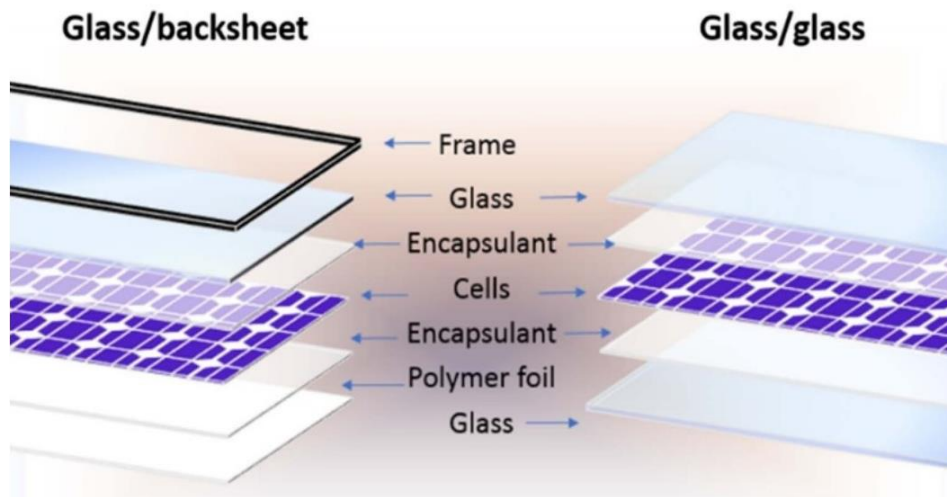


Figure 4: Conventional vs glass-glass photovoltaic module (Sinha et al., 2021)

Despite the increased weight and cost, glass-glass modules exhibit several favourable characteristics compared to conventional glass-foil products that lend themselves well to integration into the built environment, including higher load bearing capabilities, improved environmental resistance, longer module lifespans (Schneller et al., 2016), and the ability to create partially transparent modules via modification of the internal layers.

The appearance of glass-glass BIPV is also highly customizable, colours and patterns can be added to glass-glass modules to create aesthetically pleasing coloured BIPV or even mimic the appearance of other materials to replace opaque cladding elements (Zanetti et al., 2017; Ballif et al., 2018), improving aesthetic appeal and customization options is expected to contribute towards rapid growth of the BIPV glass segment over the next several years, as depicted below in Figure 5 (Grand View Research, 2021).

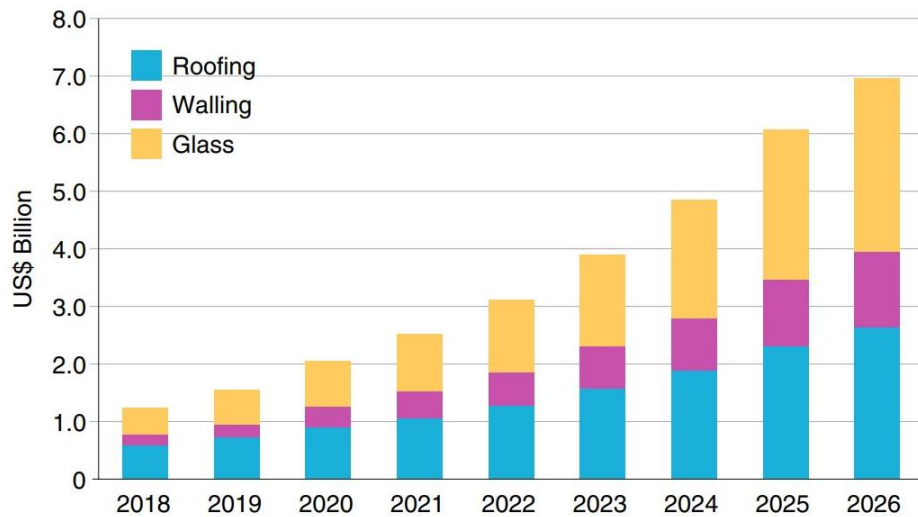


Figure 5: BIPV market forecast by segment (Ballif et al., 2018)

1.4 Research Motivation and Objectives

Conventional PV module manufacturing uses specialized lamination equipment to maximize throughput, it is a capital intensive and highly competitive market to enter, international variations in electricity, land, and labour costs also make it difficult for many countries to achieve the low costs provided by leading PV manufacturers (Woodhouse et al., 2019). With the niche market of glass-glass BIPV there is an opportunity for laminated glass manufacturers to lower the barrier for entry by adapting glass lamination and handling equipment to the manufacture of BIPV and enter a developing adjacent market with high future potential.

This research focuses on the potential for integrating glass-glass BIPV manufacturing into existing laminated-glass production facilities. The primary research question developed for this thesis is:

Can current laminated glass manufacturing systems be adapted to the manufacture of building integrated photovoltaic modules, and if so, what modifications need to be made to the processing?

This work will aim to answer the primary research question as well as provide an overview of BIPV technologies through the following objectives.

- Research and analyse the feasibility, performance, and comparative benefits of current commercial semi-transparent PV technologies and manufacturing techniques for integration into a laminated glass manufacturing line and product range.

- Identify current standards and design procedures applicable to photovoltaics devices and the requirements necessary for certification of glass-glass BIPV products in New Zealand
- Design and fabricate BIPV prototypes using existing laminated glass manufacturing equipment and perform tests on prototypes to evaluate the potential of using laminated glass manufacturing systems to create a functional and compliant BIPV product.

1.5 Thesis Layout

The thesis is divided into the following chapters:

- Chapter 2 provides a brief overview of flat glass and discusses the techniques for laminated glass and for glass-glass PV lamination.
- Chapter 3 introduces crystalline silicon photovoltaics and discusses the potential uses in both transparent and opaque BIPV.
- Chapter 4 discusses commercial thin-film technologies and gives a brief overview of manufacturing procedures and methods of adding transparency.
- Chapter 5 provides a summary of factors affecting the performance of BIPV modules and summarizes the relative manufacturing advantages of each PV technology.
- Chapter 6 covers the detailed design of mini-module glass-glass BIPV prototypes, including details of relevant design considerations, standards and design guidelines.
- Chapter 7 details the experimental testing undertaken to answer the primary research, as well as discussion of the results and proposed future alterations to the methodology.
- Chapter 8 provides conclusions and future work.
- Appendices A through C provide additional calculations and data related to the design, compliance and commercialization of glass-glass BIPV products.

2 Glass Lamination

This chapter covers the basics of glass properties and the manufacturing processes used to create float glass and laminated glass, as well as the methods used in the PV industry to laminate glass-glass photovoltaic modules.

2.1 Float glass

Glass is a hard and brittle amorphous solid which is usually translucent or transparent, it has many desirable properties, including being inert and non-porous, a good electrical and thermal insulator and having high transparency. The most common form of glass is soda-lime glass which is made by fusing silica (from sand), soda ash and limestone, with small amounts of other additives such as recycled glass (cullet). Soda-lime glass has high transparency but exhibits a slight green tinge due to the absorption spectra of iron oxides present in the silica component, a common modification to the glass composition is the use of high-quality grades of silica containing about 90% less iron oxide content than usual, this is done to make low-iron glass which has a much 'whiter' appearance and higher transmittance than regular soda-lime glass.

The majority of flat glass is manufactured by the float glass procedure (Figure 6), which involves floating molten glass over a shallow bath of molten tin to create a flat glass sheet of uniform thickness, with the speed at which the glass is drawn off the tin bath determining the thickness. Once drawn off the float bath the glass travels through a lehr (furnace) where it is annealed by slowly cooling under controlled conditions to remove any residual thermal stresses that may weaken the product (G.James Glass & Aluminium, 2007; Callister & Rethwisch, 2018). The glass is then cut usually using automatic in-line systems that score the glass using a hard-alloy or diamond cutting wheel and break the glass along the score line, followed by edgework to remove defects from the breaks. Cutting can also be done using laser or waterjet cutting, which allows for more complex shapes and cut-outs from the middle of the glass.

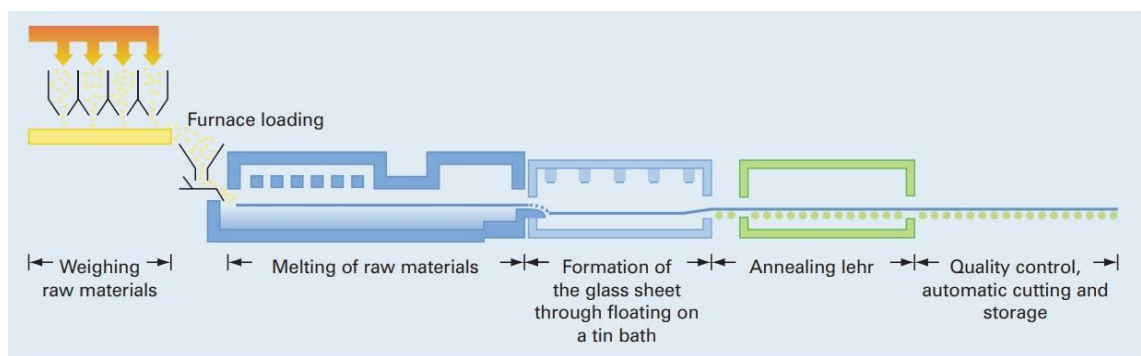


Figure 6: Float glass process (G.James Glass & Aluminium, 2007)

2.1.1 Heat Treated Glass

Glasses primarily fail due to propagation of surface microcracks under tensile load; therefore glasses are significantly stronger in compression as no stress concentration occurs in the surface defects in this loading condition. In order to increase the strength of glass a heat-treatment process can be used in which the glass is heated above its transition temperature to about 620 °C and rapidly cooled to induce residual compressive stresses at the surface of the glass as shown in Figure 7, this compressive stress must be overcome before tensile fracture occur which greatly increases the tensile strength of the glass (G. James Glass & Aluminium, 2007; Callister & Rethwisch, 2018).

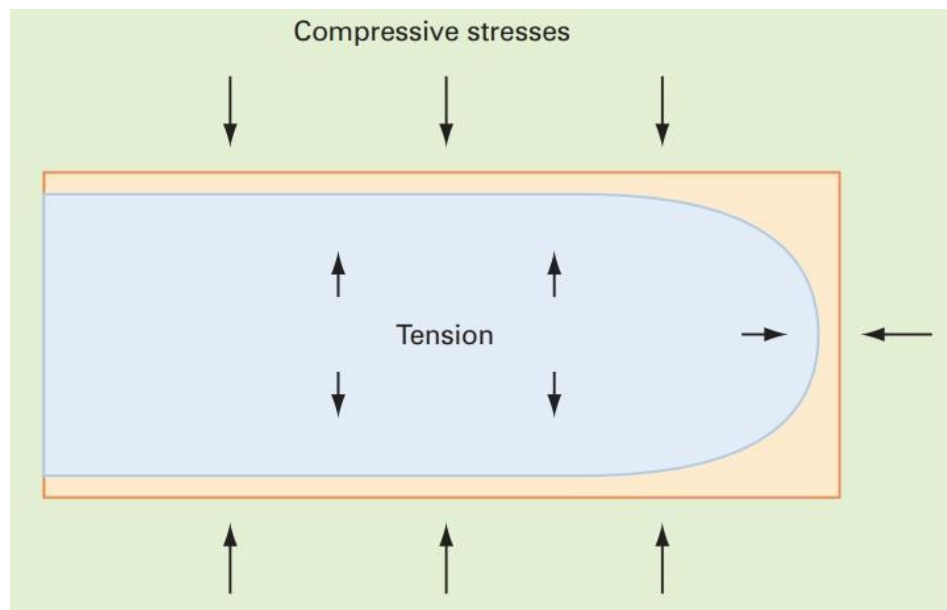


Figure 7: Stress field of heat-strengthened glass (G.James Glass & Aluminium, 2007)

Heat-treated glasses are divided into heat-strengthened and fully toughened (tempered) grades, the difference being the rate of cooling which is applied during the heat-treatment procedure. The faster rate applied during quenching of fully toughened glass results in higher residual stresses and gives it the highest strength, about 3 – 6 times stronger than annealed glass (Callister & Rethwisch, 2018), the high residual stress also has an effect on fracture pattern and causes it to break into small blunt cubical fragments, making it much safer for use in applications where there is a risk of human impact. Heat-strengthened glass is quenched at a slower rate and so is not quite as strong, about 2-3 times that of annealed glass, and also fractures into larger pieces which means it is not classified as a safety glass, it can be consider as having properties intermediate of annealed and tempered glass (G.James Glass & Aluminium, 2007).

There are some limitations to the production of heat-treated glass, the maximum size of tempered glass is limited by the capacity of the heat-treating furnace while a minimum size is imposed by the distance between the rollers which move the glass through the furnace, usually around 300 mm. These rollers also cause a flatness deviation called roller wave, arising from the soft heated glass sagging between the spaces in the rollers, which can create optical distortions in the finished product. Thermally heat treated glasses cannot be cut as a disruption to the surface stress field will cause the glass to shatter, this means any cuts or edge treating must be done prior to heat-treatment.

2.2 Laminated Glass

Laminated glass is manufactured by sandwiching a polymeric interlayer between sheets of glass (See Figure 8) and applying pressure and heat in a controlled manner to remove gases and adhere the interlayer to the glass. The laminate then acts as a composite in which the viscoelasticity of the interlayer allows for improved impact resistance compared to an equivalent thickness of monolithic glass. The elasticity of the interlayer and high adhesion to the glass means that if one or both glass sheets fracture the pieces will likely remain adhered to the interlayer, maintaining some residual strength post-breakage and greatly reducing the safety hazard (Carrot et al., 2015).

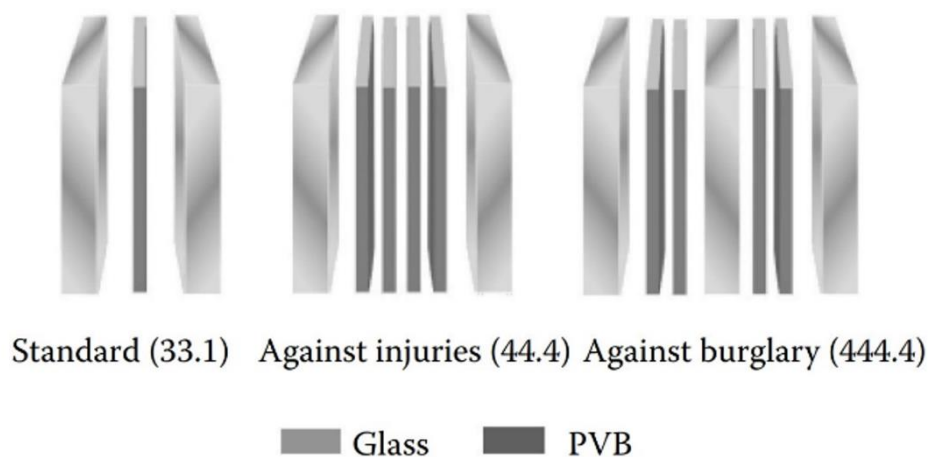


Figure 8: Example configurations of PVB laminated glass (Carrot et al., 2015)

Laminated glass is often used as a safety glass in buildings where there is potential for human impact to reduce the risk of personal harm, or otherwise where improved impact resistance and post-breakage strength are required. Laminated glass can also be used to enhance the environmental barrier of glazing in buildings by reducing the transmission of sound, heat (IR light) and damaging UV radiation into the building interior, these properties can be enhanced by the use of specialized interlayers and/or glass coatings.

2.2.1 Interlayers

Laminated glass is usually manufactured using polyvinyl-butylal (PVB) interlayer, which is used primarily due to its toughness, high adhesion to glass, and excellent optical transmission. PVB was patented in 1935 and has since been the main interlayer for both the automotive and construction glass industries, over time the formulation of PVB has evolved to not only greatly improve its performance but also create specialty grades with unique properties such as increased acoustic attenuation, extra high stiffness, or improved IR absorption (Carrot et al., 2015).

Outside of PVB there are only 2 other interlayers that see any significant use in the laminated glass industry: EVA and Ionomer. The main use of EVA is for frameless glass and/or high humidity environments because it has low water absorption and high adhesion, meaning it can be used without the risk of delamination or edge defects due to moisture penetration. EVA is also well suited for laminating specialty pieces with inserts due its lower melt viscosity allowing it to better flow around the inserts during the lamination process. Ionomer is used for highly blast resistant or structural glass elements due to its exceptional stiffness, which is about 100 times that of standard PVB, its higher glass transition temperature also means that maintains its mechanical properties over a wider range of temperatures (Martín et al., 2020).

Interlayer Property	PVB	EVA	Ionomer
Chemically cross-linking	No	Yes	No
Water absorption 24 hrs immersion	0.5 – 3.6 wt.%	0.15 – 0.55 wt.%	--
Diffusion coefficient (45 °C / 85% RH)	0.25 cm/h ^{1/2}	0.16 cm/h ^{1/2}	0.015 cm/h ^{1/2}
Coefficient of thermal expansion	1.6 – 1.9 10 ⁻⁴ /K	1.6 – 2.0 10 ⁻⁴ /K	1.0 – 1.5 10 ⁻⁴ /K
Glass transition temperature	8 – 47 °C	-77 to -18 °C	55 °C
Light Transmittance	88 – 89 %	90 – 92 %	88 – 89 %
Surface resistivity	10 ¹⁰ – 10 ¹² Ω	10 ¹⁴ Ω	>10 ¹² Ω
Shear modulus (25 °C, 3s load duration)	1.5 – 150 MPa	1.94 MPa	136 – 167 MPa
Shear modulus (50 °C, 3s load)	0.36 – 0.72 MPa	0.37 MPa	12.7 – 26.4 MPa
Adhesion strength	60 – 70 N/m ²	90 – 140 N/m ²	--

Table 2: Interlayer properties from literature and product data sheets (Sulkis, 2019; Pujol Group, 2020; Martin et al., 2020; Sinha et al., 2021; Kuraray, 2022)

2.2.2 Shear Transfer

Under mechanical load stresses developed in one sheet of a glass laminate are transferred through the interlayer into the other sheet. This load ‘sharing’ between the two glass sheets is called shear transfer, a higher degree of shear transfer leads to reduced maximum principal stresses in the glass sheets under load and increases the overall stiffness and fracture strength of the laminate (Callister & Rethwisch, 2018; Kuntsche et al., 2019).

The strength of laminated glass is highly dependent on the core (interlayer) properties, with both stiffer and thinner interlayers resulting in a higher shear transfer and lower max stress. The shear behaviour can vary, as depicted in Figure 9, between the layered limit where no shear transfer occurs ($W = 0$) and the laminate behaves as independently bending layers, to complete shear transfer ($W = 1$) at the monolithic limit in which the laminate behaves as a homogenous beam. Typical standard thickness glass interlayers have shear transfer coefficients (W) of around 0.5 – 0.7 at room temperature, but extra stiff interlayers such as Ionomer can achieve near complete

bonding ($W > 0.9$) which typically occurs for most designs when the shear stiffness is greater than 10 MPa (Kuntsche et al., 2019; Martin et al., 2020).

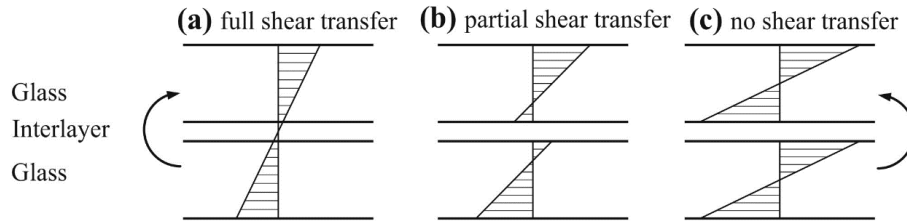


Figure 9: Laminated glass shear transfer behaviour (Kuntsche et al., 2019)

As the shear modulus for an interlayer is time-temperature dependent it follows that the laminates mechanical behaviour is also dependent, with increasing temperatures and load durations the shear stiffness of the polymer decreases, therefore decreasing the laminate stiffness and fracture strength. Novotny & Poot (2016) found that for all common glass interlayers the maximum impact resistance occurred near the glass transition temperature for each polymer, with performance rapidly dropping off at increasing temperatures and only the stiffest of interlayers providing suitable impact resistance at high temperatures of 60 °C. The impact of interlayer temperatures on principal stress in laminated glasses is explored more in Chapter 6.1.1 and in Appendix B with reference to New Zealand laminated glass design methodologies and the expected operating temperatures of glass-glass BIPV modules.

2.2.3 Manufacturing Processes

The industry standard for large scale manufacturing of laminated glass are the autoclave processes, nip-roller autoclave is the most common as it is well suited to high volume production. The nip-roll process referred to in Figure 10 is as follows: glass is pre-cut and washed thoroughly to remove all contaminants before being assembled in a lay-up stack within a temperature and humidity controlled chamber to prevent premature adhesion of the interlayer film. The layup then goes through a preheating furnace and a series of large, heated rollers which are responsible for degassing the laminate as well as sealing the edges to prevent air from entering back through the edges. The laminate is then autoclaved where it is heated to about 130°C and subjected to high pressure (10 - 12 bar) to permanently bond the glass and interlayer. The high pressure also diminishes any voids within the interlayer, a controlled cool down phase to about 50 °C with pressure maintained prevents these voids from re-expanding (G.James Glass & Aluminium, 2007; Carrot et al, 2015).

The vacuum-bag autoclave process is similar except that a vacuum bag is utilized for the de-airing process rather than a nip roller, the laminate is placed inside a vacuum bag and undergoes the lamination cycle inside an autoclave while a vacuum is maintained within the bag. This

process is much more labour intensive and limits throughput but lowers the risk of entrapped air, it is often used for multi-layer or curved laminates which cannot be nip-rolled.

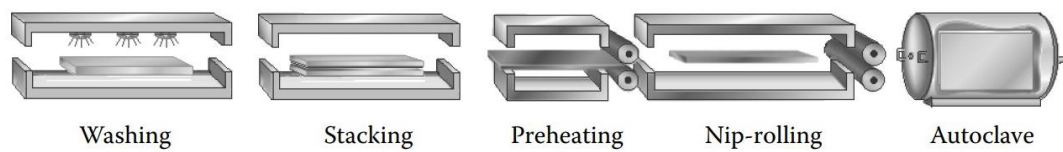


Figure 10: Nip-roll & autoclave process for laminated glass (Carrot et al., 2015)

Vacuum bag lamination can also take place in an autoclave-free process, instead using a non-pressurized oven for heating the laminate, this is often referred to as vacuum-bag only (VBO) process to indicate the absence of any external pressure outside of what the vacuum bag applies. VBO processes benefit from reduced equipment cost and production space, making it a good alternative to vacuum-bag autoclave for small-scale production of custom laminate pieces.

VBO lamination consists of 3 main stages as shown below in Figure 11, firstly the temperature is slowly ramped-up and held slightly above the melt temperature, usually 70–90°C, this stage is for removing air and VOCs as well as melting the EVA, allowing it to flow around inserts and fill in any voids. After a sufficient holding time the temperature is then ramped up to about 130°C and held, this step is responsible for curing the interlayer, chemical bonds form between polymer chains in a thermally irreversible process called cross-linking which drastically alters the material properties. Finally the temperature is ramped-down to about 50 °C in a cool-down stage before it is removed from the lamination oven to continue cooling to room temperature, the vacuum is maintained at about 30 mbar or lower during all heating stages and can also be applied during this cooldown to reduce thermal dimensional changes. Laminates with thicker pieces of glass require longer holding times at both the melt and crosslinking stages, this is to allow for uniform heating of the laminate as the reactions are highly sensitive to small changes in temperature (Folienwerk Wolfen, 2014; Bornemann, 2019).

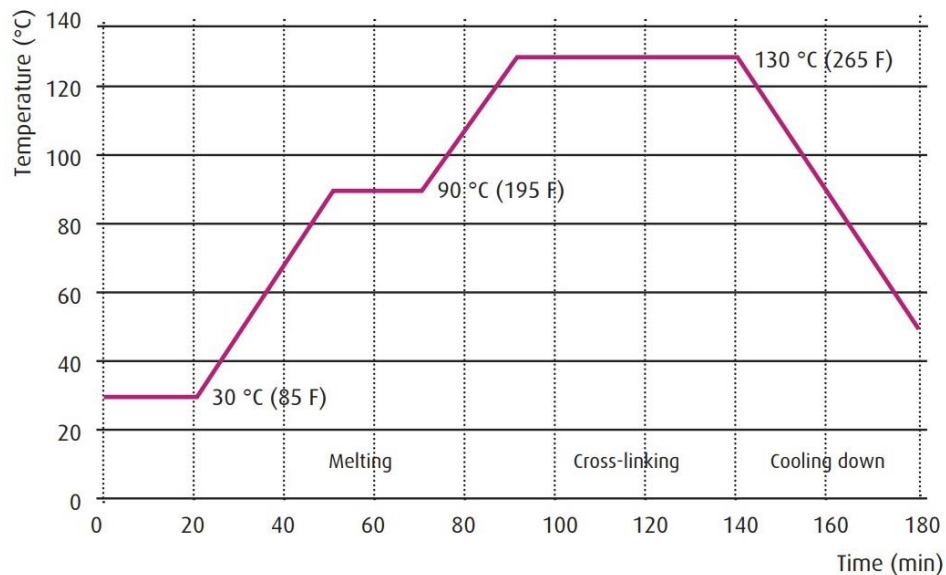


Figure 11: Oven temperature profile during VBO lamination (Folienwerk Wolfen, 2014).

Autoclave processes are typically used for non-crosslinking thermoplastic interlayers (PVB, Ionomer) because they release a relatively low amount of gas during the process, with most voids forming from water vapour already trapped in the interlayer. Because of this they can be effectively de-aired using nip roller and benefit from the production scale and simplicity of these methods, although it is possible to laminate such interlayers using vacuum bag processes (Bornemann, 2019). On the other hand chemically crosslinking interlayers (EVA) release considerable amounts of gaseous volatile organic compounds (VOC) during the lamination process, largely in part from the additives included to activate and facilitate the cross-linking process (Cattaneo et al., 2015), a vacuum needs to be applied to continuously to remove entrapped air and any VOCs to prevent bubbles forming in the laminate throughout the process, meaning that EVA is almost always laminated using an vacuum bag process.

2.3 Glass-glass Photovoltaic Lamination

PV lamination is the manufacturing process of permanently bonding the PV cells between a substrate and superstrate using a polymeric encapsulant, for glass-glass PV laminates the process is similar to the VBO process for laminated glass except that a specialized double-chamber laminator is used.

2.3.1 Encapsulants

Like in laminated glass a polymeric interlayer is used to bond the layers together and improve the structural properties of the laminate, although it is referred to as an encapsulant in the PV industry. In a PV module the encapsulant properties are vital for ensuring long-term power

generation, the encapsulant provides several functionalities including mechanical protection of the cells, prevention of moisture and oxygen ingress, electrical insulation, high adhesion to all module components, prevention of cell corrosion, and resistance to hydrolysis, UV, and thermo-oxidative ageing.

EVA encapsulants are predominantly used in conventional PV modules because they provide high optical transmission, low moisture permeation, and high electrical resistivity, however they are known to breakdown in the combined presence of UV, moisture and heat, releasing acetic acid that both causes and accelerates corrosion, delamination, and encapsulant yellowing. This is theorized by Sinha et al. (2021) to be a more significant issue in glass-glass module as the non-porous nature of the glass backsheet traps the acetic acid inside the module and worsens the damaging effects. Despite this EVA is still an excellent choice for encapsulation due to its numerous benefits and it currently makes up over 90% of the PV encapsulant market.

It is still of interest for PV manufacturers to explore alternative encapsulants with no breakdown products for glass-glass modules, especially because the non-porous back glass allows the use of higher diffusivity encapsulants that would not be viable in a conventional tedlar backsheet modules. One such alternative is PVB, which is often used in combination with an edge-seal to help overcome its high water absorption, PVB however does not provide the same level of electrical resistivity, increasing the risk of electrical potential induced degradation (PID) which occurs due to leakage current through the bulk and surface interfaces of the encapsulant (Pingel et al., 2010). Another alternative material and strong contender for future replacement of EVA are polyolefin elastomers (POE), alike PVB they have no breakdown products but also provide higher volume resistivity, lower water vapour diffusion and hydrolysis than EVA, and lower processing times in the case of thermoplastic polyolefins (TPO). POEs have low market penetration due higher prices but are effectively being used in glass-glass modules with exceptional lifetimes due to the elimination of PID, corrosion, and encapsulant yellowing (Cattaneo et al., 2015; Martin et al., 2020; Satpathy & Pamuru, 2020).

In addition to the encapsulant an edge seal is often also used in glass-glass modules to reduce the ingress of moisture from the module edges. The edge seal is a low diffusivity polymer in the border region of the module, applied in a transverse width of around 10 – 15 mm in either adhesive tape or pumpable sealant form, a cross-section schematic is shown in Figure 12. As the edge seal is aligned with the encapsulant layer it is also partially responsible for bonding the glass plies together, it must have high adhesion strength to prevent moisture ingress at the seal-glass interface and force water to enter through the bulk of the seal, the seal must also have sufficient mechanical properties to retain the structural integrity of the module under varying conditions.

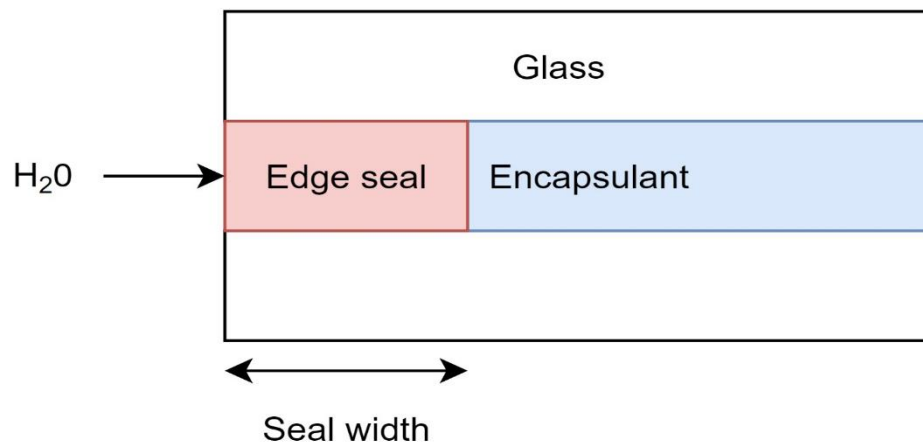


Figure 12: Cross section of glass-glass module with edge seal

The most commonly used edge seal material is polyisobutylene (PIB) due to its exceptionally low diffusion rate, around 10 times lower than a standard PVB encapsulant, PIB also has high elasticity and temperature resistance making it ideal for maintaining structural integrity under thermal and mechanical loads. Many other materials exist with even lower diffusivities but only a few have the desired mechanical properties to provide the necessary adhesion for the lifetime of a module (Kempe et al., 2010).

2.3.2 Lamination Process

PV lamination is typically done using a double-chamber vacuum laminator (See Figure 13), which consists of 2 chambers separated by a flexible membrane. The module layup enters the bottom chamber and is heated to the encapsulants softening point while the application of a vacuum to both chambers evacuates air and VOCs from the layup without applying any membrane pressure, during this pre-heating phase the laminate is raised slightly off the heating plate by pins to heat the laminate uniformly and prevent glass warping, the pre-heating stage is held for sufficient time to allow the encapsulant to flow into voids around the PV cells and circuitry, and for proper evacuation of VOCs. The pins then lower the module directly onto the heating plate to facilitate faster heating and temperature is raised to the crosslinking point of the encapsulant to begin curing it, the upper chamber is vented to atmospheric pressure while the lower chamber maintains vacuum, causing the flexible membrane to press down onto the module and apply a pressure of 1 bar, maintaining the modules shape and improving contact with the heating plate. A cooling stage finalizes the process, this can be done slowly with convection, or more preferably with a cooling press, which uses water circulated cooling while pressure is maintained on the module to rapidly decrease the temperature. The cooling press helps reduce the residual stress in the solar cells by both maintaining the shape of the module and by quickly terminating the EVA curing process to achieve an optimal encapsulant cross-linking degree (Lange et al., 2011; Satpathy & Pamuru, 2020).

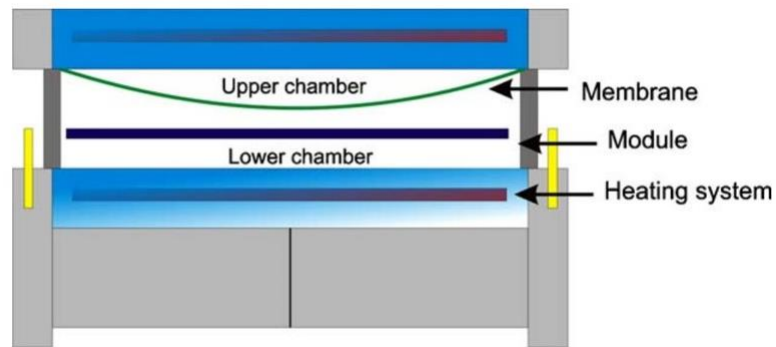


Figure 13: Double-chamber laminator (Drabczyk & Panek, 2012)

The stages of double-chamber lamination are similar to that of VBO lamination for safety glass, except that pressure applied is not constant throughout the process and the hold times at each temperature are typically much shorter due to the use of fast cure encapsulants, more efficient gas removal, and faster heat transfer. The double-chamber design allows for greater control over the lamination process than a typical vacuum bag process, specifically the ability to create a vacuum without applying external pressure to the module, which improves the efficiency of removing VOCs and helps prevent bubbles forming in the laminate (Cattaneo et al., 2015).

Correct application and timing of each lamination stage has a large effect on the final laminate quality. For EVA encapsulants the initial application of the vacuum must be applied early enough in the cycle to successfully remove all entrapped air and gas, but not so early that it also removes sublimed additives that are critical for activating and stabilizing the cross-linking reaction. The venting of the upper chamber to apply pressure on the layup must also occur at the correct time, if it is applied to early in the heating stage it restricts air removal and increases the risk of cell breakage, while if it is applied to late the hot and low viscosity encapsulant will permit cell displacement inside the laminate, creating a defect called string shift (Lange et al., 2011).

The window for cross-linking temperatures is narrow as the EVA needs to be cured within a reasonable time frame and achieve a suitable gel content (cross-linking degree) of about 70 – 95% (Drabczyk & Panek, 2012; de Oliveira et al., 2018), the reaction rate is highly temperature sensitive meaning a small decrease in temperature will reduce the gel-content and lower the adhesion, stiffness and optical clarity of the cured EVA (Chen et al., 2015). The maximum temperatures reached during the cross-linking also determines the residual stress in the PV cells and interconnects due to the thermal contraction that occurs during cooling, this is significant because the coefficient of thermal expansion (CTE) of the materials surrounding the silicon PV cells is much higher than the silicon itself, meaning that the glass, encapsulant, and interconnect ribbons will contract more and ‘squeeze’ onto the cell, with higher temperatures resulting in higher dimensional changes and more risk of cell damage (Dietrich et al., 2010, Shin et al., 2018).

3 Crystalline Silicon Photovoltaics

This chapter provides an overview of cell technology, module construction, and manufacturing of crystalline silicon (c-Si) PV technologies and methods for adding transparency to glass-glass modules.

3.1 Cell Technology

First generation silicon PV cells are made from thin wafers of crystalline silicon with metallic contacts screen printed on the surface layers, these cells are typically between 150–250 μm thick and come in standard sizes varying between 120 to 210 mm square.

There are 2 forms of crystalline silicon used in first generation silicon PV cells (Figure 14), polycrystalline silicon is made from multiple crystals and has limited efficiency due to the grain boundaries formed between the crystalline regions, monocrystalline cells are produced from a single continuous crystal of silicon and as such have no grain boundaries limitations, allowing for higher power conversion efficiency (PCE) compared to their multi-crystalline counterparts. Prior to 2018 polycrystalline silicon was the dominant PV technology due to lower production costs, however recent developments in monocrystalline technologies have led to it rapidly taking over the market, now making up 88% of global PV shipments in 2020 (Feldman et al., 2021).

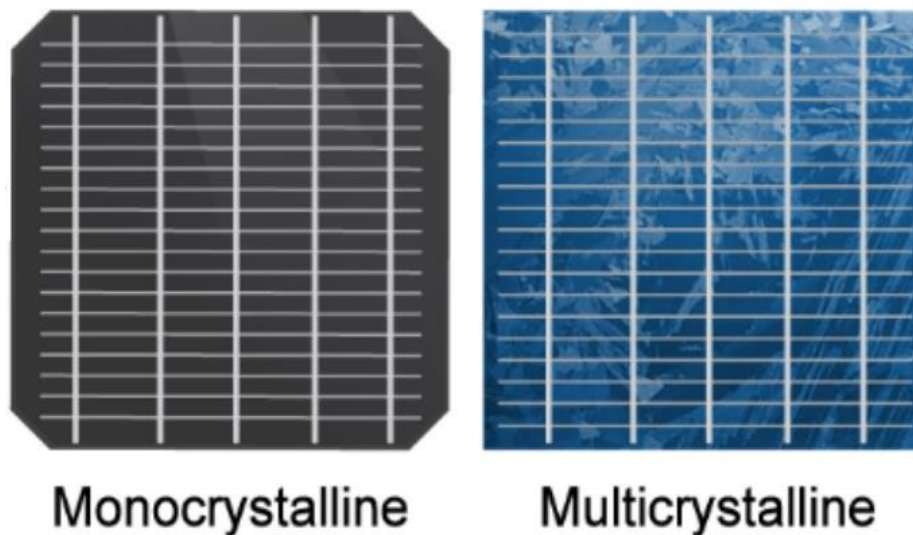


Figure 14: Appearance of mono- and poly-crystalline silicon PV cell (Smith et al., 2021).

Another significant differentiator between c-Si PV cells on the market is the cell architecture, innovative new cell structures can achieve performance improvements and cost reductions at both the cell and module level. The most common cell architecture today is the mono PERC cell

(passivated emitter and rear contact) which accounted for 85% of c-Si PV production in 2020 (Feldman et al., 2021). The mono PERC cell was a significant advancement for the PV industry as it allowed manufacturers to greatly improve production PCEs while only requiring small cost increases over the AL-BSF cells that it superseded, however with current PCEs pushing as high as 23% the PERC architecture is slowly nearing its estimated production efficiency limit of 24.5%, as such performance improvements are becoming slower and more difficult (Wilson et al., 2020).

Still the performance of c-Si cells is steadily being pushed higher by new cell architectures, a notable development discussed by Wilson et al. (2020) is SunPower's record breaking n-type interdigitated back contact (IBC) cell which achieved a PCE of 26.7%, close to the expected theoretical limit of 29.5% for a single junction c-Si cell. These higher efficiency cell types still have limited market share as the added manufacturing complexity increases costs, for example Woodhouse et al. (2019) estimated that IBC cells can be approximately 30% more costly than mono PERC cells with only a 7% relative increase in efficiency, limiting use to applications where maximum energy yield is prioritized over cost.

3.2 Cell Interconnection

Crystalline silicon PV cells are converted into PV modules by connecting multiple cells with thin metallic contact ribbons, and then laminating these interconnected cells between glass or polymer sheets with intermediate polymeric layers acting as a protective encapsulant.

Front and back metallization features are screen printed onto the cell surfaces by manufacturers using a silver paste. On the front-side rectangular contact pads called busbars form one set of cell terminals, with thin metallization features called fingers running perpendicular to them to collect and carry photogenerated current to the busbars. On the rear-side of the cell there are no fingers required as entire surface is conductive, the rear busbars often use a discrete sectioned design to reduce silver usage as depicted below in Figure 15. PV cells have at minimum 2 busbars on each surface with most modern high performance cells using a 5 busbar (5BB) design and some manufacturers producing up to 12BB cells, by using more busbars the fingers can be shorter, and the current carried in both the fingers and busbars reduced, lowering the resistive power losses in the metallization (Satpathy & Pamuru, 2020).

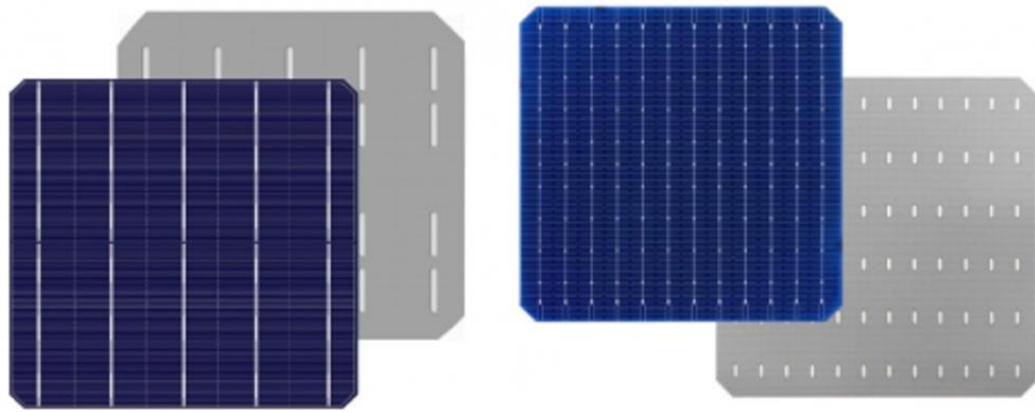


Figure 15: 5BB and 12BB solar cells with discrete rear contacts (ENF Solar, n.d.)

The busbars allow for cells to be connected to one other via a conductive contact, which is conventionally a thin and flat solder-coated copper ribbon that can be bonded to the cell busbars without the need for external application of a soldering medium. PV cell strings are interconnected using this tabbing ribbon in a process called tabbing and stringing, whereby the ribbons are soldered from the contact on the back of a cell to the opposite polarity contact on the front of the next cell to create a series connection called a “string” as shown below in Figure 16 (left). Rear contact cells such as the aforementioned IBC cell are connected into strings in a similar fashion however the tabbing ribbons all connect to the rear side of the cell with the negative and positive contacts located at different positions on the rear surface.

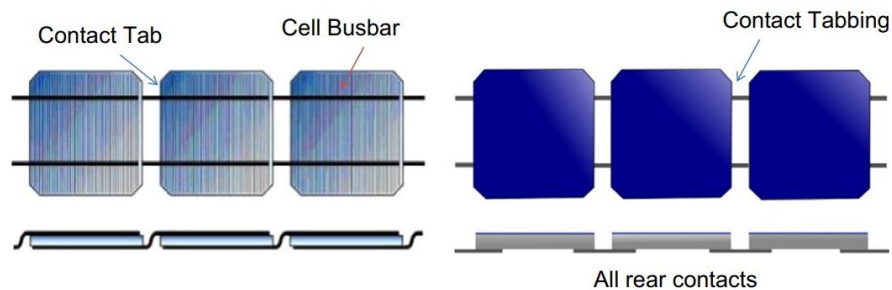


Figure 16: Conventional (left) and back contact (right) cell stringing (Mat Desa et al., 2016)

Cells are typically interconnected into sub-strings 10 to 12 cells long, 6 of these sub-strings will then be connected to create the overall internal circuit at a suitable voltage level, they are usually connected to each other by making an alternating “U-turn” circuit path as shown in Figure 18. The connection between each sub-string uses a wider and slightly thicker interconnect called a bus-ribbon, the larger cross-section of this ribbon is to allow for the higher currents that it transports, as it carries the entire cell current between sub-strings, whereas the

current within the sub-strings is divided among the multiple tabbing ribbons. A typical 2BB bus ribbon connection is demonstrated below in Figure 17.

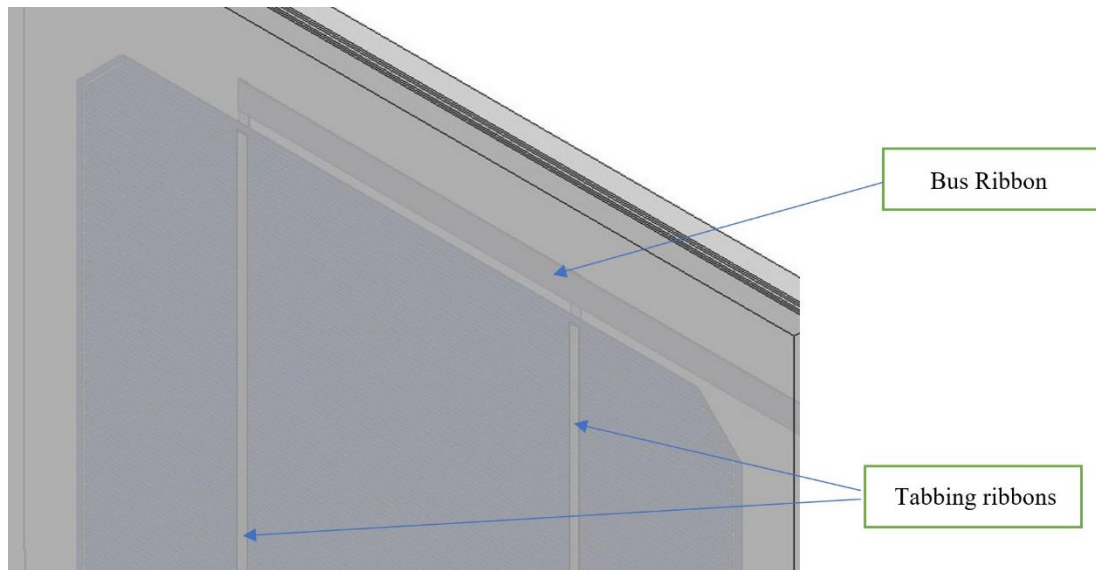


Figure 17: CAD model section depicting bus ribbon connection to the end of a cell sub-string

Connecting multiple PV cells in series will incur electrical mismatch power losses, this happens because cells that receive low irradiance (shading) produce a lower current than the rest of the string, and as all the cells are connected in series they all must reduce in output to match this low current, shading can also lead to hotspot heating in which a single shaded cell becomes responsible for dissipating all the power of the correctly functioning cells in the string, leading to excessive heating which could permanently damage the PV module (Vieira et al., 2020). Bypass diodes are used to partially alleviate some of the issues arising from cell shading, cell strings are connected in anti-parallel to a bypass diode so that if one cell within the string becomes shaded the bypass diode will activate and divert the current around the string containing the shaded cells, this also prevents the cell from exceeding its breakdown voltage and becoming permanently damaged. Figure 18 depicts a common series connection topology with 3 bypass diodes, the current path when a diode is activated is also shown.

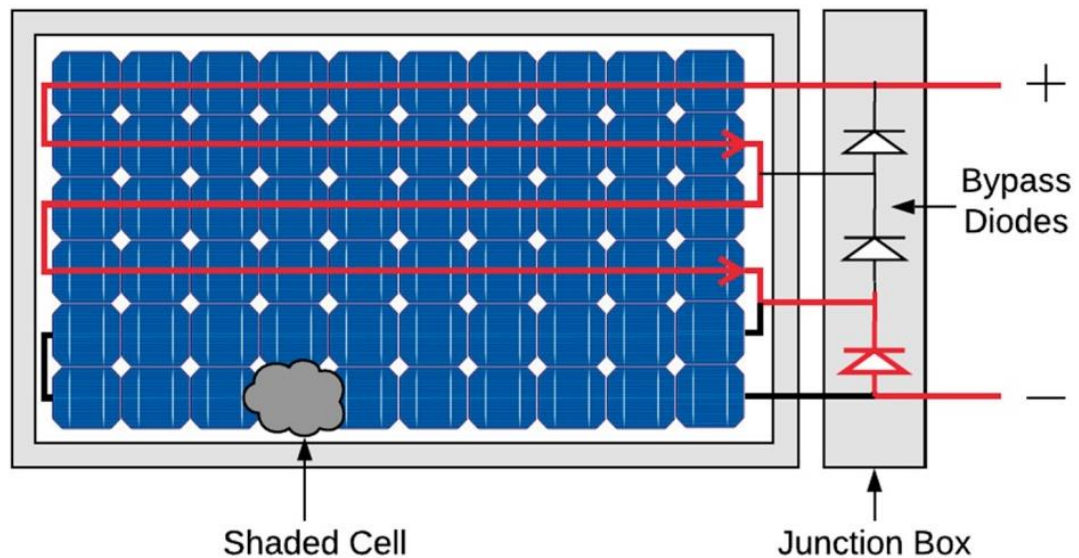


Figure 18: Common 3-string diode topology for 60 cell modules with bypass diode activated (Vieira et al., 2020).

The bypass diodes are housed in a junction box which is a small polymer casing attached to the outside of the PV module, this also provides external terminals for connecting PV modules to one another to form a PV system, a standard junction box will contain 3 bypass diodes with each being connected to 1 third of the module's cells, the junction box is connected to the internal module circuitry by means of bus ribbons that are either brought through a hole in the backsheet or between the 2 layers at the module edge. A pottant is used to fill the junction box to prevent moisture ingress into the module and aid in heat dissipation from the diodes.

Module interconnection can vary depending on number and type of cells, junction box and number of diodes, and the design of cell contacts and interconnects. A common alternate module design is the half-cell module, which can further reduce shading effects and resistive losses by cutting cells in-half and doubling the number of strings (Satpathy & Pamuru, 2020; Wilson et al., 2020). The use of alternative contact methods to reduce interconnect shading is another common avenue for performance increases, the use of shingled cells, which are connected in an overlapping design like roof tiles, or rear contact cells, which only have interconnects on the rear side, can reduce the inactive area shaded by front interconnects and increase overall module PCEs. Rear contact cells also open up greater flexibility for the use of innovative contact and interconnect designs, as discussed by Borgers et al. (2017) there is particular interest in alternative interconnect methods that integrate multiple wires or ribbons into an encapsulant or woven fabric (as depicted in Figure 19), in order to reduce resistive losses, interconnect stresses and material costs.

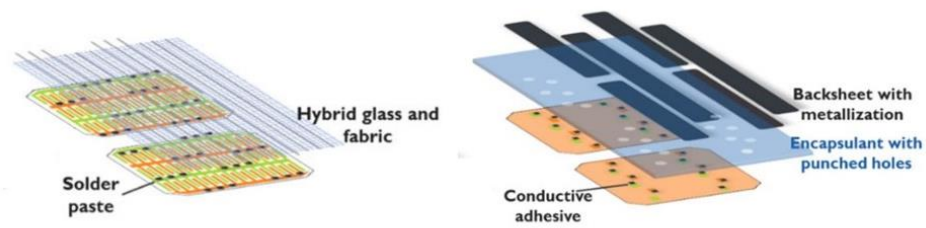


Figure 19: Example of alternative interconnect methods for rear contact cells
(Borgers et al., 2017)

3.3 Manufacturing Process

Crystalline silicon PV module manufacturing is typically a highly automated process, modern production lines use a combination of conveyor systems and vacuum gripping systems to automatically move cells and glass between most of the workstations along the production line. The manufacturing process can be divided into 4 main stages: tabbing and stringing, glass-handling & lay-up, lamination, and post-lamination. The tabbing-stringing and glass-handling/layup occur partly in parallel at the initial stages as the glass-handling step prepares the encapsulant and glass sheets for lamination while the tabbing-stringing involves the preparation of the PV cells and interconnects, the 2 processes merge when all the materials are placed in layers at the lay-up stage prior to lamination (See Figure 20).

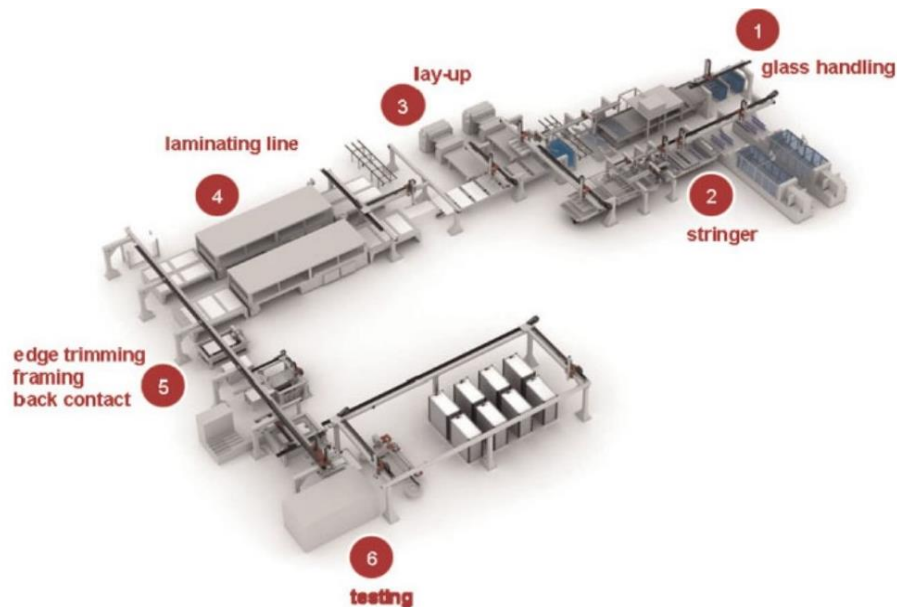


Figure 20: Schematic of a c-Si module turnkey line (Lange et al., 2011)

Tabbing and stringing is the process of interconnecting the PV cells to create a complete internal circuit as described in the previous section of this chapter, outside of very small

production environments almost all interconnection is done using an automatic soldering machine called a tabber & stringer. This equipment allows for high throughput, great control over interconnect quality, and significantly reduced cell breakage rates ($<0.1\%$) compared to manual soldering, additional features further improve interconnect quality, such as AI vision systems to detect defective cells and tab ribbon straighteners to remove camber and bends in ribbons. Typically, contactless soldering processes such as infrared soldering are used to prevent mechanical stress on the cells during the process (Satpathy & Pamuru, 2020).

The glass-handling and layup stage is the process of preparing and configuring the various layers of the module ready for entry into the laminator, the main steps are as follows:

- Glass washed with demineralized water and loaded onto conveyor
- EVA cut to size and laid onto front glass
- Cell strings laid up onto front glass/EVA
- Cell strings connected via bus ribbons (Can be Manual or automated)
- Electroluminescence testing to detect cell defects
- Edge seal applied (glass-glass only) and lay-up of EVA/back-sheet
- Bus ribbons brought through back sheet or out module edges.

The module lamination then takes place as described previously in chapter 2.3.2. Fast cure EVA encapsulants are often used, which allows for the entire lamination process to take place in around 10 – 15 minutes, however this can be even shorter if thermoplastic encapsulants such as PVB or POE are used.

The post lamination process is the most labour-intensive process and involves the attachment of all external componentry as well as stickering, inspection and testing. Many of these processes such as edge trimming, junction box attachment and framing are beginning to see more automation or machine assistance in order to further reduce cycle times.

- Edge trimming to remove excess EVA
- Junction box is wired to interconnectors and adhered to the backsheet
- Junction box filled with pottant and cured
- Aluminium frame fixed to the laminate with a framing machine and RTV silicone
- Module cleaned and visually inspected for defects
- Module electrical parameters tested using solar simulator
- Nameplate stickering
- Modules sorted and packaged

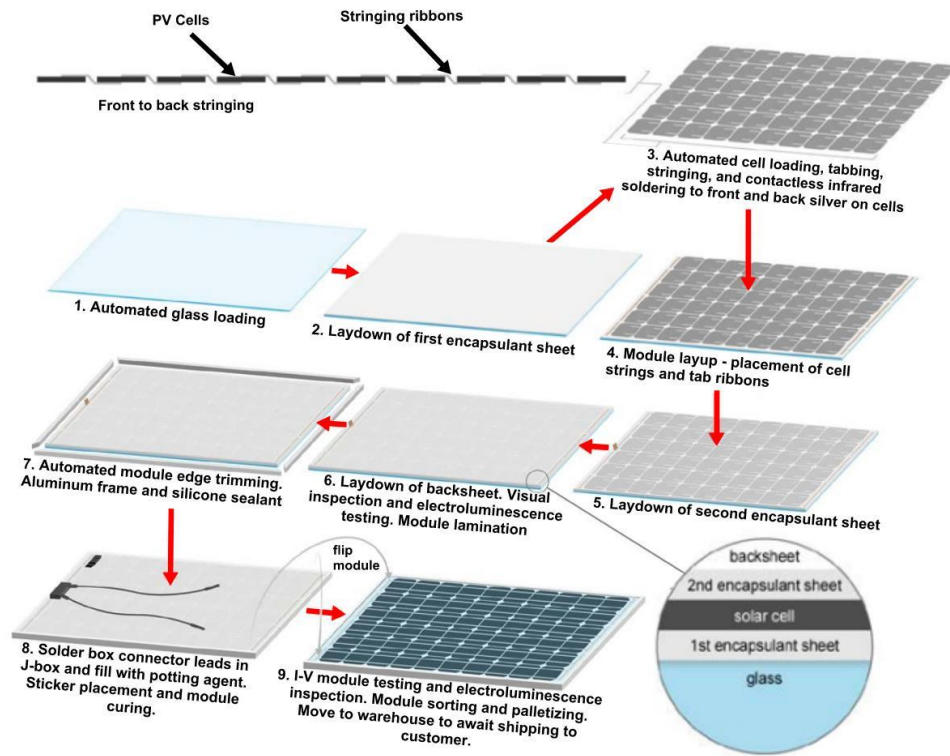


Figure 21: Glass-foil module manufacturing process (Woodhouse et al. 2019)

The production process described above (Figure 21) does not differ significantly for glass-glass modules with only minor changes occurring due to design differences. Glass-glass modules can use an edge seal which is applied during the layup step, especially when manufactured with a higher diffusivity encapsulant such as PVB, edge-seals are seldom used in glass-foil modules as moisture can bypass the seal by permeating through the polymer backsheet. A different junction box design which is installed on the side or edge of the module may also be favourable in glass-glass modules, more conventional back mounted junction boxes will require that a hole is pre-cut in the back glass prior to any heat-treatment of the glass, whereas edge junction boxes have the bus ribbons brought out the side of the lay-up without any cutting required. Finally due to the improved mechanical integrity of glass-glass modules there is a possibility for a frameless module configuration to decrease cost and weight in applications where the frame is not needed for structural or mounting reasons.

3.4 Semi-Transparent Crystalline Silicon Modules

Crystalline silicon is the dominant technology in BIPV with its 70% market share mainly driven by the roofing market (Grand View Research, 2021), the façade market is more balanced with about a 50 – 60 % share (Zanetti et al., 2017). There is currently only one commercially viable method of adding transparency which typically does not translate well to architectural design for

all facets of the building envelope, however continued commercial and research innovations are leading to new ways of improving the appeal and design flexibility of such modules.

3.4.1 Spatial Segmentation

The most common method to fabricate semi-transparent modules for BIPV is to arrange c-Si PV cells with large spaces between them in a glass-glass module construction, this allows for light to be transmitted through the extended cell gaps. The manufacturing is fairly simple as the process is similar to that of a conventional c-Si modules, except that the cells are strung together with longer interconnects and a larger gap. The main drawback of this technology is the aesthetic appeal, the large opaque PV cells create non-uniform lighting and appearance as shown in Figure 22, and despite the ability to reach high visible light transmission (VLT), does not provide a clear view through the product. This generally makes it a poor choice for vision regions in vertical glazing, although it can still be integrated well into a number of products such as skylights, canopies, external accessories, and opaque or non-vision cladding elements such as spandrels.



Figure 22: Spatially segmented c-Si BIPV modules integrated into overhead glazing (K. Lee et al., 2020a; Polysolar., 2021a)

In some cases the appearance of the PV cells is used for artistic benefit, or to highlight the use of green infrastructure, however the interconnects spanning between each cell can detract from this orderly grid-like appearance, this is where the use of alternative interconnect methods could be of benefit in BIPV. Using back contact cells in conjunction with multiwire interconnection methods could allow for much thinner and less visually obtrusive interconnection between cells and help improve the aesthetic appeal.

Due to the simplicity of manufacturing spatially segmented c-Si modules there have been many efforts to overcome its weakness by improving the aesthetic appeal, the majority of approaches involve cell modification to reduce the size of each opaque area within the module, this has been done by cutting cells into thin strips as seen below in Figure 23, while other manufacturers have added a number of small perforations to the cell in order to pass a small amount of light through. Researchers have fabricated highly transparent cells by laser cutting holes through a

200 μm silicon wafer, resulting in a high efficiency cell with a homogenous and neutral coloured appearance (K. Lee et al., 2020b), while other approaches have been to fabricate spherical micro-cells embedded in a substrate (K. Lee et al., 2020a). Few of these technologies have appeared in large-scale commercial use yet, as alternative PV technologies can provide similar aesthetics at significantly lower costs.



Figure 23: Examples of semi-transparent modules using modified c-Si cells.

Left: Perforated mono-crystalline BIPV sample (Ertex Solartechnik, n.d.), Middle: Thin-strip c-Si module developed for power generating IGUs (NSG Group, 2021), Right: High transparency 200 μm c-Si wafer (K. Lee et al., 2020a).

Another common approach to improve the appearance is to add colour and/or patterns to the laminate in order to reduce the appearance of sharp separation between the opaque and transparent region, this does not increase visibility through the product but does help to hide the grid-like structure. This can be achieved in a multitude of ways including, encapsulant, cell or glass colouring, decorative laminate inserts, glass-etching, ceramic frit, and selective-reflector coatings. Some of these approaches can also be used to make coloured or patterned modules that appear opaque and can even mimic the appearance of other materials while still allowing sufficient light transmission, a widely used product by BIPV manufacturers is a glass coating developed by SwissINSO which uses a diffuse selective reflectance coating to give PV glass an opaque coloured appearance while still maintaining over 80% VLT (See Figure 24).



Figure 24: Examples of PV cells and modules with modified appearances

Left: Polycrystalline cells coloured via selective anti-reflective coating (Ghosh, 2020), Middle: Coloured BIPV façade utilising Kromatix™ glass (Zanetti et al., 2017), Right: Opaque BIPV panels with integrated meshes and filters to mimic the appearance of other building materials (Ballif et al., 2018).

3.4.2 Luminescent Solar Concentrator

Luminescent solar concentrator (LSC) PV separates the light absorbing and energy generation functions by mounting PV cells around the edge of a glass or transparent polymer waveguide and embedding photoluminescent molecules in the bulk of the waveguide. The embedded chromophores absorb light in the visible wavelength range and then re-emit it as non-visible infrared light through stokes shifting, this re-emitted light is guided to the edge mounted cells via total internal reflection, (refer Figure 25), where it is absorbed for energy generation (Meinardi et al., 2017; Z. Li et al., 2021). LSCs are not specifically restricted to c-Si as the PV cells mounted around the edge of the waveguide can be made of any material, however given the small area available it is currently beneficial to use c-Si over thin-film cells to maximize efficiency.

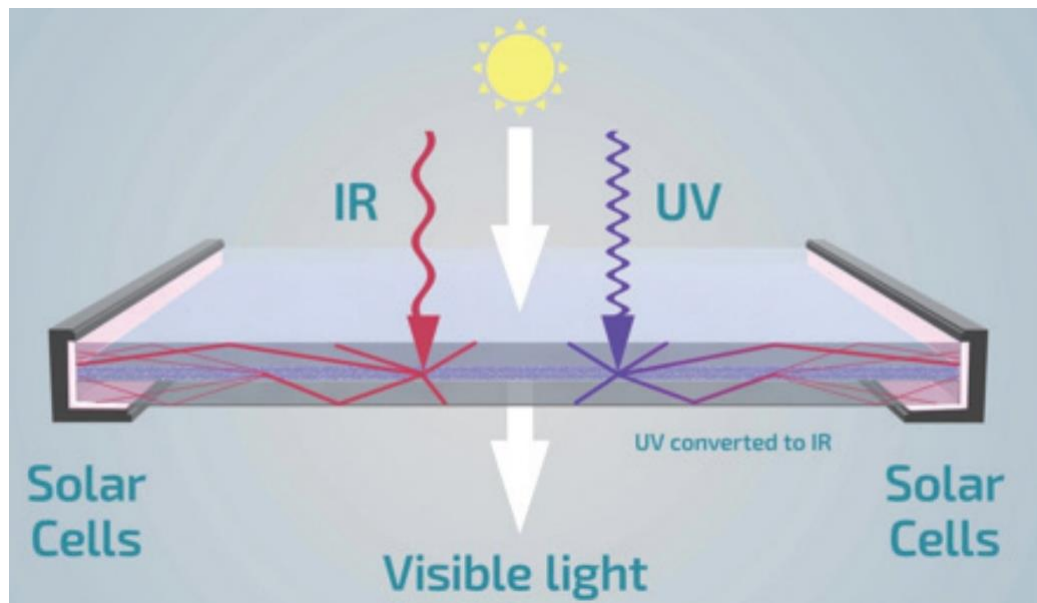


Figure 25: Dual UV/IR absorption LSC schematic

LSCs have 3 main absorption-emission cases where they can exhibit colour-neutral transmission, the first is when UV light is absorbed and NIR light is emitted, this design is limited as the UV energy available is small. The second case is NIR absorption and NIR emission at longer wavelengths, an overlap in these spectra will cause some portion of emitted light to be re-absorbed. The final case is when the chromophores absorb visible light, but evenly across the spectrum so that no colour tinting occurs (Z. Li et al., 2021).

There are number of downsides to this technology which limits it to mostly research interests (Zanetti et al., 2017), firstly the PCE is usually very low (about 2% or less) due to waveguide attenuation, reabsorption of emitted light, and low quantum efficiency of chromophores (K. Lee et al., 2020a), secondly the long-term stability is unproven as the resistance of the luminescent materials to moisture, light and heat over long time periods is not well documented, finally the attenuation of the re-emitted NIR light becomes significant for standard sized products and so soda-lime glasses are impractical as a bulk waveguide, more expensive optical materials with high IR transparency such as fluorinated PMMA or optical BK7 glass must be used to which are too expensive for general BIPV use (Meinardi et al., 2017).

If this technology were to become commercially viable in the future, it would offer superior aesthetics, as small area research LCSs have been proven to achieve visible transmittance and haze values similar to soda-lime glass (K. Lee et al., 2020a) and can be almost indistinguishable from a normal glazing. Such devices would likely fit in as a niche product where maximum visual transparency is highly prioritized over efficiency.

4 Thin-film Photovoltaics

Thin-film PV technologies utilise direct bandgap absorbers, allowing a significant portion of solar irradiance to be absorbed within only a few micrometres of absorber layer (T. Lee & Ebong, 2017), the current commercial absorber materials for thin-film PV are amorphous silicon (a-Si), cadmium telluride (CdTe), and copper indium gallium selenide (CIGS). The structures and manufacturing processes for opaque and transparent thin-film PV using these technologies are discussed in this chapter.

4.1 Film Structure and Manufacturing

The structure of a thin-film cell is a multi-layered film which generally contains a back contact, absorber layer, and front electrode with additional buffer/intrinsic layer(s) between the absorber and front electrode to optimize the film structure and align the bandgaps of each layer, a generic thin-film cross section is illustrated below in Figure 26. The front electrode must be transparent to the semiconductors absorption spectrum to permit light to reach the absorber layer and generate photocurrent, typically n-type transparent conductive oxides (TCO) such as doped tin, indium and zinc oxides are used for front electrodes as they are sufficiently conductive and have high transparencies (Stadler, 2012). For the back contact metals such as molybdenum, silver and aluminium are often used, it is not only desirable for the back contact to form a low resistance ohmic contact but also to be highly reflective to redirect unabsorbed radiation back into the absorber.

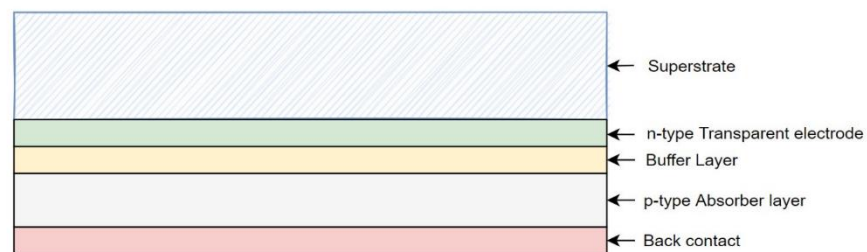


Figure 26: Cross-section of a generalised superstrate deposited thin-film PV

The resistivity of TCOs used as front electrodes is significantly higher than that of metal back contacts and as such has a significant impact on the electrical performance of large area films, in order to reduce electrical losses the film is partitioned into a pinstripe pattern of series connected cell segments about 6 – 10 mm in width (Brecl et al., 2005), this reduces the cell current and lowers resistive heating losses in the TCO layer, as well as increasing the module output voltage to a utilizable level. This partitioning is done by scribing grooved lines through each layer to connect the TCO and metal back contact and allow current to flow through the film from cell to cell (Figure 27), each of the 3 scribes is offset from the previous one to provide

suitable electrical isolation, the scribe and offset widths create a total dead zone width of about 0.25 – 0.5 mm per cell, resulting in a film having about 90% – 97% overall active area which can generate photocurrent (Başol & McCandless, 2014).

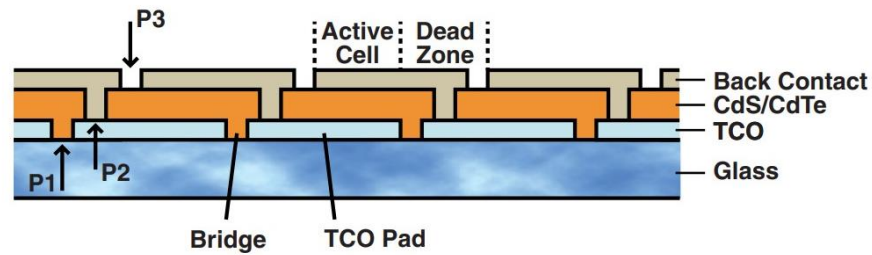


Figure 27: Superstrate deposited CdTe film structure showing the P1, P2, and P3 laser scribes. (Başol & McCandless, 2014)

The general procedure for superstrate deposition and scribing is as follows; firstly a TCO is deposited on the superstrate (usually 3.2 or 4 mm annealed glass) followed by a P1 laser scribing process which removes a thin strip of the electrode through photoablation. The absorber and buffer layer(s) are deposited and subsequently P2 laser scribed, in some processes an insulating plug is then deposited into the P2 scribe to provide more lateral resistance between cells and allow for a reduction in dead-width. The back contact is then deposited and the P3 scribe completes the monolithic interconnect region, further laser processing is done to create electrical contact pads and an edge delete region which electrically isolates the cells from the module edge and removes edge defects (Booth et al., 2010). Thin-film cells can also be substrate deposited in which the order of the deposited materials is reversed, with the metallic back contact deposited first on a substrate material and the TCO electrode deposited and scribed last, this is typically only used commercially for CIGS technologies as higher efficiencies are attainable for both CdTe and a-Si using superstrate procedures.

Deposition methods vary between cell layers as each film must be optimally produced to achieve ideal properties. Metal (back contact) and metal oxide (TCO) layers are often formed by DC or radio frequency sputtering deposition, in which a power supply is applied across the source material and substrate in a vacuum chamber and bombarded by a sputtering gas such as Argon (Stadler, 2012; Jilani et al., 2017). Deposition methods used for the absorber layers vary much more significantly between technologies and are often complex with additional processes required to treat and/or dope the absorber layers in order to remove defects and optimize the film-structure, an overview of the most common methods for each technology is given later in this chapter.

The scribing process utilizes short laser pulses on the scale of nanoseconds to selectively remove a circular area of material, these pulses are emitted at high frequency while the laser is

moved along a scribe line to create a continuous groove from the overlapping apertures of ablated material (Booth et al., 2010). The scribing process must be optimized for each material layer to achieve high module efficiencies as the quality of the scribe is sensitive to a vast number of factors such as laser energy and frequency, pulse length, frequency and spot diameter/overlap, Figure 28 below shows the large variance in scribe quality as a result of laser parameter changes (Rekow et al., 2010).

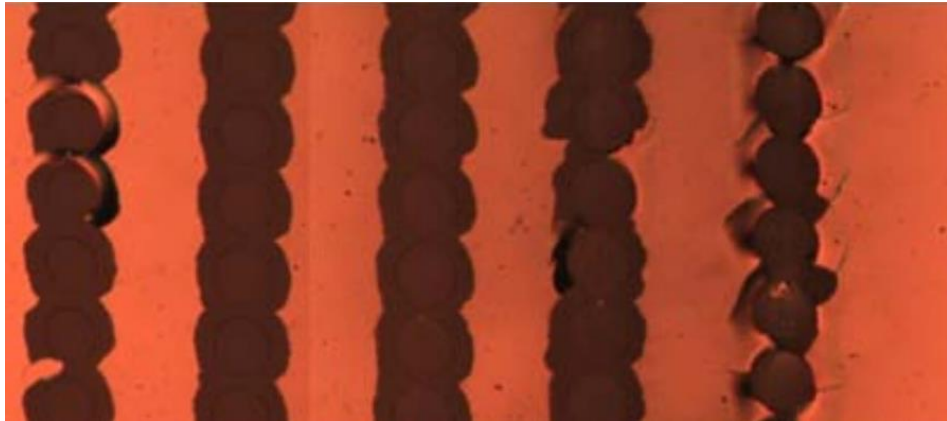


Figure 28: CIGS scribe lines with individual pulses visible (Rekow et al., 2010)

After the deposition & scribing stage the internal circuitry is already formed, as such no cell tabbing is required and the film only requires the attachment of bus ribbons prior to lamination, contact ribbons are attached to the electrodes exposed at opposite ends of the film using an electrically conductive adhesive or ultrasonic soldering. The lamination process is similar to c-Si modules with the main difference being the thickness and configuration of the encapsulant layer, one thin layer of encapsulant is used as there are only 2 plies in the laminate and the flexible PV film requires less protection from mechanical damage. An edge-seal is also likely to be used in thin-film modules, while not limited to only thin-film it is more commonly used due to the higher moisture sensitivity of the PV film.

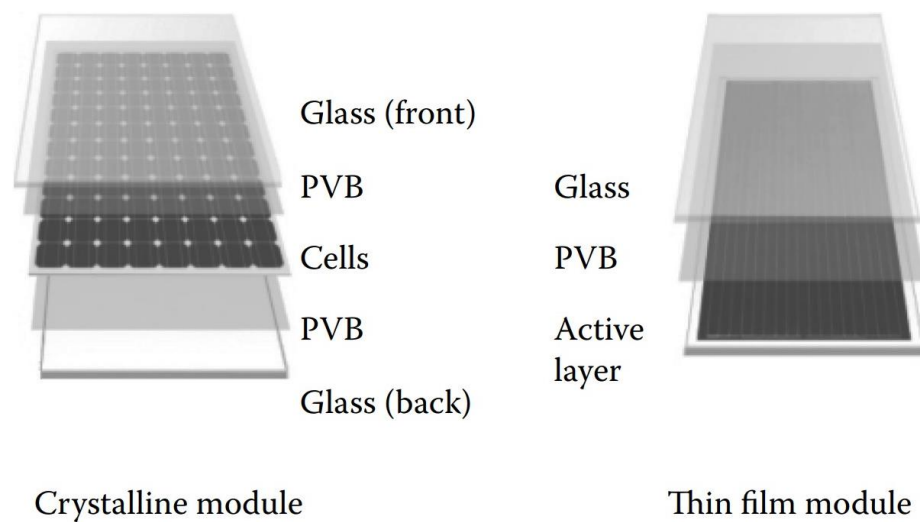


Figure 29: Crystalline and thin-film glass module construction (Carrot et al., 2015).

The monolithic interconnect does not easily allow for the addition of bypass diodes without incurring significant cost and complexity, however the monolithic film is typically more resistant to shading effects due to lower currents and the pinstripe layout of cells, which can be seen in Figure 29, within the module. Junction boxes for thin-film modules do not require multiple bypass diodes as there are no sub-strings to be bypassed within the module, instead they may contain a single diode for externally bypassing a shaded module. This means a smaller form factor can be used and the junction-box can be mounted more discretely at the edge or side of modules which is beneficial for frameless and see-through BIPV modules.

4.1.1 Amorphous Silicon

Amorphous silicon is a very mature thin-film technology that benefits from low cost, non-toxic manufacturing processes, it is no longer considered a large scale PV technology, making up just 0.2% of global PV production in 2020 (Phillips et al., 2022), owing to inherently low efficiencies which have stagnated in research cells at about 13% for the last decade or so (T. Lee & Ebong, 2017; Green et al., 2021).

Amorphous cells utilize a p-i-n structure, with a thick intrinsic a-Si layer capped on either side by thin p and n doped layers, the silicon must be hydrogen passivated to reduce the density of dangling bond defects. High efficiencies are obtained with multi-junction structures, which use multiple cell levels of differing bandgaps to more strongly absorb light over a wider spectrum, the top-most cell has the highest bandgap to absorb the short wavelengths of light while still passing the longer wavelengths to the lower cells. Multi-junction devices also reduce the effects of the Staebler-Wronski effect, which is a light-induced degradation of a-Si films that reduces power output on exposure to intense light, caused by the destruction of hydrogen-silicon bonds

partially reverting the hydrogenation process and increasing the density of dangling bonds (T. Lee & Ebong, 2017).

A common multi-junction device structure is the micromorph tandem cell, so called because it combines an upper amorphous cell with a lower micro-crystalline ($\mu\text{c-Si}$) cell, the general layer structure is depicted below in Figure 30. Typically doped zinc or tin oxides are used for the TCOs while a silver contact may also be used as a rear contact and reflector (T. Lee & Ebong, 2017; Sai et al., 2018). An intermediate reflector can also be used between the 2 cells to re-reflect short wavelength light back into the high-bandgap top cell for increased absorption.

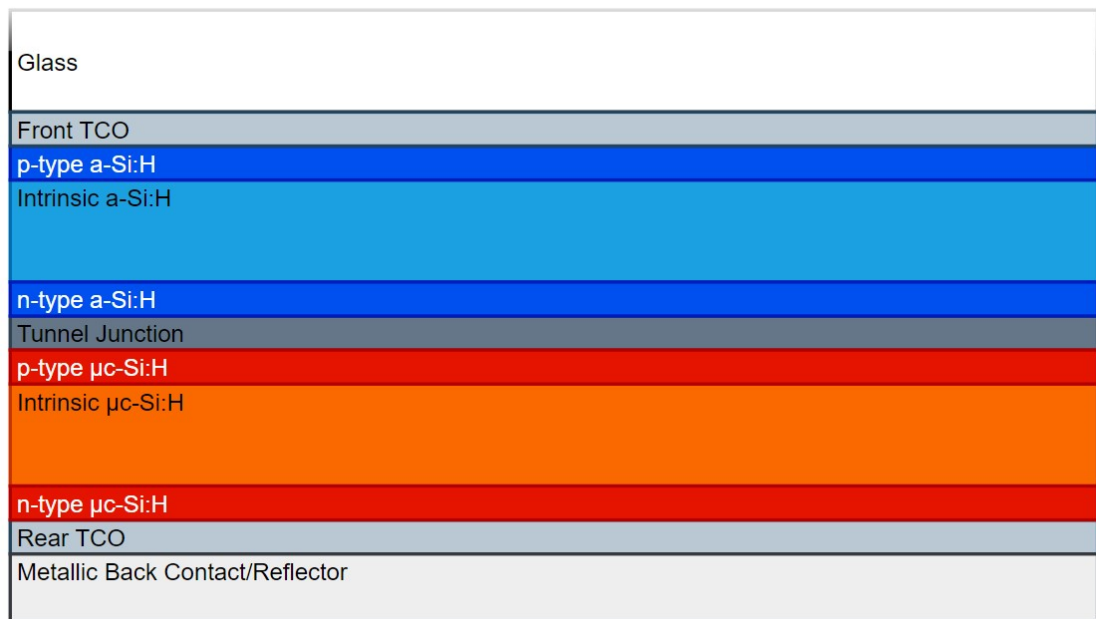


Figure 30: Superstrate deposited micromorph cell structure

Both $\mu\text{c-Si:H}$ and a-Si:H films are manufactured using very-high frequency plasma enhanced chemical vapour deposition (VHF-PECVD). Plasma reactor boxes are usually used which introduce silicon and hydrogen containing reacting gas (often SiH_4 and H_2) between electrodes and excited them to a very high-frequency (40 – 60 MHz) using an AC or RF signal to form a plasma, the plasma then reacts to form a layer of thin-film silicon on a substrate within the reactor box (Schmitt, 1989), additional reactive gases containing boron and phosphorous (such as B_2H_6 and PH_3) are used to create p- and n-type silicon layers respectively (Sai et al., 2018). PECVD allows for fast deposition at relatively low substrate temperatures due to the mobility of electrons within the plasma.

4.1.2 Cadmium Telluride

CdTe currently holds the largest market share of thin-film PV, at about 6% of all PV and 80% of the thin-film market (Phillips et al., 2022), due to the low manufacturing costs achieved through development of large area deposition techniques and equipment. CdTe modules can be produced at a similar cost to c-Si (Smith et al., 2021) and have recently commercial module efficiencies records of 19.0% were achieved (Green et al., 2021). A typical CdTe device structure is depicted below in Figure 31.

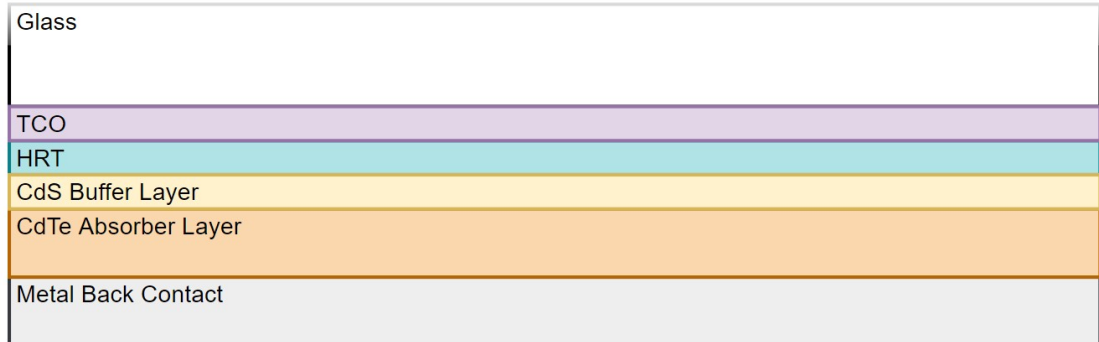


Figure 31: Standard superstrate deposited CdTe device structure (HRT = High Resistivity Transparent layer)

One of the most successful deposition methods for CdTe is the vapour transport deposition (VTD) process developed by NREL which can produce cycle times below 3 minutes. This system cannot be described in great detail as it is proprietary, however the following details are publicly available: first a powder chamber provides a continuous supply of solid source materials, this powder is then converted to a gas by rapid sublimation in a vaporizer, the vaporized Cd-Te is then carried by an inert gas in a distributor system where it coalesces on a heated glass substrate to form the initial CdTe film (Powell et al., 1998; Rose & Powell, 2002).

Deposited CdTe films are of poor grain quality and must be treated with chlorine to obtain high efficiencies, this is usually done by annealing at temperatures of about 350 – 440 °C after treatment with CdCl₂ via physical vapour deposition or methanol solution (Romeo & Artegiani, 2021).

Film quality of deposited CdTe films are temperature dependent and high substrate temperatures generally improve the attainable PCEs of the final device, processing temperatures for commercial devices are limited to below 515°C by the strain point of soda-lime glass. Additionally the processing temperatures require that high efficiency CdTe be superstrate deposited, because in substrate processes the metal contact is deposited first and would become damaged by the subsequent high temperature deposition of CdTe (Başol & McCandless, 2014).

4.1.3 Copper Indium Gallium Selenide

CIGS is a promising thin-film technology with cell efficiencies on par with CdTe and polysilicon, current efficiency records sit at 19.2% for mini-modules (Cd free) and over 22% for laboratory cells (Klinkert, 2015; Green et al., 2021). CIGS can be fabricated from multiple procedures and onto a number of substrates, there is plenty of potential for future improvement and many researchers believe that device efficiencies of 25% will be achievable, despite these benefits its commercial success has been limited by current difficulties surrounding cost-effective scaling up of both module size and production volume (Wilson et al., 2020).

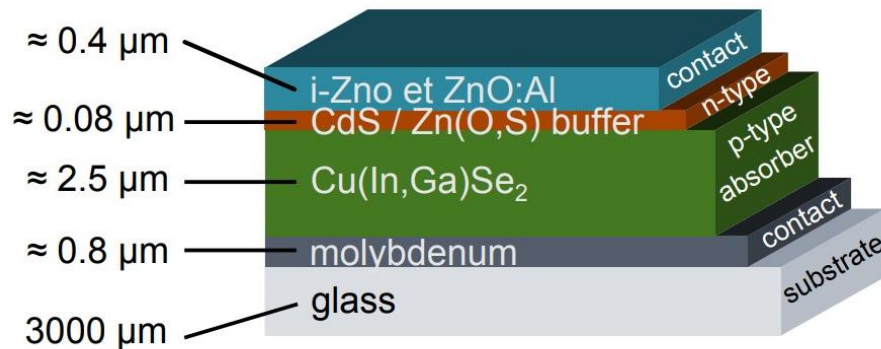


Figure 32: CIGS device structure (Klinkert, 2015)

High efficiency CIGS modules are substrate deposited, with molybdenum used for the back contacts as shown in Figure 32 (Klinkert, 2015), there are numerous methods for the preparation of CIGS cells with effective PCEs, however only 2 of these methods have seen much use in mass production.

First is the 2-step or selenization-after-sulfurization (SAS) process which is easily scalable and has produced laboratory efficiencies above 22%. The procedure uses sputtering to deposit a metallic Cu-In-Ga precursor followed by selenization, either by annealing at elevated temperatures in a H₂Se atmosphere or by evaporating a Se layer on top of the deposited precursors and rapidly heating to temperatures of about 550 °C. The latter selenization process while more costly is beneficial as it avoids the handling of toxic H₂Se gas.

Co-evaporation is the second mass-production process achieving efficiencies above 20%, it uses simultaneous thermal evaporation of copper, indium, gallium and selenide within a high vacuum chamber. This can be done in single-stage, bi-layer, or three-stage process variations to allow increasingly precise control over the ratio of metal constituents at different depths of the absorber layer for bandgap grading (Klinkert, 2015; Wilson et al., 2020).

Laser scribing of CIGS is difficult due to the high thermal conductivity of the absorber and contact materials, energy absorption from laser pulses induces local compositional changes which can form shunt paths (Rekow et al., 2010; Gečys et al., 2017). In the past a mechanical scribe process was used for the P2 and P3 grooves, although it suffered from poor scribe edge quality (Booth, 2010; Rekow et al., 2010). Research into laser process for P2 & P3 scribing of CIGS have demonstrated processes that can produce scribes without inducing shunt defects, with most relying on ultra-short pulsed lasers, however the equipment costs are significantly increased and may also limit processing speeds to below viable speeds (Rekow et al., 2010; Gečys et al., 2017). It appears that an industry-accepted laser process has not yet been widely adopted for CIGS manufacture.

4.2 Semi-Transparent Thin-Film Photovoltaics

The first neutral coloured see-through PV cell was developed using thin-film technology by Sanyo Corp in 1993 (Takeoka et al., 1993), since then commercial development has led to semi-transparent thin-film technologies becoming the superior option for balancing aesthetics and cost.

4.2.1 Aperture Type

As it stands this is one of the most successful approaches for creating semi-transparent photovoltaics (STPV), it benefits from the low cost manufacturing of thin-film PV with minimal alterations to the deposition process, and existing equipment can be adapted to the additional production stages. A uniform and neutral coloured light transmission spectra can be achieved, as shown in Figure 33, making it highly aesthetically appealing for BIPV products.



Figure 33: a-type thin-film BIPV of varying transparencies and colours (Corti et al. 2020)

Adding transparency is accomplished by creating small apertures through the opaque layers of the monolithic film to form regions where the full spectrum of light can pass through, (See Figure 34), the small size of the apertures allows for very uniform lighting as the distinction between opaque and transparent regions is not obvious when viewed from afar, the distance at which this non-uniformity becomes apparent will depend on aperture size, shape and positioning. These apertures are usually formed via laser scribing using the same equipment that forms the monolithic interconnect scribes, the process is often referred to as the P4 scribe. Alternative aperture formation methods have been investigated in research, such as the work by Sidali et al. (2018), who created a semi-transparent CIGS cell by electrodeposition on a treated substrate, essentially building up the film structure with apertures already in place.

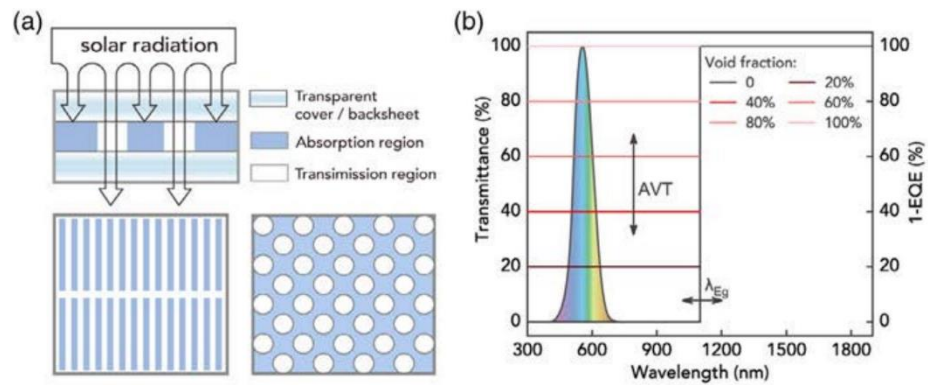


Figure 34: Examples of aperture-type film (a), and effect of removed absorber material on transmittance (b). (Z. Li et al., 2021)

P4 laser scribing can affect the composition and structure of the absorber layer at the boundary of the aperture, this creates shunt defects which increase conductance between the top and bottom electrodes leading to the formation of current leakage paths which negatively affects device output. Significant shunt defects primarily occur only when the film contains highly conductive and low melting point elements such as the copper in CIGS cells, but non-metallic absorber layers can also be affected by aperture formation, as was observed in a-Si cells with shunt defects arising from material flaking and crystallization at the aperture boundaries (Kuk et al., 2019). Ideally the P4 process is carried out with negligible change to shunt resistance, in which case the decrease in PCE would be identical to the fraction of absorber material removed (void fraction), thin-film technologies that can be P4 scribed with low shunt defects will have a linear decrease in power as VLT is increased, thereby making them more suitable for high transparency devices.

4.2.2 Ultra-Thin Film

Ultra-thin film (UTF) is another method for thin-film STPV that uses a transparent back contact to enable transmittance of un-absorbed light through the cell and a reduction of the absorber layer thicknesses to increase the transmitted fraction of light. UTF has the advantage over a-type cells that light is equally transmitted through all regions of the cell and so has a completely uniform appearance from all viewing distances, despite this UTF modules have not seen much commercial success in full-sized PV modules due to a number of inherent performance disadvantages, the manufacturing of such devices is also less favourable as the use of a TCO back contact and thinner device structure may require deviation from the standard low cost deposition techniques.

The efficiency of UTF cells is hindered by the use of transparent back electrodes, as the lower conductivity of TCOs introduce higher series resistances than the conventional opaque metallic electrodes. Further efficiency decreases arise from the ultra-thin layer structure due to a reduced fraction of absorbed light, increased recombination losses due to lower diffusion distances, and reduced shunt resistance due to larger surface roughness to thickness ratios (Kuk et al., 2019). These effects are all proportional to the thickness of cell meaning that creating high transparency UTF devices is limited by increasing losses and minimum achievable thickness.

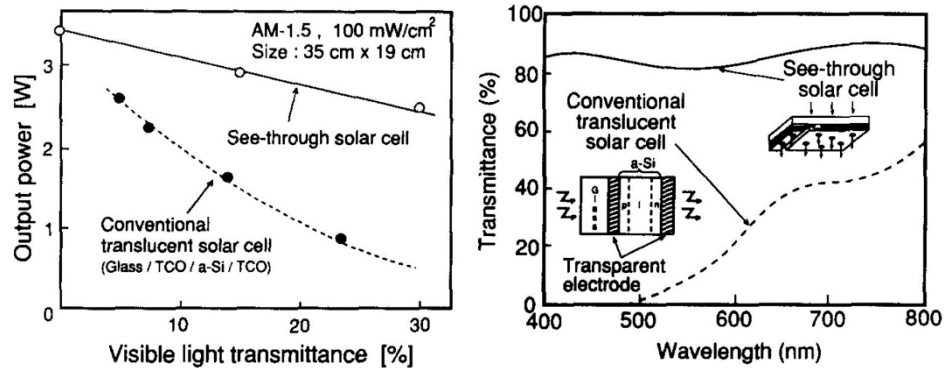


Figure 35: Optical comparison of a-type (See-through) and UTF (Translucent) a-Si solar cells (Takeoka et al., 1993)

With respect to BIPV there is another critical downside to UTF modules in that the absorber layer absorbs shorter wavelength light more strongly, giving the transmitted light a reddish-yellow tint as is indicated in Figure 35 (Takeoka et al., 1993; K. Lee et al., 2020a). The colour tinting is ill-suited for human comfort, and typically architectural glass favours green-blue tint as being more visually acceptable than warmer coloured tints (Yang et al., 2019). The tint of UTF cells can be overcome by using coloured back glass or interlayers behind the absorber layer to create a more neutral spectra or coloured STPV, as shown in Figure 36, although this comes with reduced transmittance and slightly increased cost while also providing inferior

efficiency compared to a-style modules which can be coloured just as effectively using the same methods.



Figure 36: UTF a-Si module with modified colour (Yeop Myong & Won Jeon., 2015).

Left: Optimized layer thickness for blue shifted natural tint, Middle: Green-blue back glass, Right: Hybrid a-type/UTF film with Blue PVB

4.2.3 Selective Absorptance

Selective absorptance PV cells absorb only a specific range of wavelengths, for the purpose of neutral-coloured STPV with high transparency this range of wavelengths needs to be primarily in the non-visible regions. This can be achieved by raising the bandgap past the visible light spectrum to absorb UV light only, however the portion of solar energy in the UV band is very small and would limit the theoretical maximum efficiency of such a device to just 6.4% (Z. Li et al., 2021). Alternatively only IR light could be absorbed; however this is not possible with conventional semiconductors as they continuously absorb light above the bandgap, meaning a material suitable for IR absorption will also absorb the higher energy visible light to some extent.

Current first and second generation PV semiconductors cannot selectively absorb IR light due to their bandgap behaviour, nor do they have bandgaps high enough for UV only absorption, however certain emerging third generation thin-film technologies are capable of true selective absorptance. Perovskite cells can be tuned to very high bandgaps for UV selectivity using halide substitution methods, and organic PV (OPV) can achieve IR selectivity due to the distinct absorption spectra of organic molecules (Z. Li et al., 2021). Furthermore these 2 technologies can be combined in a tandem structure to absorb both UV and IR light and create a device with both excellent transparency and high efficiency, research cells using this structure have achieved efficiencies of around 11% at an exceptional visible light transmittance (VLT) of 53%, which is on par with commercial c-Si STPV, as shown in Figure 37 (Zuo et al., 2019, as cited in Z. Li et al., 2021).

OPV may have high future potential for integration into BIPV, due to the capability for NIR selective absorption, very low fabrication cost, and wide variation in colours and transparency (Z. Li et al., 2021). To complement these characteristics some OPV have a zero or positive temperature power co-efficient (Y. Zhang et al., 2018), a performance benefit that is especially useful for BIPV due to the higher cell operating temperatures.

Despite these exceptional characteristics there are many obstacles for emerging PV, both OPV and perovskite have limited environmental stability due to intrinsic sensitivity to water and oxygen, with OPV beginning to see some use in BIPV projects but still struggling to reach 10 years of stable lifetime (Y. Zhang et al., 2018; K. Lee et al., 2020a). In order for these emerging technologies to become competitive they would likely need to at least match the guaranteed 20 – 30 years of stable power output provided by current technologies. Additional barriers are the scaling up of production and device sizes as well as the toxicity of perovskite cells due to the necessity of lead to create effective devices (Wilson et al., 2020).

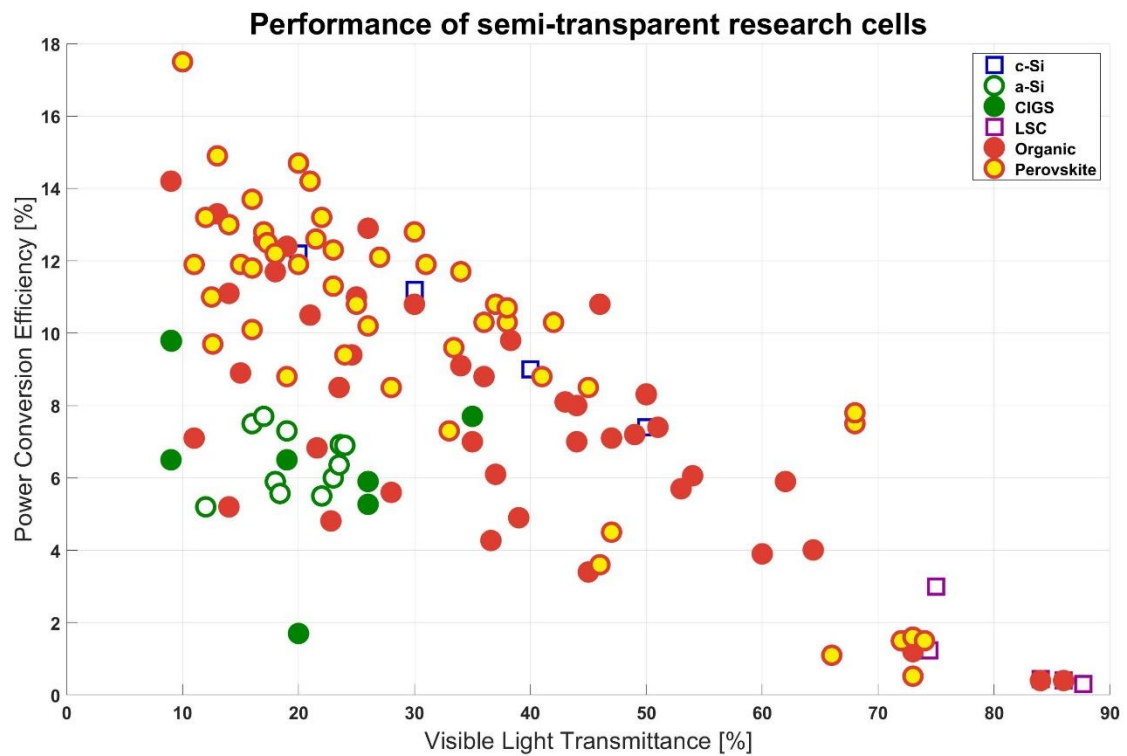


Figure 37: PCE vs VLT for transparent research cells, indicating the high potential of perovskite and organic cells over the full transparency range. Data from Almora et al. (2020), K. Lee et al. (2020a) & (2020b), Z. Li et al. (2021), and Sidali et al. (2018)

5 BIPV Performance & Feasibility

BIPV modules should not be presented as a conventional PV product for which only a few performance aspects matter, but rather as a multifaceted product with several functionalities (Ballif et al., 2018). This is because BIPV systems will usually have much lower yields when compared to conventional rack-mounted PV systems and so can often be written off as poorly performing and not worth the cost. Furthermore there are many variables that can alter the feasibility and competitiveness of BIPV, some of which are shown below in Figure 38, of these parameters the most significant for performance at the module level and manufacturing processes are discussed in this chapter.

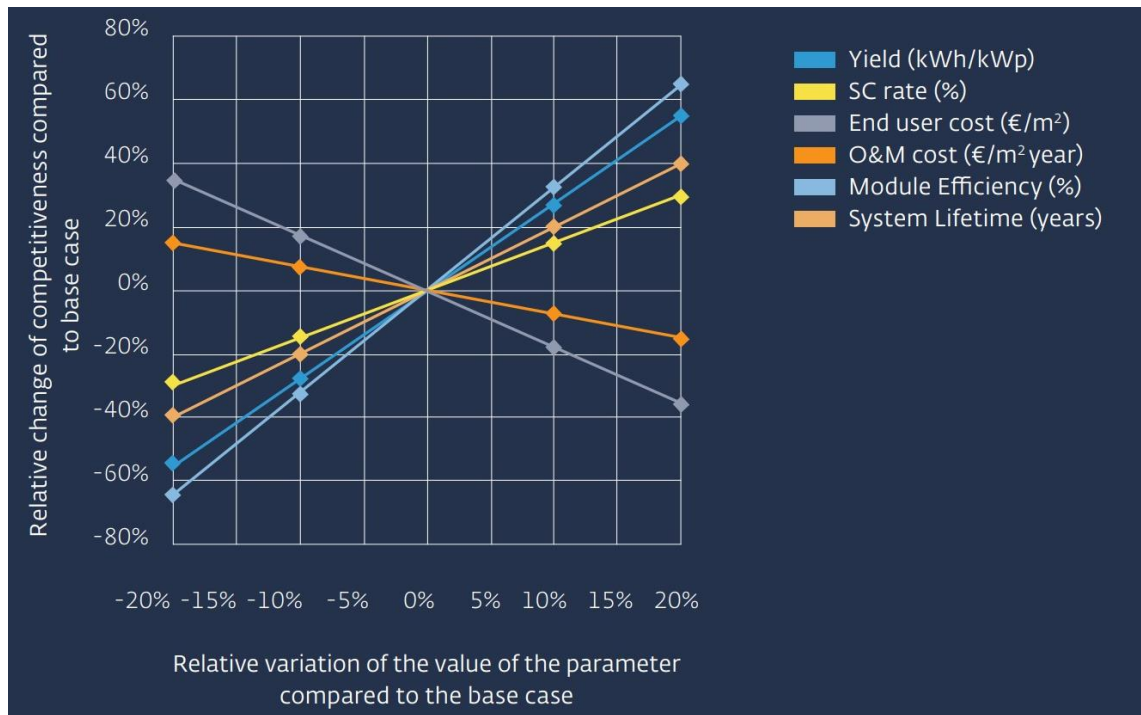


Figure 38: Electricity cost sensitivity of grid-connected BIPV systems (Corti et al., 2020)

5.1 Power Conversion Efficiency

The power conversion efficiency is the portion of solar energy that is converted to electrical energy, it is measured under standard test conditions (STC) to eliminate inconsistency due to variations in temperature and light energy, the fixed conditions for STC are 25 °C, 1000 W/m² irradiance and AM1.5 spectrum, which is the light spectrum that occurs when sunlight travels through 1.5 times the perpendicular thickness of the atmosphere. The rated PCE therefore doesn't represent the actual efficiency of a PV module in operation because temperatures and spectral irradiance vary significantly in different locations and over daily and seasonal cycles. In BIPV systems the disparity from STC is larger than conventional rack mounted systems as they

are typically more poorly ventilated and sub-optimally orientated, resulting in higher operating temperatures and more variation in received irradiance.

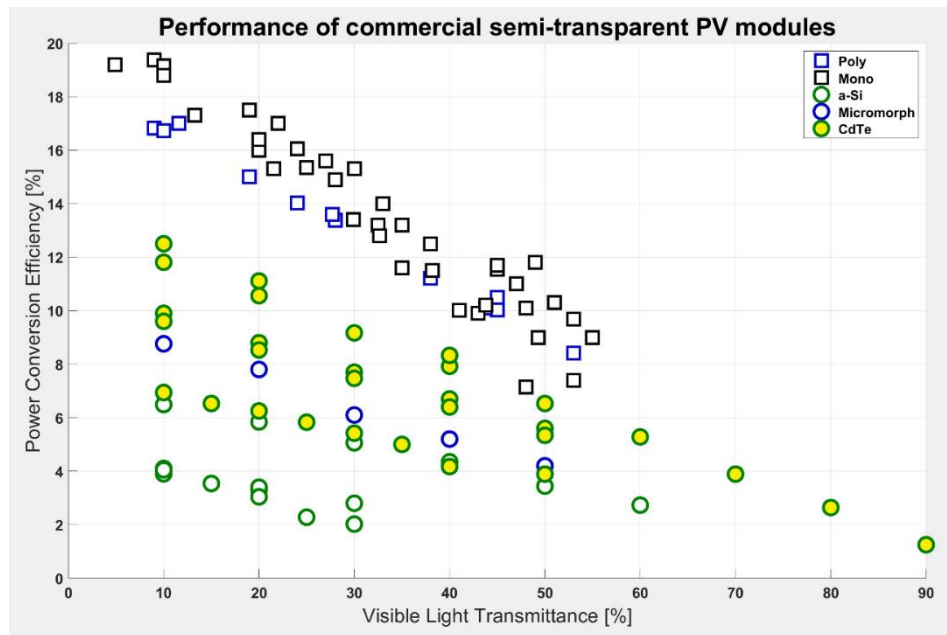


Figure 39: Efficiency data for commercially available semi-transparent PV modules at STC (Data sources listed in Appendix A; Table 21)

Even with added transparency c-Si products provide superior efficiencies up to 50% VLT, with products offered above this transparency being scarce, possibly due to the increased difficulty in spacing the large c-Si cells in an orderly manner. Based on the data in Figure 39 which was taken from BIPV manufacturers the decrease in transparency with increasing efficiency is slightly stronger with c-Si technologies, making it plausible that at high VLTs of around 70% or more CdTe modules may provide the best efficiencies.

Maximum Efficiency	c-Si	a-Si	CIGS	CdTe
Record Opaque Cells ^[1]	26.7 %	10.2 %	23.35 %	21.0 %
Record Opaque Modules ^[1]	24.4 %	12.3 %	19.2 %	19.0 %
Commercial Modules 30% VLT ^[2]	15.3 %	6.1 %	--	9.17 %

Table 3: STC efficiencies of opaque and commercial transparent PV modules and cells (^[1]

Green et al., 2021; ^[2] Table 21)

5.2 Temperature Dependence

The temperature coefficient of a PV cell is the fraction of power output change that occurs for a 1°C increase in cell operating temperature, for all conventional PV materials this value is negative, meaning that power output decreases linearly as temperature rises. Conventional rack mounted PV modules have a nominal module operating temperature (NMOT) of around 45°C (Mittag et al., 2019) so the actual conversion efficiency during operation is lower than the rated value measured under standard test conditions (STC) at 25°C. The temperature coefficient is especially important for BIPV applications because integrated devices can reach much higher operating temperatures than conventional systems due to a lack of rear-side ventilation in certain building elements, additionally the use of a glass backsheet can also raise operating temperatures by 2–3°C compared to conventional modules as the extra rear-side irradiance adds to the total energy absorbed into the PV cells (Sample & Virtuani, 2009; Mittag et al., 2019).

Sample & Virtuani (2009) found that glass-glass BAPV devices with an 8 cm air gap behind the module operated at an average temperature of 61°C in the summer months (Italy) while the same device integrated with no air-gap and a worst case insulative mounting material averaged about 10 degrees hotter at 72°C, the maximum temperature reached by a non-ventilated device was 92 °C which would correlate to approximately 25% reduction in maximum output for a c-Si device. These values are supported by the work of both Ritzen et al. (2017); who found average temperature ranges of about 60 – 70 °C for ventilated and 70 – 85 °C for non-ventilated BIPV roof systems, and Özkalay et al. (2022), who measured 98th percentile temperatures of 59 °C and 80°C for ventilated and non-ventilated glass-glass BIPV respectively.

Parameter	c-Si	Technology a-Si	CdTe	
Temperature Coefficient	0.41 – 0.57	0.10 – 0.30	0.20 – 0.22	[1]
Ranges				[2]
[-%/K].	0.36 – 0.47	0.19 – 0.21	0.2 – 0.28	
Relative power loss operating at 70 °C	-16.2 % to -21.15%	-8.5% to -9.45%	-9.45 % to -12.6 %	[2]
Max PCE at 60°C & 30% VLT	10.26 %	5.2 %	7.80 %	[2]
Max PCE at 85°C & 50% VLT	6.86 %	3.45 %	5.34 %	[2]

Table 4: Temperature coefficients and expected power losses of transparent PV products
(¹Virtuani et al., 2010; ²Table 21)

Thin-film modules have lower temperature coefficients with the median values being approximately $-0.2\text{ }^{\circ}\text{C}^{-1}$ for both CdTe and a-Si, c-Si modules have much higher coefficients, with expected losses at 70°C being almost double that of thin-film, despite this the overall output is still greater with the best c-Si BIPV products outperforming thin-film technologies even in worst case scenarios. High temperature performance is often touted as an advantage for thin-film modules but given the large disparity between efficiencies at STC the advantage is not leveraged until almost 100°C , c-Si products on the market also have a larger variation in temperature coefficients with some newer n-type cells having temperature coefficients of 0.3% or less, not far off modern thin-film modules (Satpathy & Pamuru, 2020). There is still some advantage to the lower coefficient of thin-film modules in that there is much greater consistency in energy generation throughout the day/night and seasonal cycles.

5.3 Irradiance Dependence

The efficiency and yield of a PV module is dependent on the intensity and spectrum of light received, this varies between technologies because of the absorption spectrum of the semiconductor and electrodes, as well as the irradiance dependent resistive characteristics of the cell itself. Further optical effects occur at the module level, with reflection and absorption occurring in the front interfaces and layers of the PV module altering the amount of light that is transmitted completely to the PV cell absorber layer.

5.3.1 Angle of Incidence

The angle at which direct light strikes a solar module has a significant effect on the power generated because of 2 mechanisms, firstly a higher angle of incidence (AOI) will reduce the area of the module perpendicular to direct solar flux, thereby reducing the irradiance incident to module surface, and secondly higher incidence angles result in larger reflective losses at the interface between 2 different optical media as dictated by the Fresnel equations. This behaviour is depicted below in Figure 40 which shows the angle dependent optical loss due to Fresnel reflection (left), and the total power received considering both the Fresnel reflectance loss and incident solar flux. The main factors that can alter AOI effects are the modules optical design (substrate thickness and type, encapsulant selection, anti-reflective coatings) and the orientation of each module.

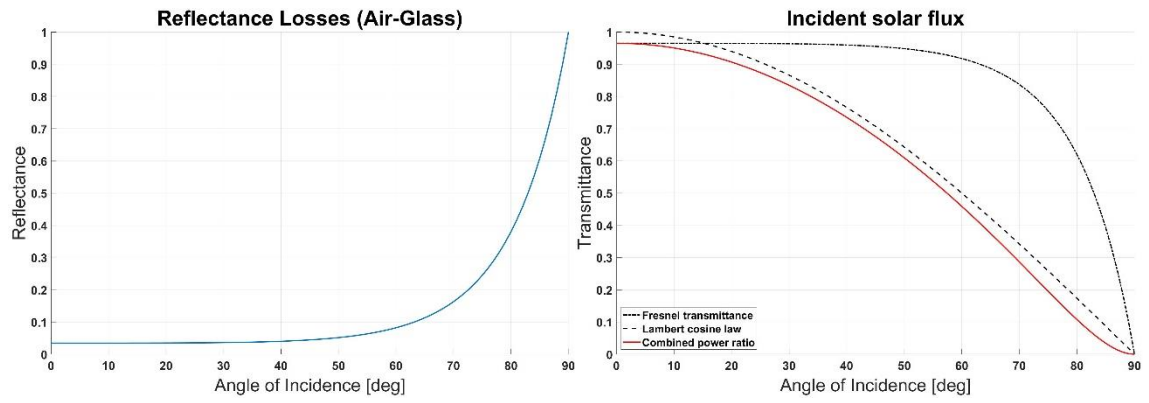


Figure 40: Example of variation in reflectance (left), and in total received power (right)

Typically rack-mounted arrays are mounted at a pre-determined tilt angle that maximizes the system yield by optimizing the average AOI over the course of a year, however control over tilt angle is usually not possible in BIPV applications as the devices must be permanently integrated flush to building surfaces to provide other building functionalities such as weather sealing.

BIPV systems can only be optimized for AOI effects by correctly selecting the faces of a building for BIPV installation that will provide useful energy yield, for example in vertical façades the walls facing away from the equator will have a higher average AOI and hence generate much less energy making them a poor choice for BIPV integration (See Figure 41). A consequence of this is that manufacturers may need to provide low-cost dummy modules that do not generate power but have the same appearance as the active BIPV products to allow a consistent design language throughout the entire building without incurring the cost of installing the expensive BIPV components on a sub-optimal building face (Ballif et al., 2018).

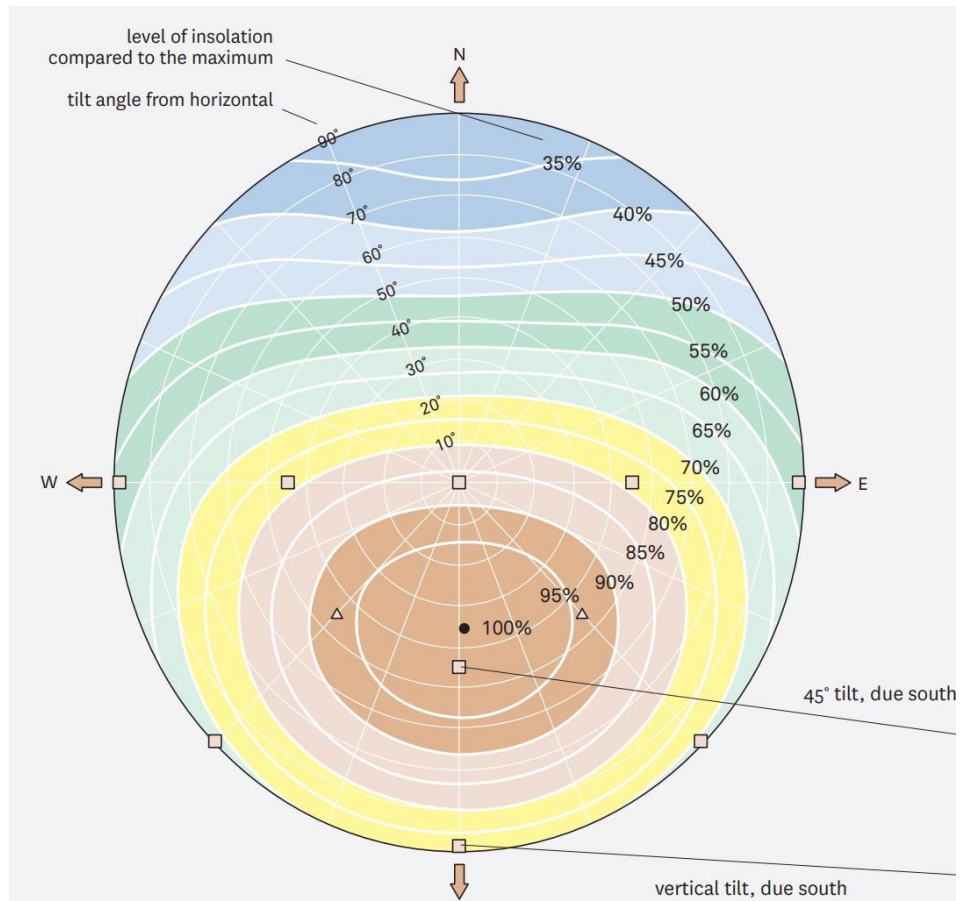


Figure 41: Contour plot of relative yearly insolation received by orientation and tilt angle in the northern hemisphere (Roberts & Guariento, 2009)

Note that in the southern hemisphere maximum generation would occur for north orientations

5.3.2 Low Irradiance & Spectral Response

As a result of internal resistances within the PV cells a reduction in irradiance also reduces the efficiency of the device, this is due to a linear reduction in shunt resistance as the irradiance rises causing increased parasitic losses (Mavromatakis et al., 2017). This effect is more relevant for BIPV as the sub-optimal orientation of devices lead to a higher portion of solar insolation being received at high incidence angles and therefore lower average irradiance. The impact of shunt resistance on low-light performance has another implication for semi-transparent BIPV as some aperture forming processes will decrease the shunt resistance of the cell to some degree (Gečys et al., 2017; Kuk et al., 2019), which could lead to worsened low-light performance.

A study of various PV technologies in US climates found that power losses in rack-mounted systems due to low irradiance were quite minimal, with the majority of modern cell types having between 1-2 % loss, with the main exception being CIGS which tended to be in the range of 5-7% (Marion et al., 2014), although CIGS cells were relatively new in development at

the time and suffered more because of lower shunt resistances that could not yet been improved with manufacturing techniques at the time.

The spectral response of a module also affects the generation under different environmental conditions, location dependent outputs will vary between technologies. Absorber materials with a spectral response more skewed towards blue light (Refer to Figure 42) will perform worse when the air mass (distance sunlight travels through the atmosphere) is higher, this is because the direct solar irradiance contains a lower portion of blue light due to preferential scattering of short wavelength light in the atmosphere (Rayleigh scattering). The air mass is higher when the solar zenith angle is increased, which occurs nearing sunrise/sunset, during winter months, and at lower latitudes. The performance difference is especially evident in a-Si cells which have the highest bandgap, for example a comparative yield study between a-Si and poly c-Si arrays in India revealed that a-Si modules performed 14% better in summer but 6% worse in winter months largely due to spectral effects (Ghosh, 2020).

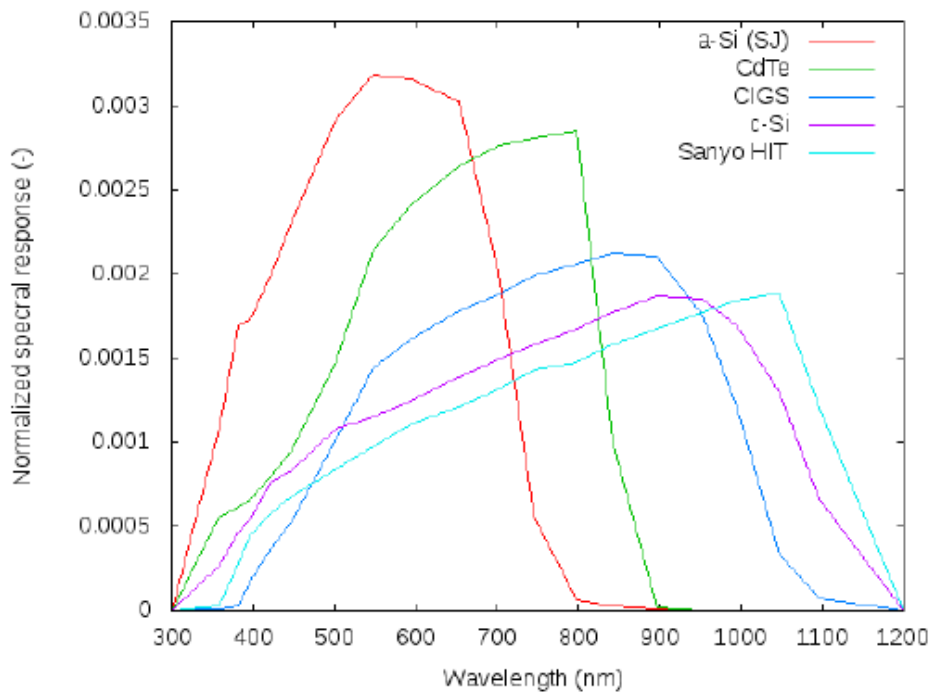


Figure 42: Normalized spectral response of PV technologies

The effect of spectral response can be seen below in Figure 43, where the normalized efficiency of CdTe module can actually increase for low irradiances in certain conditions and locations owing to the improved response to the solar spectrum at low irradiance. The effect on overall power generation tends to be fairly minimal, as demonstrated by Ahsan & Khan (2019) CdTe panels only produced a 1% higher yield than c-Si panels over a 4 year period.

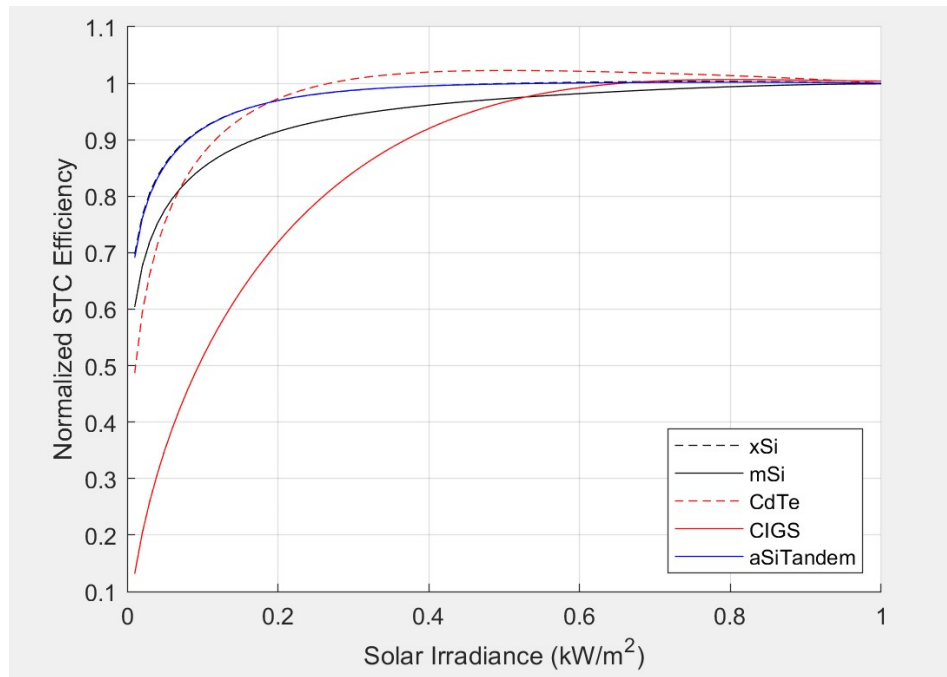


Figure 43: Efficiency vs irradiance, parameters from Mavromatakis et al. (2017)

5.3.3 Shading

The shading effect refers not to the loss of power output due to reduced irradiance, but rather to the additional electrical mismatch losses that occur within a module when part of the module is shaded. Shading at the system level is dependent on the orientation of the BIPV system in relation to nearby structures which could block direct sunlight from reaching modules within the system.

At a module level the resistance to shading is dependent on the configuration of cells, sub-strings, and bypass diodes. For crystalline modules a higher number of bypass diodes and sub-strings will lower the discrete power reductions occurring for an individual cell being shaded but does not guarantee reduced losses for all shadow geometries. Thin-film modules on the other hand are usually considered as being more resistant to shading because of the pinstripe layout of cells within the module, the thin rectangular cell segments within the film are more likely to receive even shading across multiple cells which does not incur shading mismatch losses as the current reduction is roughly equal for each cell, however as seen below in Figure 44 (right) if the shading is parallel to the scribe lines then multiple cells will be completely shaded which could require the entire module to be bypassed.

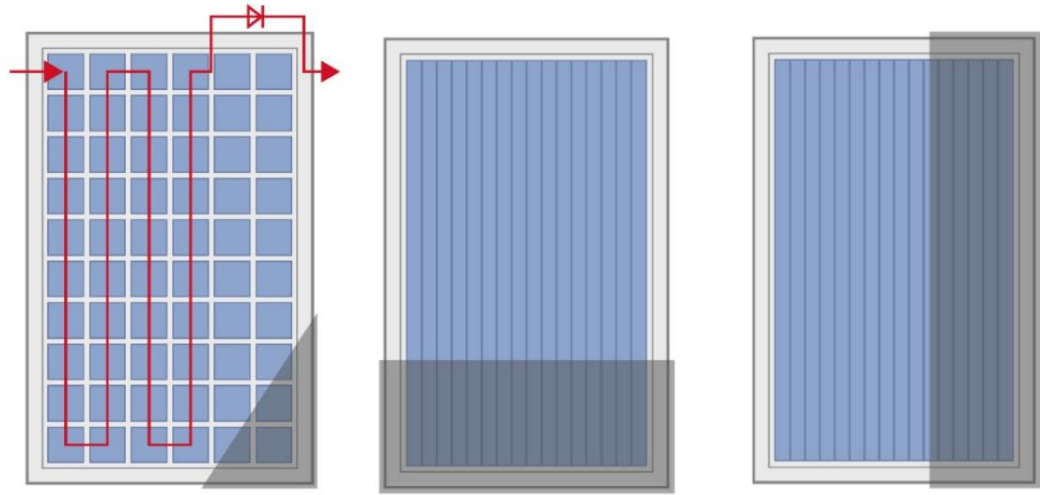


Figure 44: Shading effects on generic c-Si vs thin-film modules (Current travels horizontally in the thin-film diagrams so worst case mismatch losses occur in the case on the right)

5.4 Module Degradation

A photovoltaic lifetime is usually defined as the time at which the power output has degraded to 80% of its rated output, it is essentially a measure of the average linear annual degradation of the module. The annual degradation restricts the overall energy that a PV system can produce over its lifetime as the efficiency gradually decreases, longer module lifetimes are particularly appealing in BIPV as replacement of modules is undesirable due to their complete integration into the building envelope.

The guaranteed 80% output lifespan for conventional EVA glass-foil crystalline modules is usually 25-30 years, with field annual degradation rates of between 0.2–0.6% (Jordan & Kurtz, 2013). Thin-film modules generally have degradation rates closer to 1.0 %/yr as they are more sensitive to moisture, however there are significantly fewer long-term studies on thin-film modules due to longer stabilization periods and their relatively recent emergence into utility scale and residential use (Jordan et al., 2016). Current thin-film modules are capable of providing competitive lifetimes of at least 20-25 years by using module constructions which provide extra resistance to moisture ingress, this still falls well short of what can be achieved using c-Si cells with similar module constructions, of which some manufacturers offer warranties of up to 87% power output after 30 years (CS Wismar, 2020; Aleo Solar, 2020; Solitek, 2021), suggesting an actual 80% output lifetime exceeding 45 years if warranted degradation rates were to remain constant.

Parameter	c-Si	a-Si	CIGS	CdTe	Sources
Module Degradation [%/yr].	0.31 – 0.61	0.87 – 1.25	0.20	0.40 – 1.26	Jordan & Kurtz, (2011); Jordan et al. (2016)
Module Lifetime [yrs].	20 – 30	25	20	20	Ogbomo et al. (2017); Ghosh (2020)
	83 – 87% output after 30 years	80% output after 25 years	n.d.	80% output after 20 – 25 years	Manufacturer Datasheets (Table 21)

Table 5: PV module durability and average degradation rates

Both c-Si and thin-film modules can have extended lifetimes by the use of glass back-sheets, and encapsulants and edge-seal that enhance the resilience to a multitude of degradation modes. Outside of manufacturing defects the encapsulation material of the module is one of the most important factors for limiting degradation rates at the module level. Encapsulants with low transmission rates of oxygen and water vapour help limit corrosion, delamination, and cell degradation, high thermal conductivity is also useful as it cools the module more effectively and lower the rate of thermal ageing in the polymer (Köntges et al., 2014; Schneller et al., 2016).

High electrical resistivity is beneficial in lowering potential induced degradation (PID), which is caused by leakage currents through the encapsulant under high negative bias (>-600 V) leading to migration of sodium ions from the glass into the PV cell. Moisture content and adhesion of the encapsulant also play a part in PID as a lower equilibrium content and high adherence to the glass reduces the formation of conductive leakage paths (Pingel et al., 2010; Satpathy & Pamuru, 2020). Breakdown products are another factor for degradation, as discussed earlier in Chapter 2.3.1 EVA releases acetic acid as it breaks down, which accelerates several degradation modes within the module, utilizing non-crosslinking encapsulants can prevent this as they are much more chemically stable (Sinha et al., 2021).

Encapsulant	Module Type	Guaranteed Output	Warranty Duration
EVA	c-Si	80%	25 years
	Thin-film	80%	25 years
PVB	c-Si	83%	30 years
	Thin-film	80%	20 – 25 years
POE	c-Si	87 – 88 %	30 years

Table 6: Warranty provided by encapsulant material for glass-glass semi-transparent PV (Data from Table 21)

5.5 Embodied Energy and Emissions

Energy payback time (EPBT) is the time required for a photovoltaic array to generate the amount of energy that was originally consumed to produce the system, it is used as a general measure of the environmental impact of manufacturing and installing a PV system by estimating how quickly it can counteract its own embodied energy and begin operating at net zero. The EPBT can vary between locations and system yield and so is typically given as an estimate range for a specific location.

Thin-film technologies have a large advantage as the energy requirements for thin-film deposition are much less intensive than the production of silicon wafers, meaning technologies such as CdTe can achieve EPBTs below 1 year (in optimal PV arrays) while c-Si modules payback times may exceed 3 years due to the energy intensive cell fabrication. It should be noted that these values apply only conventional opaque modules, in the case of transparent BIPV the EPBT will be longer as the systems will have much lower annual yield, while thin-film systems may also have marginally increased EPBT due to the additional energy consumption required for the P4 laser scribing process.

The EPBT does not fully encompass the environmental impact as energy consumption for manufacturing may be partially drawn on from renewable sources. A more general measure of environmental impact is the embodied emissions, which is the CO₂ equivalent weight of emissions released for the manufacture of PV modules, this includes all activities required for the production cycle of the module including material extraction, processing, manufacturing and logistics and provides a more direct means of comparison to other building materials when considering environmental factors.

	c-Si	a-Si	CIGS	CdTe
Energy Payback Time [yrs].	3 – 4	2 – 3	1 – 2.4	0.75 – 2
Embodied carbon [gCO₂-eq/kWh].	45	50	46	35

Table 7: EPBT & embodied CO₂ equivalent emissions of PV technologies (Ogbomo et al., 2017; Ghosh, 2020)

5.6 Manufacturing Feasibility

Each PV technology presents its own unique challenges and benefits for BIPV, in order for successful integration of semi-transparent BIPV manufacturing into a laminated glass production line the specific manufacturing process must be both compatible and economically viable.

5.6.1 Crystalline Silicon

Transparency is easily added to modules with minimal adjustment to conventional designs and can be done with regular c-Si cells, modern tabber-stringers can easily adjust to different cell and ribbon sizes and interconnect schematics, making the addition of cell gaps for transparency very simple. Module manufacturing does not need to take on the production of PV cells and is much less capital intensive because of this, relying on third parties for cell production reduces the risk of falling behind in module performance, compared to thin-film technologies in which innovation by competitors could rapidly outdate manufacturing processes.

5.6.2 Copper Indium Gallium Selenide

Due to the high thermal conductivity and low melting points of the metals in CIGS it is not possible to laser scribe a P4 aperture in a cost efficient manner without partially fusing the material near the edge of the apertures and causing significant shunt defects (Kuk et al., 2019), this means that CIGS is completely unviable for transparent BIPV using the P4 scribe method. Creating transparency using a UTF architecture may still be possible, however it does not seem beneficial to do so, of 200 international BIPV manufacturers none produce transparent CIGS products (Table 21).

As an opaque product CIGS does have some merits, including relatively high efficiencies, high future potential and the potential to eliminate toxic materials (CdS & H₂Se) from current manufacturing process with minimal loss. This is still not optimal for BIPV as the ideal PV technology allows for creation of both opaque and transparent products on the same production line, additionally high manufacturing costs (See Figure 45) further limit the commercial viability as high end-user costs are a major barrier to wide-spread adoption of BIPV (Ballif et al., 2018).

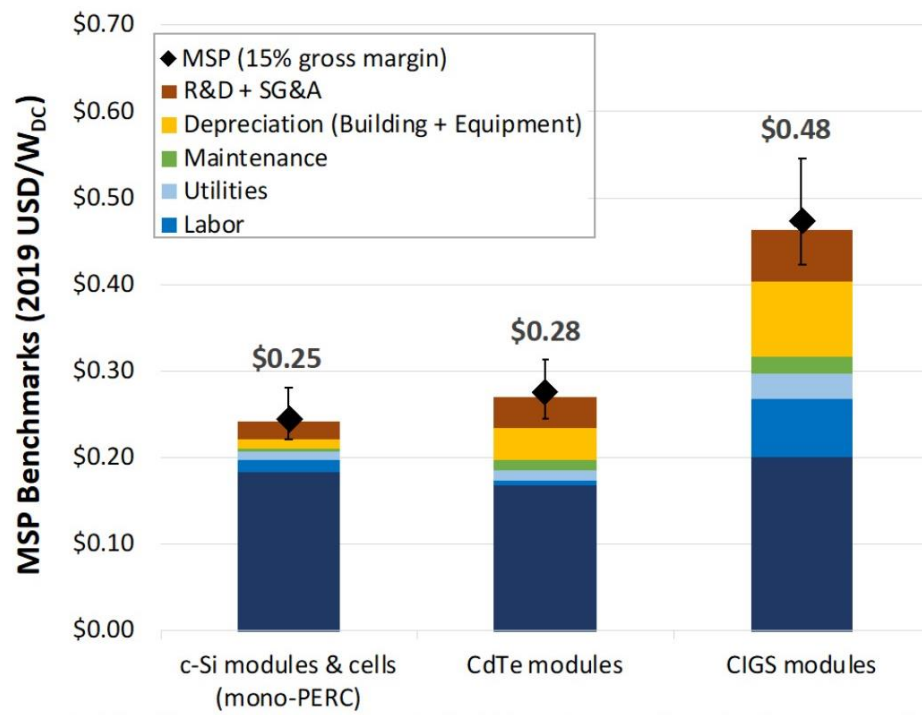


Figure 45: Minimum selling price for commercial module technologies (Smith et al., 2020)

5.6.3 Cadmium Telluride

CdTe has a low environmental footprint, low manufacturing costs, high module efficiencies, and a high potential for future development. Nonetheless there are still some drawbacks to incorporating CdTe manufacturing into a laminated glass production line.

Cadmium is a very hazardous chemical and as such safe exposure limits are imposed, this necessitates vigilant practices to control the exposure risks to workers (Fthenakis & Zweibel, 2003). This could be a drawback for integration into a pre-existing laminated glass production space, as the hazards arising from handling and transport of CdTe could impose stringent restriction on workers from other production lines, adding time and cost to these unrelated processes. Handling of CdCl₂ for post-deposition treatment could also present an issue since it is an acutely toxic and carcinogen material, although alternative chlorine treatment gases with much lower toxicity have been proven successful at a laboratory scale (Başol & McCandless, 2014; Romeo & Artegiani, 2021).

The public perception of cadmium toxicity also stands to hinder the success of CdTe BIPV devices, although the risks associated with completed modules are very low as CdTe compounds are much less hazardous than elemental cadmium, and once encapsulated do not pose any risk, as low vapour pressures and high melting temperatures make it unlikely that a dangerous amount of inhalable compounds could be released even in the case of module breakage or fire (Fthenakis & Zweibel, 2003).

As discussed earlier the strain point of soda-lime glass limits the process temperature for CdTe deposition to about 500 °C or below, in addition to this the high process temperatures necessary for CdTe deposition would destroy any heat-strengthening in the glass (Roberts & Guariento, 2009), as it would essentially relieve the surface compression once brought up to high temperatures. This is a major drawback for BIPV glazing as it prevents the manufacture of conventional tempered glass laminates to achieve certain design requirements, instead the CdTe must be deposited on regular float glass and then laminated between 2 sheets of tempered glass to achieve high toughness.

5.6.4 Amorphous Silicon

Amorphous silicon is one of the first technologies to be used in transparent PV cells (Takeoka et al., 1993), manufacturing process for a-Si are mature, low-cost and non-toxic, and transparency can be easily added using both a-type and UTF film architectures.

Of the thin-film technologies a-Si seems the most convenient for co-location of both glass lamination and PV cell deposition processes as it does not require the handling of toxic materials, low efficiencies are definitely a drawback but micromorph or triple-junction devices are capable of providing PCEs not far from CdTe (Table 3) at similar manufacturing costs.

The PECVD deposition method for a-Si can be conducted at much lower temperatures than that of CdTe, which could allow the use of heat-treated glass as a deposition substrate to create fully tempered glass-glass BIPV devices. Of the thin-film semi-transparent PV product analysed in Appendix A the only product to offer double heat-treated glass was an a-Si based (micromorph) device.

5.7 Summary

Technology	Strengths	Weaknesses
c-Si	<ul style="list-style-type: none"> • Low manufacturing costs • Stable industry • Immediate adoption of new cell technology • Superior module durability and lifetimes 	<ul style="list-style-type: none"> • Aesthetic appeal • Susceptible to shading effects • Power output varies significantly with temperature • Cells susceptible to mechanical damage during manufacturing and handling
a-Si	<ul style="list-style-type: none"> • Non-toxic manufacturing • Aesthetic products • Simple and well established manufacturing procedures 	<ul style="list-style-type: none"> • Small potential for future improvements • Worst in class module efficiency • Susceptible to light induced degradation
CdTe	<ul style="list-style-type: none"> • Aesthetic products • High efficiency • Low cost manufacturing • Lowest energy payback time • Lowest embodied carbon 	<ul style="list-style-type: none"> • Handling of toxic materials required • Public perception of Cadmium • Some processes for high efficiency manufacturing may be proprietary • Manufacturing procedures subject to change in industry • High process temperature prevent use of heat-treated glass as a substrate
CIGS	<ul style="list-style-type: none"> • High efficiency • High potential for future efficiency improvements • Potential for non-toxic manufacturing 	<ul style="list-style-type: none"> • No current methods of effectively adding neutral colour transparency • High manufacturing costs • Use of rare Indium metal

Table 8: Comparative benefits of PV technologies for BIPV manufacturing

6 Prototype Development

This chapter describes the procedures leading to the detailed design and fabrication of a BIPV prototype that provides a sufficiently accurate representation of a full-sized BIPV product. An overview of the key international certifications and guidelines that must be followed during the design procedure is also included.

6.1 BIPV Compliance and Guidelines

PV certification is attained by compliance with international PV standards verified by a certification body, additional requirements outlined in ISO standards or national codes which are relevant to the installation and use of PV modules in their intended locations also need to be considered (BSI, 2018a).

The most common internationally adopted PV certification scheme is the IEC standard sets IEC 61730 and IEC 61215 for design and safety qualification of terrestrial flat plate modules. The two standards are designed to coordinate so that a single set of sample modules can be used to perform both qualifications, they do not address any requirements for combining PV modules with power conversion equipment nor do they address the individual components within a PV module. IEC 61730 defines the construction requirements and type tests necessary to provide safe operation by prevention of electrical, mechanical or environmental failure which could result in fire or personal injury. While IEC 61215 sets requirements for design qualification to verify suitability for long-term operation (BSI, 2020b). Part 1 of this standard also contain additional sub-parts which define specific requirements for different photovoltaic technologies.

To certify PV products for integration into buildings the device must also comply with all the relevant local construction requirements relating to structural design, installation, and electrical safety alongside the PV certification. This has been a significant barrier for BIPV due to a lack of internationally recognized BIPV building codes, making it more complex to gain certification for a BIPV product that can be sold and installed in multiple countries as well as making it difficult to certify BIPV products according to one clear prescriptive approach (Ballif et al., 2018; Corti et al., 2020). In an attempt to unify both PV and building requirements the IEC created a BIPV specific standard (IEC 63092:2020) which specifies additional fire safety, mechanical resistance, noise, and energy performance requirements related to the building functionalities provided by BIPV products. IEC 63092 still does not provide a completely harmonized international approach as BIPV modules will still be required to comply with local codes, and in many cases the standard itself calls on national building codes primarily, or in combination with ISO standards, to cover certain functional requirements (IEC, 2020).

Application category	A	B	C	D	E
Mechanical resistance and durability	IEC 61215-1 and IEC 61215-1-X based on relevant cell material IEC 61215-2 IEC 61730-1, IEC 61730-2 ISO 12543-2 (Laminated safety glass), ISO 12543-3 (Laminated glass), ISO 12543-4, ISO 12543-5 IEC TC 63126 Annex A				
Safety in case of fire	No requirements are specified				
Hygiene, healthy and the environment	No requirements are specified				
Safety and accessibility in use	IEC 61730-1, IEC 61730-2 ISO 28278 (Structural sealant glazing) ISO 29584				
Protection against noise	ISO 16940, ISO 22897				
Energy economy and heat retention	ISO 9050 and/or ISO 10293				
	ISO 10291 and/or ISO 10292 and/or ISO 10293				
				ISO 19467	ISO 52022-1 ISO 52022-3
Sustainable use of natural resources	No requirements are specified				
Note: National or local building-related codes or standards may apply					

Table 9: Requirements from IEC 63092-1:2020 for BIPV modules containing at least one glass pane, application categories refer to those in Table 1 (IEC, 2020)

Another significant certification obstacle for BIPV products are the PV retesting requirements (PD IEC TS 62915) which dictate that previously IEC 61730/61215 qualified PV module designs be requalified under certain design changes such as 20 % change in a module dimension (BSI, 2018c). These requirements are written with conventional PV modules and applications in mind where notable changes in design typically do not occur during the run of a product series, in contrast a very specific challenge of BIPV products is the large variation in sizes and designs that are needed to meet architectural requirements, these requirements makes custom BIPV modules more expensive due to additional testing and certification costs of non-standard sizes and designs (Wilson et al., 2020).

A requirement of both IEC 63092 and 61215 that is especially relevant for BIPV is compliance with IEC TS 63126:2020 to verify module safety, durability and performance of PV modules operating under elevated temperatures that are not covered by the scope of IEC 61215 and 61730. This specifically applies to modules with 98th percentile operating temperatures exceeding 70 °C, meaning that temperatures are expected to exceed this value for at least 2% of each year or operation period (IEC, 2020), as discussed in Chapter 5.2 the maximum operating temperature of non-ventilated BIPV readily exceeds 70 °C, with even ventilated vertical components reaching a 98th percentile temperature of around 60 °C (Özkalay et al., 2022).

Document	Name	Scope
IEC 63092-1:2020	Photovoltaics in buildings – Part 1: Requirements for building-integrated photovoltaic modules	Requirements for use of non-concentrating photovoltaic modules as building products
IEC 63092-2:2020	Photovoltaics in buildings – Part 2: Requirements for building-integrated photovoltaic systems	Requirements for photovoltaic systems that are integrated into buildings, specifically mounting method and structures
IEC 61730-1:2018	Photovoltaic (PV) module safety qualification – Part 1: Requirements for construction	Construction requirements to provide safe electrical and mechanical operation
IEC 61730-2:2018	Photovoltaic (PV) module safety qualification – Part 2: Requirements for testing	Testing requirements and sequence to verify safe operation of PV modules
IEC 61215-1:2021	Terrestrial photovoltaic (PV) modules – Design qualification and type approval – Part 1: Test requirements	Requirements for design qualification of non-concentrating terrestrial PV modules exposed to open-air climates
IEC 61215-2:2021	Terrestrial photovoltaic (PV) modules – Design qualification and type approval – Part 2: Test procedures	Define testing procedures and sequences for proof of resistance to prolonged outdoor exposure.
PD IEC TS 63126:2020	Guidelines for qualifying PV modules, components and materials for operation at high temperatures	Define additional testing requirements for module with 98 th percentile operating temperatures that exceed 70 °C
PD IEC TS 62915:2018	Photovoltaic (PV) modules – Type approval, design and safety qualification – Retesting	Define test sequences to maintain type approval and qualification for PV modules that have been modified from the originally qualified design
AS/NZS 3000:2018	Electrical installations	Requirements for the design, construction and verification of electrical installations.
AS/NZS 4777.1:2016	Grid connection of energy systems via inverters – Part 1: Installation requirements	Specifies the electrical and general safety installation requirements for inverter energy systems (≤ 200 kVA) connected to the grid
AS/NZS 5033:2021	Installation and safety requirements for photovoltaic (PV) arrays	General installation and safety requirements for electrical installations of PV arrays.

Table 10: Summary of key PV standards and guidelines relevant to glass-glass BIPV in NZ

6.1.1 Laminated Glass Design Methods

BIPV products must comply with the New Zealand building code and meet all standards relevant to the material and building functionality provided, for glass-glass BIPV this entails compliance with NZS 4223 Glazing in Buildings, which sets out design procedures for the selection of glasses for internal and external glazing installed in buildings.

In NZS 4223.1:2008 determination of the stress in each sheet of laminated glass can be calculated using a simple method which assumes proportional load sharing based on the thickness ratios and number of glass sheets in the laminate, and for short and medium-term load durations the simplified method specifies that the total minimum glass thickness of the laminate be used for further calculations (Standards New Zealand, 2008). Alternatively a complete non-linear analysis of the glass-interlayer behaviour may be undertaken.

The method of NZS 4223 for short term load durations is practical for the moderate levels of shear bonding usually occurring in laminated glass, however at high temperatures the reduced shear transfer through interlayer means this is no longer suitable, as seen below in Table 11 even at 50 °C the reduced shear stiffness of the EVA encapsulant means that both effective thicknesses are already less than calculated by the standard method, implying that the simplified method of NZS 4332.1 would underestimate glass deflection and stress under this loading condition. Methods and further results for these stress calculations are presented in Appendix B.

Interlayer	NZS 4332.1:2008 Clause 3.4.1.a	Deflection Effective thickness	Stress Effective Thickness
EVALAM Visual (25°C)	7.7 mm	7.85 mm	8.51 mm
EVALAM Visual (50°C)	7.7 mm	6.22 mm	7.04 mm
Kuraray Trosifol Clear (80°C)	7.7 mm	5.66 mm	6.42 mm

Table 11: Comparison of stress effective design thickness of laminated glass under short term (Standards New Zealand, 2008; Kuntsche et al., 2019).

Note: Load duration ≤ 3 seconds, 1000 mm glass span, 4/1.52/4 mm laminate

The application of NZS 4223 for the design of glass-glass BIPV laminates should therefore use a complete linear analysis including shear interactions of the interlayer and time-temperature dependent elastic properties to ensure correct specification of glass thicknesses for the high temperatures in BIPV devices. IEC 63092 specifies that rigidity of laminated glass in BIPV modules be calculated using the upper temperature limit of the interlayer calculated from a solar energy balance, or if no values are available 85 °C shall be taken as the upper limit for BIPV with rear insulation, and 65 °C as the limit for modules with no rear-side insulation. These values are not the maximum expected values and consider that the maximum thermal loads are unlikely to occur in conjunction with ultimate mechanical loads due to wind cooling the PV panels (IEC, 2020).

6.2 Prototype Design

IEC standards recommend that mini-modules (used for the purpose of edge seal testing), should use at least one discrete cell and use the same bill of materials and same perimeter construction as a full-sized module (BSI, 2020b), while representative modules sample should maintain the same encapsulation methods, interconnects, terminations, edge distances and insulation distances as actual sized modules (BSI, 2021a).

6.2.1 Module Type Classification

Prototype modules were categorized according to the pre-defined construction requirements of IEC 61730-1:2018 (BSI, 2018a) to ensure that they provide a suitable level of safety for operation and testing and will be representative of full-sized BIPV modules wherever feasible. The module classifications are discussed below with justification of any assumptions.

- PV modules are classified according to IEC 61140 by the accessibility of the module in its installed location, for the purpose of being suitable for nearly all BIPV applications a class II rating is taken. This is the highest hazard situation where the module is in an unrestricted access area and the voltage ratings are considered to be hazardous (greater than 35 V DC), most BIPV installations will fall under this category as the building elements are often accessible either internally or externally.
- Pollution degree (PD) is a measure of the expected conductive pollution in the micro-environment of the PV module, a higher pollution degree means more environmental particles and moisture that create conductive paths within the module. Pollution degree 3 is specified as the base rating for the macro-environment of a PV module however this can be reduced to degree 2 for encapsulated components should the requirements of IEC 61730-2, excluding test sequence B.1, be met (BSI, 2018b). Degree 2 is selected to best represent a qualified full-sized product design.
- Comparative tracking index (CTI) is a measure of the encapsulants resistance to surface electrical breakdown, it is significant for preventing tracking along the encapsulant interfaces which could create leakage paths and reduce insulation resistance. For the purpose of selecting insulation distances IEC 61730 separates CTI into 4 groups in accordance with IEC 60112, a slightly conservative assumption of material group II is made to account for the lack of CTI ratings on the datasheets of interlayers provided for laminated glass (EVA products for PV lamination usually receive the highest rating of Group I).

- IEC 61730-1 also requires specification of module and system voltages in order to prescribe insulation classes, the maximum system voltage is the highest allowable potential within a PV system and is taken to be 1000 V DC which is the maximum allowed for PV arrays installed on buildings as specified in IEC 62546 clause 6.1.1. The maximum working voltage is defined as the maximum voltage that can occur between live parts of different potential within a PV module, based on the values given in IEC 61730-1 the maximum was selected as 100 V DC because standard sized module voltages typically exceed the next lowest value (35 V DC).

Module Class (IEC 61140:2016)	Pollution Degree (IEC 60664-1:2020 Clause 4.5.2)	Tracking Index (CTI) (IEC 60112:2020)
0: Modules having hazardous voltages in areas of restricted access	Degree 1: No conductive pollution occurs	Material Group I: $600 \leq \text{CTI}$
I: Modules of hazardous voltage levels with special installation measures required	Degree 2: Only non-conductive pollution occurs that is occasionally caused to be conductive by condensation	Group II: $400 \leq \text{CTI} \leq 600$
II: Modules having hazardous voltages in non-restricted access areas.	Degree 3: Conductive pollution occurs, or dry non-conductive pollution occurs which becomes conductive due to condensation	Group IIIa: $175 \leq \text{CTI} \leq 400$
III: Modules inherently protected by limitation of voltage to below hazardous levels	Degree 4: Continuous conductivity occurs due to dust or moisture	Group IIIb: $100 \leq \text{CTI} \leq 175$ (not suitable for use in PD 3 modules at system voltages greater than 600 V)

Table 12: Summary of prototype classification according to IEC 61730-1:2018

6.2.2 Insulation Class

From the previously determined design classifications the required level of insulation for module components can be taken from table 3 of IEC 61730-1:2018, following this standard design procedure should mean prototype modules are suitable for exposure to the elevated voltages expected in actual operation of full-sized modules of the same classification, allowing for future testing of insulative capabilities of the prototypes.

Insulation for class II modules requires protection against direct contact, basic insulation between live parts of different potential, and reinforced insulation between live parts and

accessible surfaces (BSI, 2018a). The distances relevant for insulation between live parts are defined as either creepage or clearance distances, creepage is the shortest distance between 2 conductors along the surface of an insulator, while clearance is the shortest path insulated by air between said conductors, an example of both insulation distances is illustrated in Figure 46.

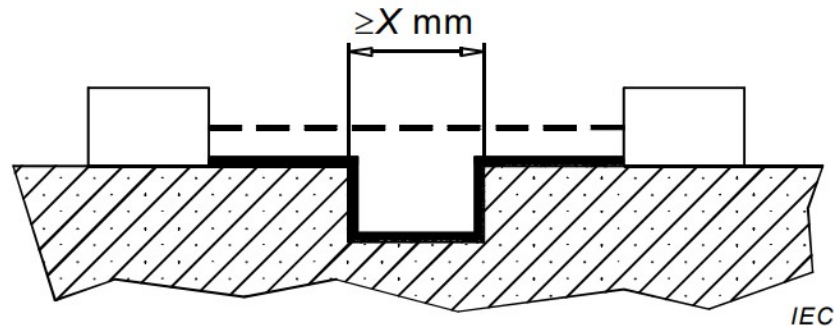


Figure 46: Creepage (solid line) vs clearance (dotted line) distances between 2 conductors (BSI, 2018a)

For prototype design clearance values were ignored as the design did not permit the separation of conducting surface by air only, all internal circuitry is completely in contact with encapsulant therefore only creepage distances are relevant. Likewise the insulation distance for terminals and cemented joints were not needed as these apply to junction boxes and edge seals which are not included in prototypes for reasons later discussed.

All remaining relevant insulation distances are taken from IEC 61730-1:2018 Table 3 according to the specified module class, material group, CTI rating and working or system voltage.

- The creepage distance X between live parts of different potential inside the PV module must be greater than or equal to 1.0 mm
- The creepage distance Z between internal live parts and accessible outer surfaces must be greater than or equal to 14.2 mm
- The thickness of thin layers (encapsulant sheet) within the PV module must be greater than 0.15 mm

These insulation distances apply to the regions of the PV cell interconnection as detailed below in Figure 47.

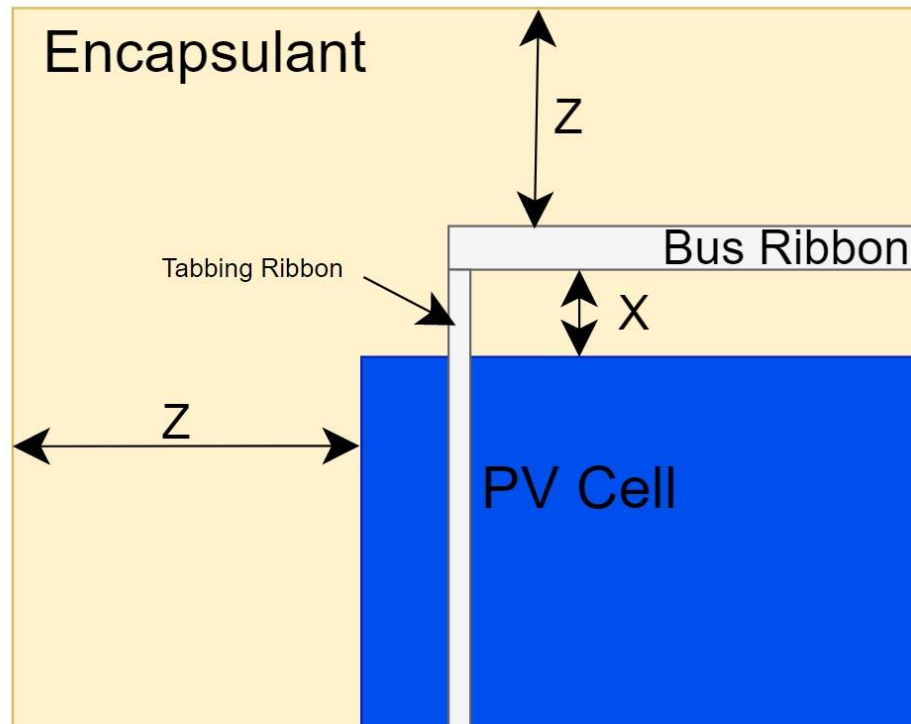


Figure 47: Locations for minimum creepage distance

6.2.3 Photovoltaic Cells

As discussed in Chapter 5.7 both crystalline silicon and thin-film are viable technologies for full scale production of BIPV product, however within the scope of this project there are issues restricting the use of thin-film technologies. The equipment cost and complexity of thin-film manufacturing is such that a collaborative effort would be required in order to fabricate thin-film BIPV prototypes. According to ENF Solar Ltd. (n.d.), which currently lists around 40,000 photovoltaic manufacturers worldwide, there are currently no known producers or distributors of thin-film photovoltaic products located in New Zealand. Without the possibility of local collaboration the use of thin-film cells for prototypes is impractical for initial prototypes, crystalline-silicon on the other hand does not have the same restrictions as cells can readily be purchased and all fabrication processes can be done manually at low cost and with little prior experience.

Irrespective of this limitation it still appears most beneficial to focus on c-Si cells as they present a higher technical challenge for the lamination process, which is the primary focus of this research, whereas the challenges that would arise from fabricating thin-film BIPV modules would be largely related to the manufacturing of the film itself.

125 x 125 mm² pseudo-square poly-crystalline with 2 front and rear busbars were selected for the PV cells, the smaller size choice was rather arbitrary and mainly came down to supplier

options, the use of 2BB cells was done to reduce the difficulty of manually soldering the interconnect ribbons, and in doing so lower the variation in the quality of electrical connections. A polycrystalline cell was chosen to minimize costs as absolute module efficiency is not relevant within the scope of testing. Prototypes will consist of a single cell to reduce the variation in performance due to interconnect quality and absence of cell mismatching effects, this allows the effects of lamination procedures on the PV cell itself to be more easily isolated.

6.2.4 Cell Interconnection

The design arrived at for the interconnect scheme is presented below in Figure 48, it creates a positive and negative terminal while minimizing the length of ribbon required and allowing for ease of electrical testing. A distance of 5 mm between the cell and bus ribbon creates ease of soldering, prevents short circuiting, and allows for thermal expansion (Satpathy & Pamuru, 2020), this distance also well exceeds the 1.0 mm creepage distance required for insulation between live parts within the module. The border thickness of 15.0 mm meets the minimum insulation thickness requirements from IEC 61730-1:2018 and limits the minimum glass dimensions to 155 x 175 mm.

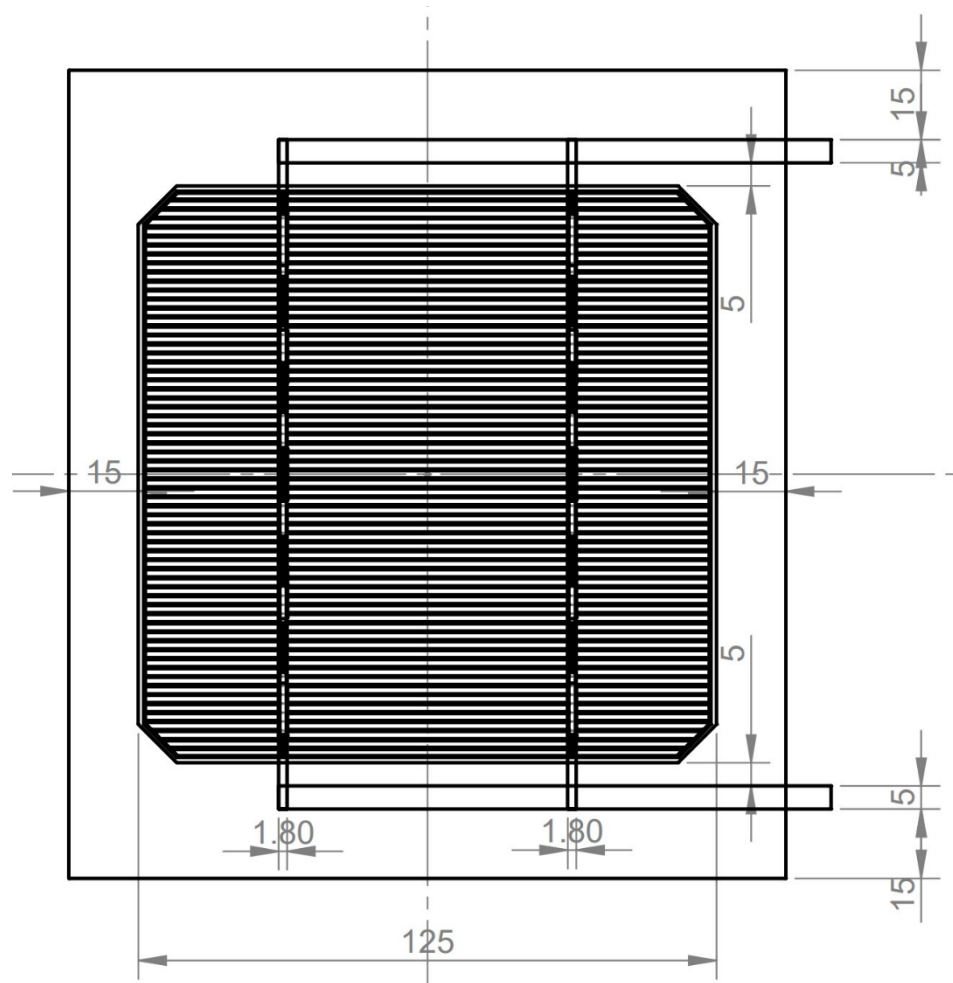


Figure 48: Prototype cell interconnect 2D CAD drawing with minimum insulation requirements dimensioned

The interconnect ribbon has a significant impact on the stress induced in PV cells during the both the soldering and lamination cooling procedure, high stresses are induced in both the interconnect and cell during cooling from high temperatures which can cause cell breakage or interconnect damage. Lower yield strength interconnect ribbon can reduce cell breakage by allowing more elongation under thermal stresses, this has more of an impact in reducing the breakage rates than the thermal expansion coefficient of the ribbon (Schneller et al., 2016; Satpathy & Pamuru, 2020). Additionally thinner tabbing ribbons can also further reduce cell cracking, because they increase the uniformity of thermal contraction in the encapsulant above the cell and minimize cell bending (Rowell et al., 2018).

A conventional front-back tabbing and stringing configuration was used with tin-silver (96.5Sn 3.5Ag alloy) solder-coated ribbons, the tabbing ribbon dimensions are 1.8 x 0.15 mm and bus ribbons 5.0 x 0.18 mm. These ribbons are slightly thinner than standard ribbons thickness of 0.2 – 0.5 mm, which should help to alleviate some of the thermal contraction effects mentioned above.

6.2.5 Encapsulant

Due to the necessity for a BIPV product to meet both PV module and laminated safety glass requirements the encapsulant selection is mostly limited to the materials that overlap both fields. Alternative materials from either industry lack necessary qualities to make competitive BIPV devices, the exceptional stiffness of Ionomer is a detriment for BIPV, as this causes a large transfer of stresses into the PV cells under load, while POE has certain exceptional properties but is expensive and shows high susceptibility to UV ageing (Sinha et al., 2021).

Both EVA and PVB have properties that can apply to both laminated glass and PV modules, and are used in each industry to some extent, however for a module design without an edge seal the high water absorption of PVB rules it out. Even with the previously mentioned downsides of EVA it is still the optimal choice for low cost glass-glass BIPV, in addition to this a VBO process is used which is not well suited to PVB due to the high water vapour content usually requiring an autoclave process to prevent voids forming.

EVALAM Visual UV+ is the selected encapsulant material, it is a UV blocking and high adhesion EVA for laminated safety glass (Pujol Group, 2020). EVALAM is supplied in sheets of standard thickness ($0.38 \text{ mm} \pm 5\%$), of which 4 will be used per module (2 on each side of the cell) to create a total encapsulant thickness of 1.52 mm.

The use of a thick encapsulant layer is very beneficial for the protection of PV cells because it reduces the amount of shear forces transferred into the cell and lowers the risk of breakage during mechanical loading, Rowell et al. (2018) found that adding just one additional encapsulant layer to PV laminates could double the amount of force required to fracture the PV cells inside, furthermore the benefit of thicker encapsulants is even more useful at the higher temperatures expected in a BIPV module because the encapsulant stiffness is very low and so the encapsulant thickness dominates the shear transfer behaviour (Dietrich et al., 2010). In addition to this a thicker encapsulant is better for laminating uneven surfaces, as there is more material for filling voids or unevenness, which is useful for filling in the geometry of the cells and interconnects as well as the physical distortions in the tempered glass caused by roller wave.

6.2.6 Module Glass

A nationally compliant BIPV product has to be able to withstand the live loads expected for the building type and location as specified in NZS 4223 Glazing in Building, as well as the uniform static (2.4 kPa), non-uniform static (5.4 kPa), and dynamic loads tests ($\pm 1 \text{ kPa}$) of IEC 61215-2 (BSI, 2021b). It is expected that heat-strengthened or tempered glass must be used in the

majority of BIPV glazing to pass the PV load tests and meet the requirements of NZS 4223 when taking into consideration the high operating temperatures of BIPV.

With respect to prototype design and testing the use of tempered glass is slightly limited due to the following factors.

- Tempered glass is treated in a furnace with standard roller widths, therefore glass sizes smaller than the roller-roller distance of 250 mm cannot be produced.
- The surface compression stress field of tempered glass means it cannot be cut, which makes it impossible to cut samples from the prototypes for further testing

For this reason it is beneficial to use annealed glass for the purpose of either producing some prototypes below the minimum size limit for tempered glass, or to allow samples to be later cut from the prototypes. But for all other prototypes tempered glass should be used to lower safety hazards of potential glass fracture occurring during handling and testing.

4 mm soda-lime glass was used for both the front and rear glass, two sizes were specified: one of dimensions 155 X 175 mm with no heat-treatment to closely meet the minimum insulation distances (Z) in Figure 48, and another with a tempered design and the minimum heat-treatable size of 250 x 250 mm. Symmetrical glass thicknesses are used as this helps to prevent warpage during lamination, reducing stress on the PV cells (Cattaneo et al., 2015). The use of low-iron glass, texturizing or glass coating was deemed unnecessary as these features are typically only used for improving the optical properties of PV modules to maximise efficiency which is not relevant at this stage.

6.2.7 Excluded Components

Certain components of a PV module were excluded from the prototype design to reduce complexity and cost when they did not have a significant effect on the lamination process or electrical safety of the prototypes.

- An edge seal was deemed unsuitable as it would significantly raise the complexity of lamination and introduce many unknown variables into the process.
- A junction box will not be included in the prototype design for simplicity, as the function is mainly to host the diodes required for full sized modules, with a single-cell layout no bypass diode is required.
- Prototypes will not be framed as this is only relevant for mechanical performance of full-sized modules.

6.2.8 Fabrication Procedure

Tabbing and stringing was carried out by manual handheld soldering with a rosin flux applied by pen for cleaning and wetting of the busbar surface, a solder temperature of about 300 °C was used. After soldering the excess flux and other residues are removed by cleaning the cells with high purity isopropyl alcohol to prevent any adhesion issues during lamination. An example of soldered and cleaned PV cells ready for lamination is captured below in Figure 49.

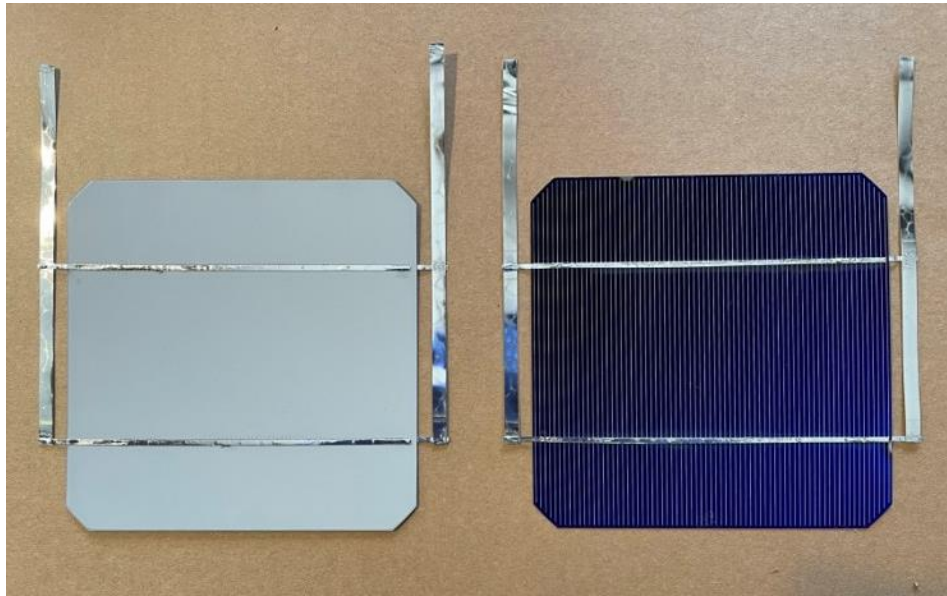


Figure 49: Soldered PV cells

The module ‘lay-up’ is then formed by layering 4 mm glass/0.76 mm EVA/PV cells/0.76 mm EVA/4mm glass. Once aligned the laminates are taped around the edges to minimize encapsulant squeeze out and laminated in a LamiFlex LF4500 glass lamination oven. Standard cycle parameters recommended by the interlayer manufacturer for 4mm/4mm glass thickness are used, with a set cure temperature of 135 °C, Prototypes were fabricated in 4 separate batches, for the separate purposes of initial trial runs, physical inspection testing, annealed glass trial runs, and cell characterization testing. A total of 4 annealed and 14 tempered modules were made.

Lamination Stage	Hold Time	Target Temperature
Preheat	90 minutes	70 – 90 °C
Cross-linking	50 minutes	135 °C
Cool-down	30 minutes	50 °C

Table 13: Lamination cycle parameters

7 Experimental Testing

This chapters covers the experimental tests conducted to assess whether the standard vacuum bag only lamination process can successfully laminate the designed BIPV prototypes without causing major laminate defects or damage to the PV cells.

7.1 Testing Overview

A testing methodology was developed to detect very small changes in the cells condition by comparing the electrical parameters of each cell before and after the lamination process is complete. Changes in electrical parameters can be associated with particular physical defects that could occur during the lamination process. In addition to this an inspection of each prototype was conducted to detect any major visible defects that could indicate poor lamination quality.

Test Section	Purpose
Physical inspection	Visual and dimensional inspection of prototypes will allow detection of bubbles, voids, warping, and other dimensional inconsistencies which could negatively affect adhesion, moisture ingress and electrical isolation.
Cell characterization	Characterization of the cells electrical parameters will allow detection of any mechanical damage occurring to the cell or circuitry during the lamination process

Table 14: Testing methodology

7.1.1 Prototypes Manufactured

A total of 17 complete prototypes were fabricated in 4 separate batches, of those produced 1 module was not used for further testing as post-processing damage incurred by the manufacturer prevented safe handling of the module glass. These prototypes are identified using the labelling system defined in Table 15.

Not all available PV cells were used to produce prototypes, several cells were excluded due to poor solder bonding, high cell curvature, cell fracture during soldering or edge chipping, this was done to assure that cell characterization analysis was not interfered with by suboptimal cell quality.

Code (BNN-G)	Range of Values	Description
Batch (B)	A to D	Manufacturing batches labelled in successive order, first batch A of size 2 was a trial run, B (4) was for prototypes to receive physical inspection, C (5) for annealed glass trial run and cell characterization testing, and D (6) for cell characterization.
Cell Number (NN)	1 to 25	PV cell number given to each of the PV cells prior to manufacture of the prototype, this was to allow easier coordination of testing data from individual PV cells to the completed prototypes containing said cells.
Glass Type (G)	A or T	Annealed or Tempered glass, annealed glass was only used for one batch (C) before it was deemed unsuitable to manufacture prototypes with the equipment available

Table 15: Prototype identification

ID#	Manufacturing Outcome	Purpose and Testing Use
A01-T	No major manufacturing defects or failures	Initial trial run, used for physical inspection
A02-T	No major manufacturing defects or failures	Initial trial run, used for physical inspection
B03-T	No major manufacturing defects or failures	Physical inspection
B04-T	Complete failure during post-processing stage,	Not used for further testing
B05-T	No major manufacturing defects or failures	Physical inspection
B06-T	No major manufacturing defects or failures	Physical inspection
B07-T	No major manufacturing defects or failures	Physical inspection
C11-A	Major manufacturing defect,	Initially intended for cell characterization, retained for further inspection of defects

C13-A	Major manufacturing defect	Initially intended for cell characterization, retained for further inspection of defects
C15-A	Major manufacturing defect	Initially intended for cell characterization, retained for further inspection of defects
C16-A	Major manufacturing defect	Initially intended for cell characterization, retained for further inspection of defects
D12-T	No major manufacturing defects or failures	Cell characterization testing
D14-T	No major manufacturing defects or failures	Cell characterization testing
D21-T	No major manufacturing defects or failures	Cell characterization testing
D22-T	No major manufacturing defects or failures	Cell characterization testing
D23-T	No major manufacturing defects or failures	Cell characterization testing
D24-T	No major manufacturing defects or failures	Cell characterization testing

Table 16: List of fabricated prototypes and manufacturing outcomes

7.2 Physical Inspection

Minimization of interfacial voids or gas bubbles in PV modules is critical for achieving suitable mechanical integrity, insulation, and moisture protection (H.-Y. Li et al., 2015). Detection of major bubbles or voids is conducted by visual inspection loosely following the criteria of MST 01 in IEC 61215-2:2018 (2018b). To complement this inspection a thickness uniformity test is used to determine the flatness deviation at the prototype corners, this is necessary as the presence of edge ‘pinch’ can significantly affect adhesion in glass-glass modules (Cattaneo et al., 2015; BSI, 2020b), edge compression was measured by taking a thickness measurement at corners, edge and a central region of the prototypes using a Micrometer.

ID#	Glass Type	Observed Defects
A01-T	Tempered	Single minor void at cell edge
A02-T	Tempered	Single minor void at cell edge
B03-T	Tempered	Single minor void at cell edge
B07-T	Tempered	Single minor void at cell edge
C11-A	Annealed	Multiple voids at cell edges and bus ribbon, fractured front and rear glass.
C13-A	Annealed	Multiple voids at cell edges and bus ribbon, fractured front and rear glass, minor disconnected cell area
C15-A	Annealed	Multiple voids at cell edges and bus ribbon, fractured front and rear glass.
C16-A	Annealed	Multiple voids at cell edges and bus ribbon, fractured front and rear glass, major disconnected cell area
D23-T	Tempered	Single minor void at cell edge
D24-T	Tempered	Single minor void at cell edge

Table 17: Fabricated prototype defects

Attempting to fabricate the smaller sized 175 x 175 mm² samples, (intended to be 155 x 175 mm² as designed in Figure 48 but not available due to manufacturer error), with annealed glass resulted in glass fracture during lamination (Figure 50), annealed glass has lower tensile strength and so was not able to withstand the pressure applied by the vacuum membrane during the process, the larger size prototypes withstood this pressure because they utilized tempered glass which has up to 4 times higher tensile strength. Furthermore the smaller dimensions could have had some effect on the failure also; during lamination with low viscosity encapsulants deflection occurs at the module edges and corners as a result of the encapsulant partially ‘squeezing out’ of the laminate as the vacuum membrane presses down on the edges of the top glass (Cattaneo et al., 2015), a similar amount of edge compression occurs in modules regardless of size as it is mostly dependent on encapsulant viscosity and membrane pressure, therefore in the smaller sized glasses the ratio of edge deflection to glass length is larger resulting in higher bending stresses and leading to the failures observed. Fractured glass

prevented an edge compression test taking place. Further fabrication procedures were undertaken with tempered glass only to prevent fracture during lamination.

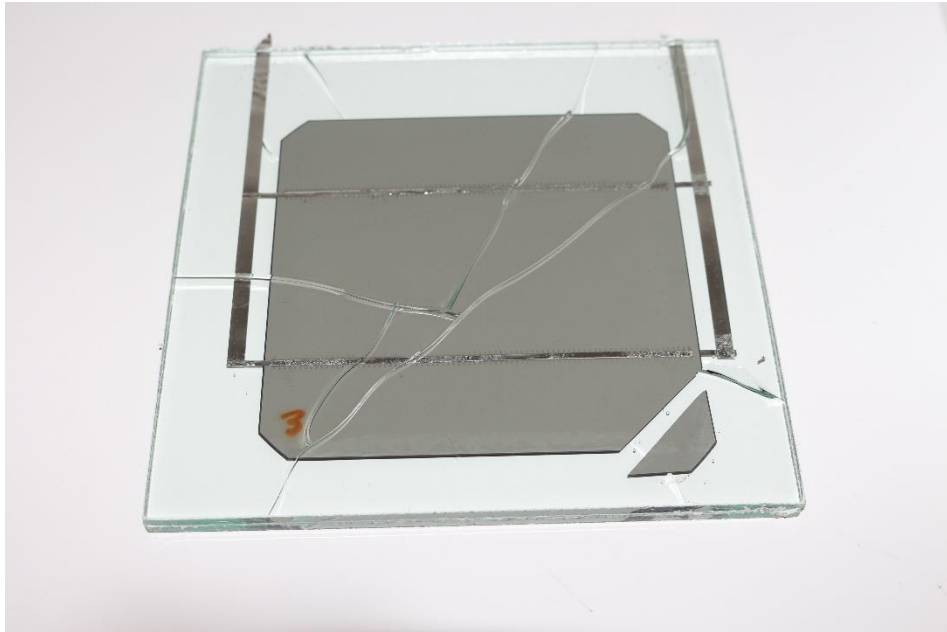


Figure 50: Defective annealed prototype with fractured glass and disconnected cell area

Tempered prototypes did not suffer from any major physical defects, although a single minor void like that in Figure 51 occurred in about half of the tempered prototypes. The void was about 1-2 mm in diameter and appeared to be embedded in the bulk of encapsulant, location of the voids was consistently on the cell edge opposite the interconnect terminals. These types of voids form as a result of entrapped air, water vapour, VOC formation, or contaminants in the lay-up and can be eliminated by effective vacuum application during the lamination process (H.-Y. Li et al., 2015). The consistent formation of voids near the cell edge indicates that air pockets entrapped between the encapsulant and cell during layup may be the culprit, the voids are likely not occurring on the other edges as the presence of the interconnects exiting the module side could provide the separation in the EVA to prevent air pockets forming.

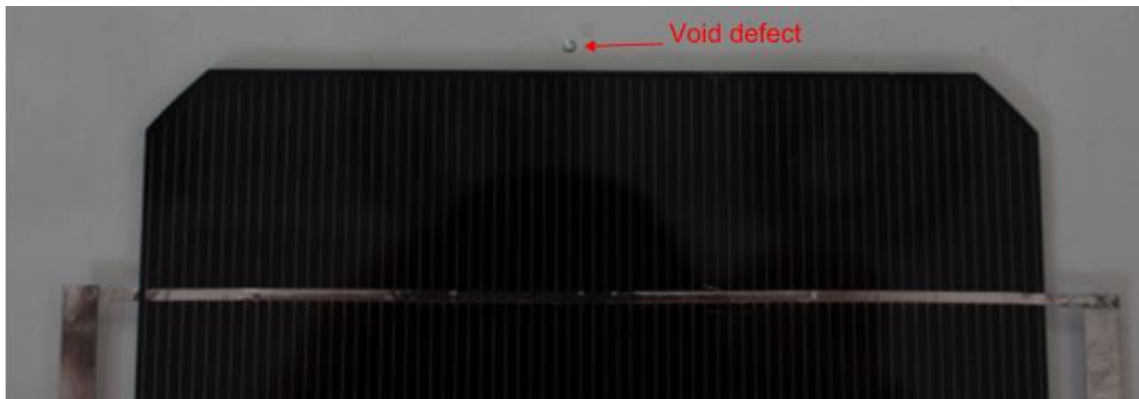


Figure 51: Prototype with minor void defect

A moderate amount of edge pinch was observed in almost all modules and was easily observed under visual inspection as can be seen in Figure 52. For glass-glass PV in a double chamber vacuum laminator about 1.0 mm of edge pinch is expected (Cattaneo et al., 2015), this was fairly consistent with the results observed, with the mean thickness difference between cell centre and module corners being 1.13 mm, the difference from cell to the centre of module edges was much lower at an average of 0.29 mm indicating that the majority of EVA squeeze out occurs at the corners.

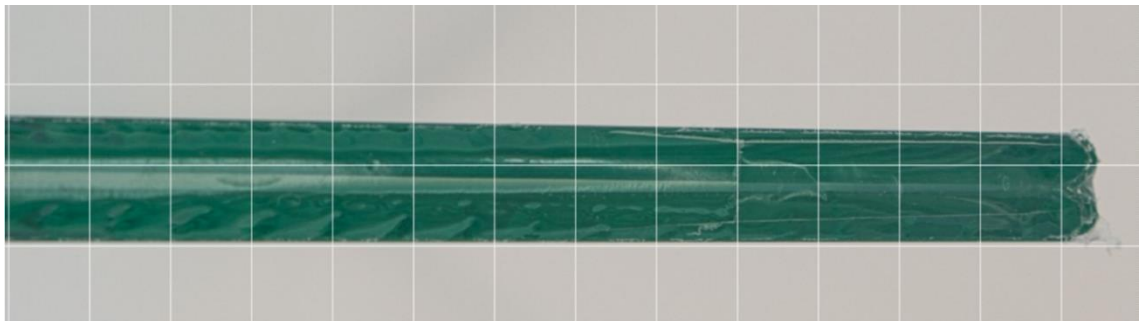


Figure 52: Prototype module showing edge pinch

The results presented below in Table 18 are the average thicknesses of the 4 corners (A), the thickness at the centre of the module edge between the terminals (B) and the measurement over a central cell region but not over the tabbing ribbon (C). Thickness deviations within ± 0.376 mm are expected to account for the industry standard tolerance for glass flatness of sheets below 6 mm (± 0.2 mm), expected thickness deviation due to roller wave in tempered glass (± 0.1 mm), and the manufacturer specified tolerance of $\pm 5\%$ for interlayer thickness (Pujol Group, 2020).

	A	B	C	Δd_{C-B}	Δd_{C-A}
B03-T	8.78	9.50	9.76	0.26	0.98
B05-T	8.60	9.44	9.82	0.38	1.22
B06-T	8.74	9.35	9.65	0.30	0.91
B07-T	8.74	9.55	9.73	0.18	0.99
D14-T	8.29	9.48	9.80	0.32	1.51
D21-T	8.63	9.45	9.74	0.29	1.11
D22-T	8.53	9.45	9.74	0.29	1.21
Mean	8.62 mm	9.46 mm	9.75 mm	− 0.29 mm	− 1.13 mm
Expected	--	9.52 ± 0.38 mm	9.72 ± 0.38 mm	--	About 1.00 mm

Table 18: Measured and expected prototype thicknesses

7.3 Cell Characterization

There are several methods of detecting mechanical damage in PV cells, most module turnkey lines use electroluminescent imaging (EL), which photographs UV emission of the cells under load to detect defective regions that are not generating current, these regions show up as dark areas in the EL image as seen in Figure 53. A similar approach to EL is using infrared thermal imaging (IRT) to detect regions of the module operating at higher temperatures due to resistive defects or reverse-bias operation. However IRT is particularly poor for glass-glass modules due to the opacity of glass in IR wavelengths causing low spatial resolution (Ahmad et al., 2019; Sinha et al., 2021), and EL requires expensive equipment and some level of expertise to perform correctly. Moreover both methods only provide a qualitative analysis and as such are mainly used for simple in-line or field detection of defects rather than analysis of the magnitude of such defects (Ahmad et al., 2019).

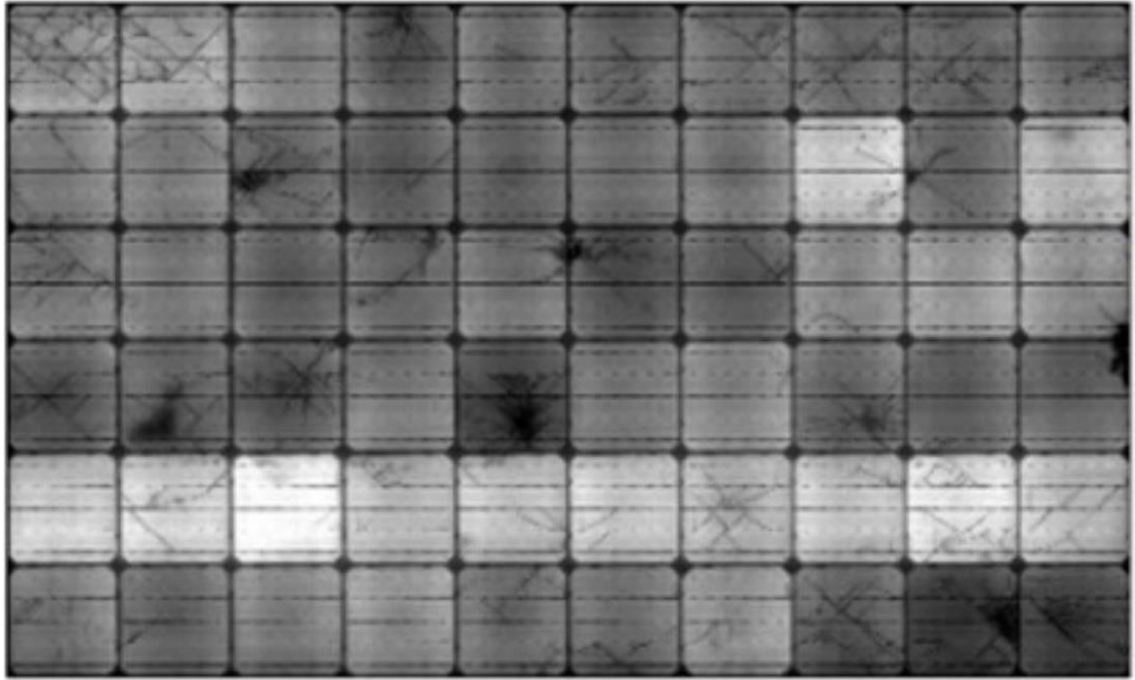


Figure 53: EL Image of a PV module showing cracks in multiple cells, dark regions indicate inactive areas (Sinha et al., 2021)

A more precise quantitative alternative is electrical characterization of cells through extraction of parameters from illuminated or dark current-voltage (I-V) curves, a high degree of accuracy can be achieved in determining key parameters, thereby allowing detection of very small changes that would not be possible using EL or IRT testing. I-V analysis is conducted by measuring the voltage across a cell or module terminals under different current loads, plotting the current and voltage pairs gives a characteristic curve which can be analysed to extract metrics of the PV devices performance. Illuminated I-V curves are measured by inducing current flow under artificial illumination using a solar simulator, or in natural outdoor lighting with the assistance of precise irradiance and temperature measurements and data correction algorithms (Köntges et al., 2014; Ahmad et al., 2019).

Alternatively dark I-V characterization can provide a suitable level of detail without the need for a solar simulator or precisely controlled outdoor measurement. Characteristics are measured without illumination by forcing current into the cell in reverse direction (+ to -), despite the current reversal the junction still operates under forward bias which allows for simple electrical characterization of the cell under a well-controlled environment (King et al., 1997). The lack of incoming light during characterization also means that optical losses resulting from adding laminate materials have no effect on the cell output, thereby allowing direct comparison of a cells condition before and after lamination (Spataru et al., 2015).

Parameters extracted from dark I-V curves also typically have a higher sensitivity to changes in the cell condition and can allow more accurate detection of smaller defects (King et al., 1997).

Analysis of silicon cells before and after mechanical damage by del Prado Santamaria et al. (2021) found that certain dark I-V parameters showed larger relative changes than those extracted from illuminated curves

7.3.1 Testing Methodology

To measure current and voltage the test device is connected in the circuit shown below in Figure 54, UNI-T UT803 RMS multimeters are used for measuring voltage and current, and EL302RD dual power supplies were used for the DC current source. To achieve near zero irradiance conditions the test unit is wrapped in a non-conductive cloth and placed under a shading device, additional shading is added to laminated prototypes to prevent light entering through the glass edges. The open circuit voltage of the cell is measured to be ≤ 0.1 mV prior to commencement of the test, this confirms that the light reaching the cell is negligible as the open circuit voltage is proportional to photo-generated current.

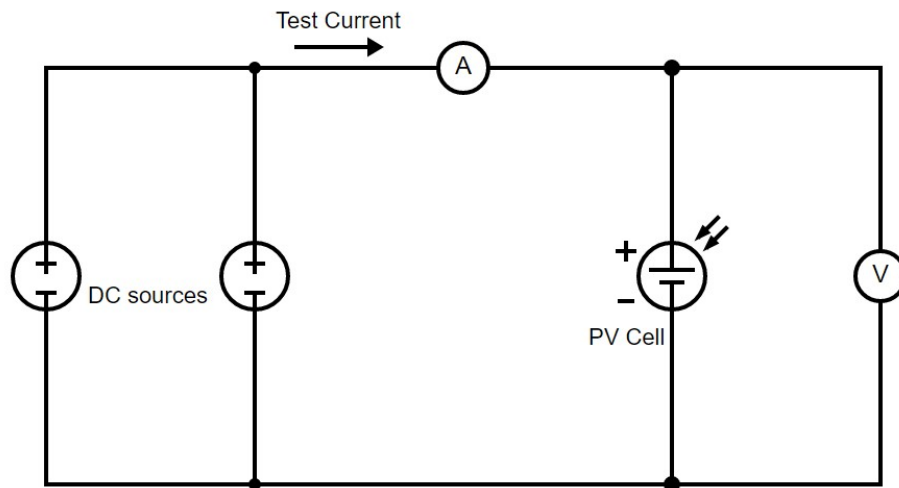


Figure 54: Dark I-V test circuit configuration

Voltage and current pairs are measured at predetermined intervals varying over the measurement range (between 1 – 20 mV), up to the maximum current of the power supply configuration (6.15 A), the value is selected to be higher than the short circuit current of the cell as this increases the accuracy of calculating the series resistance (Spataru et al., 2015), likewise at low current very small measurement intervals are used to improve the consistency in calculated shunt resistance (King et al., 1997). The I-V data is input to a MatLab program developed to perform the parameter extraction, and the cell characteristics before and after lamination can be compared to detect any electrical changes.

7.3.2 Double-Diode Model

The double-diode equivalent circuit is a standard tool for evaluating solar cell characteristics from I-V curves, Figure 55 below shows the equivalent PV circuit under dark conditions, under illumination an additional photogenerated current parallel and in the opposite direction to the diode currents reverses the overall direction of the cell current (I).

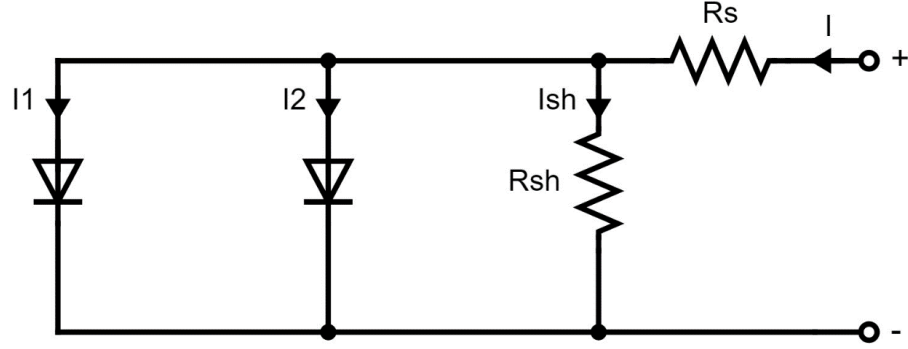


Figure 55: Double-diode equivalent circuit with no photo-generated current

The circuit above is described by the following expression (1), in which the values V and I are the voltage and current at the cell terminals, I_{01} and I_{02} are the diode saturation currents, n_1 and n_2 the diode ideality factors, R_s and R_{sh} the series and shunt (parallel) resistances of the cell, and V_{th} the thermal voltage which is a temperature dependent constant equal to 25.7 mV at room temperature (25 °C).

$$I = I_1 + I_2 + I_{sh} = I_{01} \left(e^{\frac{1}{n_1 V_{th}} (V - IR_s)} - 1 \right) + I_{02} \left(e^{\frac{1}{n_2 V_{th}} (V - IR_s)} - 1 \right) + \frac{V - IR_s}{R_{sh}} \quad (1)$$

$$I = I_{01} (e^{\alpha_1 V_j} - 1) + I_{02} (e^{\alpha_2 V_j} - 1) + \frac{V_j}{R_{sh}} \quad (2)$$

$$V_{th} = \frac{kT}{q} ; \quad V_j = V - IR_s ; \quad \alpha_x = \frac{1}{n_x V_{th}} \quad (3)$$

7.3.3 Algorithm

Extraction of parameters relies on fitting data to the double-exponential model in voltage regions where one or more components is negligible, which greatly reduces the complexity of the expression. The MatLab code created for this project utilizes existing methods in literature to find a fairly accurate initial value for each parameter, followed by region specific non-linear curve fitting to approach a suitably accurate final solution.

I-V data is difficult to fit to model as the expression for current ($I = f(V, I)$) is bivariate and self-dependent, to reduce the difficulty the series resistance is first calculated by analysing the high voltage regions where it dominates. For the solar cells used in this experiment it was shown that at high voltage $I \gg I_1 + I_{sh}$, therefore the total current can be approximated to the single-exponential expression for I_2 . The method of Kaminski et al. (1997) which is summarised below in equations (5) to (8) is used to solve the single exponential for R_s . The assumptions made generally holds true for voltages higher than 15 times the thermal voltage (V_{th}), which is about 0.4 V (Fuchs & Sigmund, 1986), hence this value is used as the lower bound to define the high voltage region, experimental analysis reinforces this assumption as the lowest residuals were obtained for a boundary voltage between 0.38 – 0.4 V for all cells.

$$I \approx I_2 = I_{02}(e^{\alpha_2(V - IR_s)}) \quad (4)$$

$$\ln I = \ln I_{02} + \alpha_2(V - IR_s) \quad (5)$$

$$\ln I - \ln I_0 = \ln I_{01} - \ln I_{01} + \alpha_1(V - IR_s) - \alpha_1(V_0 - I_0 R_s) \quad (6)$$

$$\frac{\ln\left(\frac{I}{I_0}\right)}{I - I_0} = -\alpha_2 R_s + \alpha_2 \frac{V - V_0}{I - I_0} \quad (7)$$

$$Y = \alpha_2(-R_{s0} + X) ; Y = \frac{\ln\left(\frac{I}{I_0}\right)}{I - I_0} ; X = \frac{V - V_0}{I - I_0} \quad (8)$$

To increase the number of datapoints for fitting, all possible pairs of (V , I) and (V_0 , I_0) are taken from the high voltage dataset as is also done by Kaminski et al. (1997), this gives $n(n-1)/2$ values of (X , Y) for N pairs of data (V, I) which greatly improves the strength of the fit as seen in the example regression fit in Figure 56.

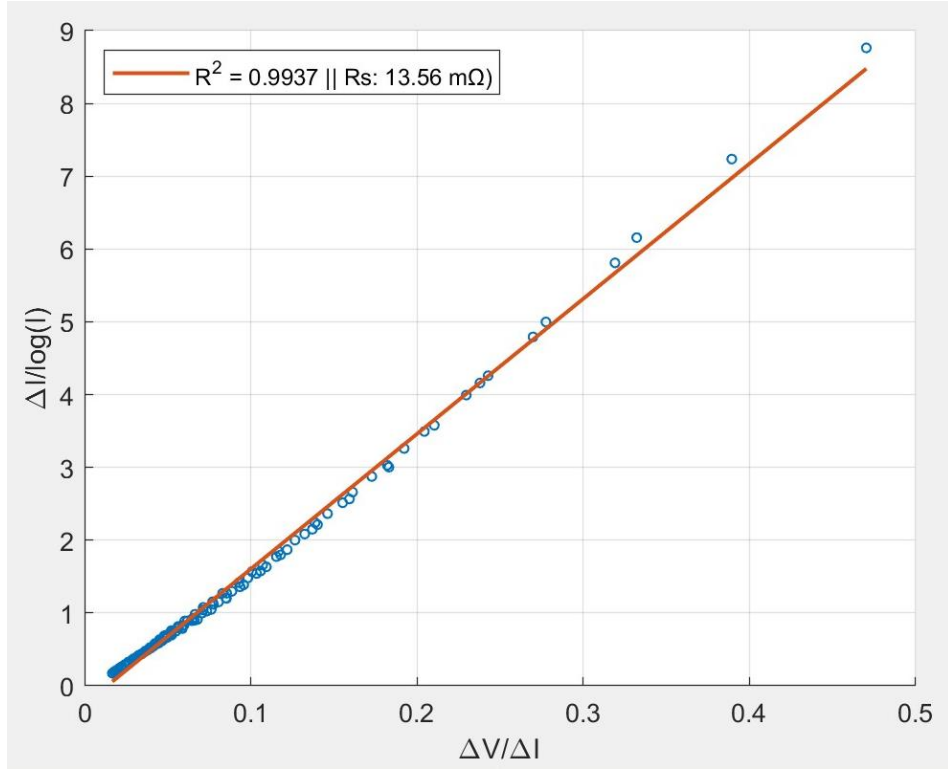


Figure 56: Regression line for equation 8 using all possible combinations of data pairs to obtain a strong fit

The shunt resistance is then initially estimated from very-low voltages, where the first diode current is essentially negligible as the exponential tends towards zero and I_1 is much smaller than I , likewise the voltage drop across the series resistor can be treated as zero and the junction voltage approximated as the total cell voltage. The saturation current I_{02} is initialized by linear regression of equation (9) in the high voltage region and then input into equation (11) long with the previously calculated α_2 to find a fairly accurate initial estimate for shunt resistance, it is important that the voltage current pairs are taken sufficiently close to zero to ensure that the assumptions permitting this method remain true, for this analysis voltages less than 30 mV were deemed suitable as a strong linear relation was observed below this value (See Figure 57).

$$\ln I \approx \alpha_2(V - IR_s) + \ln I_{02} \quad (V > 0.4) \quad (9)$$

$$I \approx I_{02}(e^{\alpha_2 V} - 1) + \frac{V}{R_{sh}} \quad (10)$$

$$R_{sh0} \approx \frac{V}{I - I_{02}(e^{\alpha_2 V} - 1)} \quad (\text{For low voltages}) \quad (11)$$

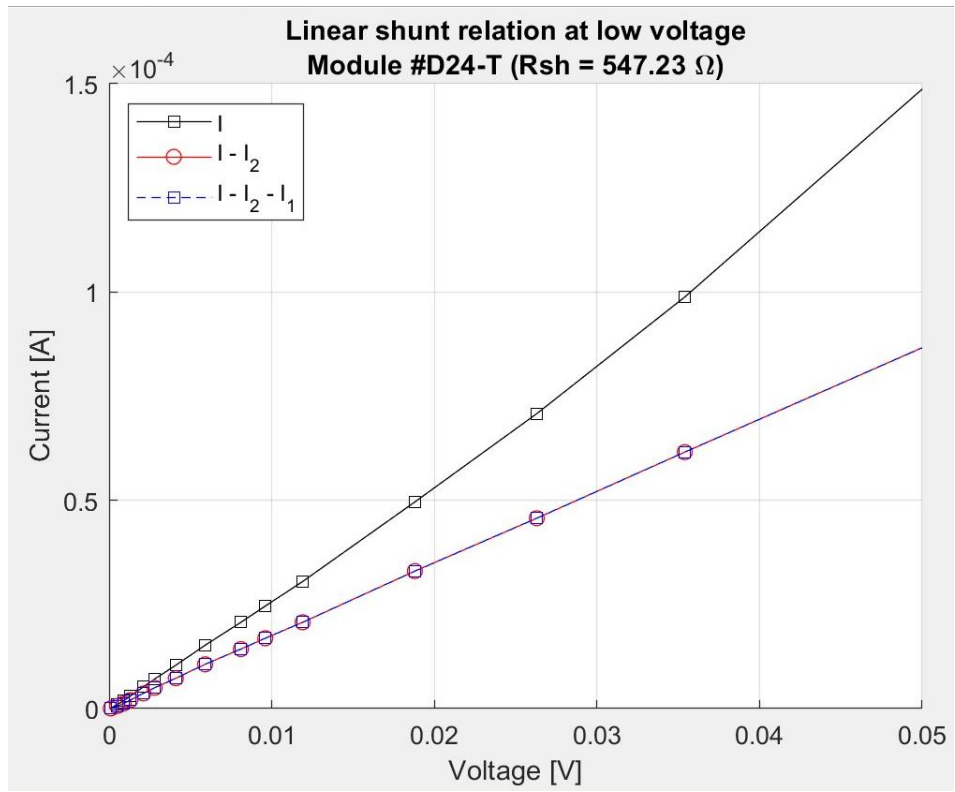


Figure 57: Shunt region showing linear relation of approximate shunt current ($I - I_2$) at low voltage, note that ignoring I_1 has negligible effect

Once R_s is approximated the current (I) can be reduced to a function of junction voltage only $f(V_j)$, which allows for non-linear curve fitting to data pairs of V_j and I . The values previously estimated for R_{sh} , α_2 , and I_{02} are used as starting points, while the 2 remaining unknown parameters I_{01} and α_1 are approximated to $1e-10$ and $1/V_{th}$ respectively which are values obtained from dark I-V results in existing literature (King et al., 1997; del Prado Santamaria et al., 2021). A curve fitting process is then conducted in which the curve is partially fit in low and high voltage regions using equations (11) to (12), following by fitting over the entire range with (12) as shown by the example in Figure 58. The resulting values are updated at each stage and carried over as initial estimates for the following fit. If sufficiently low residuals are not reached the process can be iterated by gradually altering values of R_s to find an optimal solution.

$$I = I_{02}(e^{\alpha_2 V_j} - 1) + \frac{V_j}{R_{sh}} \quad (V < 0.1 V) \quad (11)$$

$$I = I_{02}(e^{\alpha_2 V_j} - 1) + I_{01}(e^{\alpha_1 V_j} - 1) + \frac{V_j}{R_{sh}} \quad (12)$$

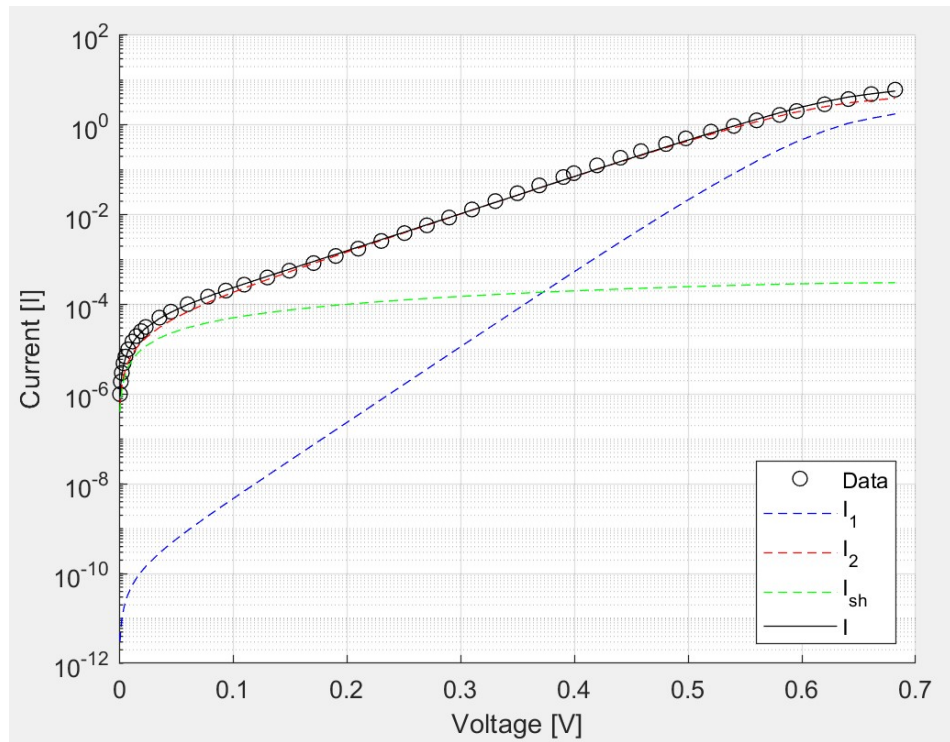


Figure 58: Fitted curve for prototype D14-T pre-lamination

7.3.4 Results

After lamination all PV cells had increased current observed in both the low and medium voltage regions, which correlates to an increase in shunt and junction recombination losses (Spataru et al., 2015). A decrease in shunt resistance raises the gradient in the low voltages (<0.1 V), while an increased saturation current in diode 2 raises the current in medium voltages (0.1 to 0.4 V). At medium-high voltages there was very small difference due to the low magnitude of I_{01} , while a slight decrease in current near the maximum voltage indicates that series resistance increased slightly for some cells. All these graphical observations correlate well with the actual parameters extracted by MatLab code. Figure 59 below shows an example of the graphical difference in dark I-V curves for a prototype that exhibited particularly high junction-recombination losses. Complete results for curve fitting can be found in Appendix C.

Parameter	D12-T	D14-T	D21-T	D22-T	D23-T	D24-T
Initial R_s	14.85 m Ω	14.20 m Ω	12.11 m Ω	12.39 m Ω	11.93 m Ω	12.28 m Ω
Final R_s	13.54 m Ω	13.18 m Ω	--	13.43 m Ω	13.76 m Ω	13.64 m Ω
ΔR_s	-8.83 %	-7.16 %	--	+8.34 %	15.34 %	11.10 %
Initial R_{sh}	5006.0 Ω	3010.6 Ω	4928.6 Ω	8431.2 Ω	2285.3 Ω	1680.4 Ω
Final R_{sh}	627.2 Ω	285.8 Ω	540.9 Ω	404.9 Ω	466.0 Ω	618.1 Ω
ΔR_{sh}	-87.47 %	-90.51 %	-89.02 %	-95.20 %	-79.61 %	-63.22 %
Initial I_{02}	7.42 x 10 ⁻⁶	1.31 x 10 ⁻⁵	2.09 x 10 ⁻⁵	3.29 x 10 ⁻⁵	3.66 x 10 ⁻⁵	2.99 x 10 ⁻⁵
Final I_{02}	2.88 x 10 ⁻⁵	4.30 x 10 ⁻⁵	--	5.65 x 10 ⁻⁵	4.35 x 10 ⁻⁵	4.41 x 10 ⁻⁵
ΔI_{02}	+288.0 %	+228.4 %	--	+71.55 %	+18.65 %	+47.32 %

Table 19: Electrical parameters before and after lamination

The extracted values are all well within reason for a crystalline PV cell, although the values of shunt resistance seem quite high it must be considered that shunt resistance increases as illumination drops (Mavromatakis et al., 2017), the high deviation in initial shunt resistances is expected to be a result of poor cell quality and some random degree of damage occurring due to mechanical force applied during soldering.

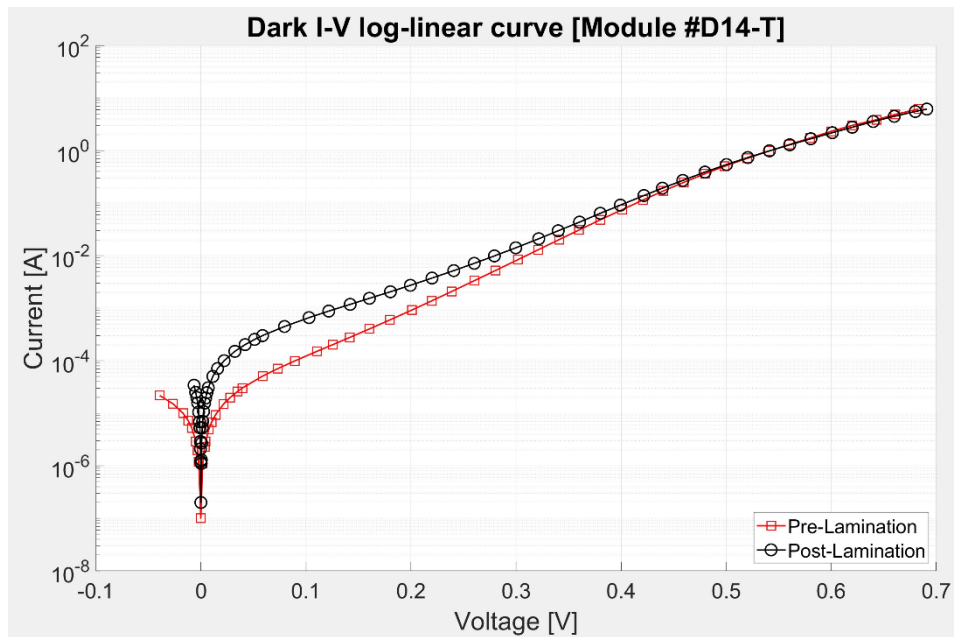


Figure 59: Dark I-V curve before and after lamination

7.3.5 Discussion

Shunt resistance decrease represents the formation of shunt paths, which are high conductance paths across the cell junction or on the cell edges, these paths lead current away from the intended path, lowering the performance of the cell and are usually caused by cracks in the cell (Köntges et al., 2014; Ahmad et al., 2019). Changes in the second diode parameters (I_{02} , n_2) are also associated with cell cracking caused by junction-recombination losses in the p-n junction (Spataru et al., 2015). While an increase in series resistance is usually due to circuitry damage such interconnect ribbon damage or disconnection but can also increase due to cell damage (Köntges et al., 2014; Ahmad et al., 2019).

The results in Table 20 below strongly suggest that primarily mechanical cell damage occurred, as degradation of the cell circuit would cause solely series resistive losses, whereas mechanical cell damage causes additional shunt and junction recombination losses which are observed (Spataru et al., 2015).

	R_s	R_{sh}	I_{02}	n_2
Pre-lamination average	12.96 mΩ	4223.7 Ω	2.35×10^{-5}	1.943
Post-lamination average	13.51 mΩ	490.5 Ω	4.32×10^{-5}	2.058
Average change	+3.76 %	-84.17 %	+130.77 %	+6.82 %

Table 20: Average change in electrical parameters after lamination

The changes in series resistance are not large enough to confidently state that they were caused by physical change in cell condition, some cells exhibited negative change of up to -10% when it is not reasonable that the resistance should actually decrease, therefore the calculation of series resistance may have an error of at least $\pm 10\%$. It can be assumed that the small series resistance changes observed is more likely due to inaccuracies in fitting rather than mechanical damage, even so the small magnitude of change would be expected as the work of Zhang et al. (2022) found that cracked cells showed very little change in series resistance while shunt resistance decreases markedly.

The magnitude of change in shunt resistance and saturation current are indicative of a significant amount of mechanical cell damage occurring, studies on PV cells with moderate amount of cracks and disconnected areas exhibited similar changes in R_{sh} and I_{02} (del Prado Santamaria et al., 2021).

There are 3 proposed causes for the mechanical damage to the cells during prototype fabrication, first would be damage incurred during transport, handling and layup process, second is damage incurred from thermal residual stress resulting during lamination and/or soldering cooldown, and third is stresses arising from mechanical pressure applied during lamination.

The uniformity of decrease in shunt resistance would indicate that damage occurring during handling is unlikely, as cracks arising from this would be expected to occur randomly and in a small portion of cells, leading to a high deviation between changes in shunt resistance before and after lamination, however the observed changes had reasonable uniformity ($M = 84.17$, $SD = 10.46$), albeit from a very small sample, indicating a consistent source of mechanical stress.

The process temperatures and materials used here are so similar to conventional PV manufacturing that cell damage as a result of thermal contraction is unexpected, but it cannot be completely ruled out. The design and manufacturing process incorporates a number of features that have been proven to significantly reduce the maximum principal stresses arising from thermal contraction, including thinner tab ribbon (0.15 mm), thicker cells (200 μm), lower cure temperatures (135 $^{\circ}\text{C}$), wider busbars (1.8 mm), thicker encapsulants (1.52 mm) and maintained membrane pressure during cooldown phase (Dietrich et al., 2010; Rowell et al., 2018; Shin et al., 2018; Song et al., 2018). All of these features are capable of working in conjunction to lower the risk of thermal contraction damage during lamination.

One design factor that could have increased the risk of cell damage from thermal contraction is the use of a higher temperature solder, as the 96.5Sn3.5Ag solder coating would raise cell stresses during soldering due to the higher solder melt temperature (217 $^{\circ}\text{C}$) compared to alternative bismuth-tin or lead-tin solders (Shin et al., 2018). However since cells are characterized after soldering this would only have an impact if the residual thermal effects from soldering increase the likelihood of breakage once the cell is laminated, simulation of vacuum lamination by Shin et al. (2018) found that the residual stresses induced during soldering are actually expected to decrease during lamination due to elastic strain recovery of the silicon wafer.

The most probable cause for mechanical damage during lamination is stress induced by mechanical pressure of the vacuum membrane. The time at which external pressure application begins is different in the VBO process for conventional glass lamination than it is for double-chamber PV lamination. Double-chamber PV laminators separate the function of vacuum extraction and applying external pressure to the module, meaning that the pressure can be applied at a later point in the lamination cycle when the encapsulant is softer without compromising the effectiveness of removing air (See Figure 60). On the other hand the vacuum

bag only process used in EVA glass lamination only has a single chamber (the vacuum bag) meaning continuous application of external pressure occurs whenever the vacuum is active, hence external pressure must be applied earlier in the cycle to properly evacuate air, leading to higher mechanical loads being transferred to the PV cells through the stiffer encapsulant which has not as much time to warm up and soften.

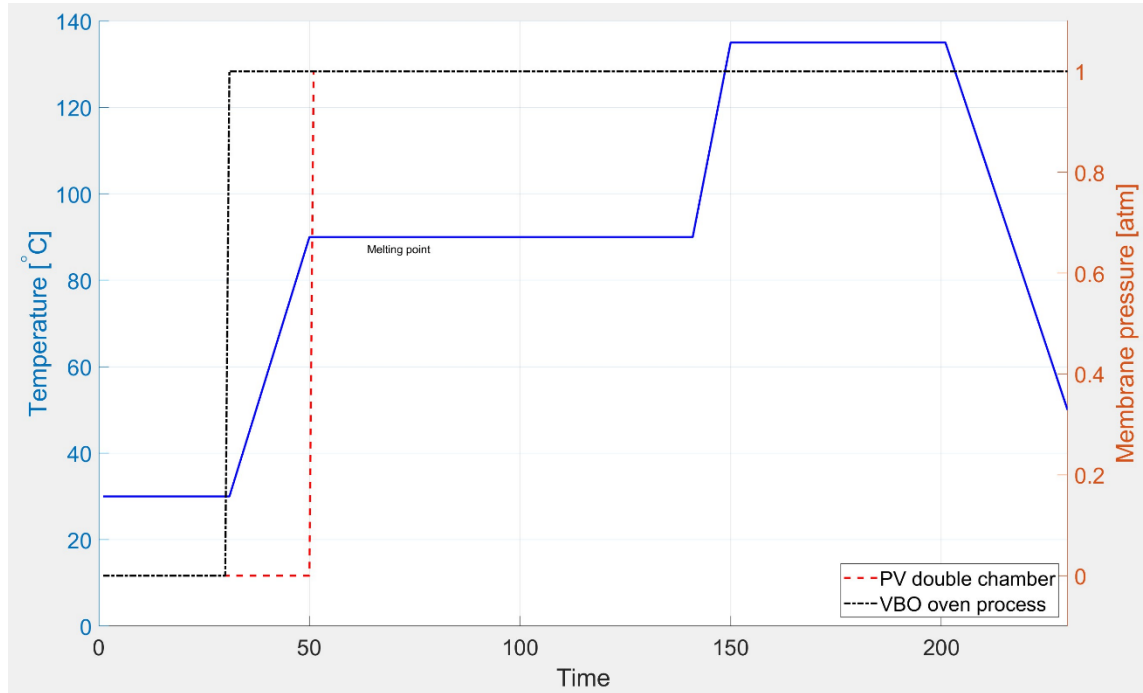


Figure 60: Difference in pressure application between VBO single and double-chamber lamination

This departure from the industry standards for PV lamination equipment could provide an explanation as to why significant cell damage occurred in fabricated prototypes despite the similarities in design and processing temperatures to a typical glass-glass PV module. Existing literature supports this theory, most notably the work of Song et al. (2018) who simulated stresses occurring in PV lamination when membrane pressure is applied before the EVA reaches its softening point of 70 °C. They found that before the EVA sheets melt they are not in contact with the cell on either side of the interconnect (Figure 61) and cause the cell to bend over the front interconnect as pressure is transmitted through the solid EVA film, once the laminate reaches the melt temperature the EVA exerts a uniform hydrostatic pressure of 1 atm on the surfaces of the cell and interconnects and the stress concentrations decrease significantly. The maximum principal stress which occurs in the cell can be over 10 times higher prior to melting of the encapsulant. This seems likely to be the cause of cell damage as the high stress concentrations induced by the solid EVA bending the cells can easily exceed the fracture strength of silicon PV cells (Song et al., 2018).

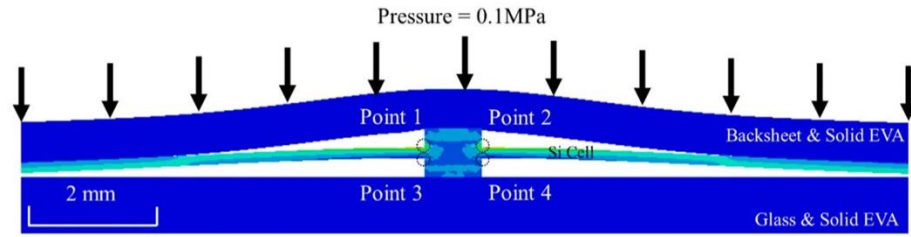


Figure 61: Stress concentration in PV cells during lamination (Song et al., 2018)

Maximum stress concentration are endured along the intersection between the busbar and the cell surface (Song et al., 2018), this would likely result in cracks running parallel to the busbar (along this concentration line) or spreading out from the busbar at particularly concentration points. Parallel crack formation is the most critical for power loss, Kajari-Schroder et al. (2015) observed that parallel cracks have a much higher probability of causing degraded or separated cell areas than perpendicular or diagonal cracks. This is partially because parallel cracks directly dissect the current carrying metallization fingers, resulting in a larger cell area becoming electrically disconnected. The formation of these critical parallel cracks resulting from the location of maximum stresses could explain why such a large change in electrical parameters was observed.

7.3.6 Proposed Changes to Methodology

Accurately fitting the very upper voltages of the curves proved to be very difficult and the value extracted for series resistance was highly sensitive to small changes in the fitting process while also exhibiting possible errors of at least 10% making it difficult to confidently determine small changes in R_s .

The accuracy of extracting R_s is partly limited by the algorithm used, for initial estimates the assumptions made to arrive at equation (7) require that $I_2 \gg I_1$ at high voltages which holds true for the specific undamaged cells used in this work, however after lamination the value of I_1 could reach up to 20% of I_2 at high voltages, which could lead to larger deviations in initial estimates from the actual value. Errors in the initial estimate of R_s are quite significant for the algorithm as it is not recalculated during curve fitting due to the self-dependency of the expression, and all subsequently fit parameters are dependent on the initial estimate.

To further complicate the uncertainties resulting from this method it seems that the assumptions made in developing a double-diode model do not always accurately apply to a solar cell that is damaged, del Prado Santamaria (2021) found that double-diode fitting of cracked cells had certain limitations and would sometimes yield inaccurate results due to over-fitting of certain parameters in order to fit the shape of the data curve. This is because as a cell becomes damaged the assumptions of series resistance being homogeneously distributed begin to break down,

localized resistive defects cause non-uniformly distributed degradation which results in poor curve fitting, especially for series resistance (Suckow, 2014; del Prado Santamaria et al., 2021)

The significance of the uncertainties in series resistance on the experimental results obtained during this research are small as purely mechanical cell damage primarily results in shunt and junction-recombination losses, and so series resistance was not of great importance in detecting cell cracking, also while mentioned above that the double-diode model may not apply to damaged cells it did not appear to affect this particular analysis as a comparable residual error was obtained before and after damage was incurred. Future improvements to the accuracy would still be useful to increase the versatility of the algorithm in detecting smaller series resistance changes and remaining accurate for cells with more localized defects.

The parameter extraction algorithm could be expanded to fit to a more complex equivalent circuit model that is better suited for fitting data from damaged PV cells, both the distributed series resistance and resistance limited recombination models described by Suckow (2014) are capable of fitting data for cells with non-homogenous defects and would provide a good basis for a versatile method. In addition to this using equipment with a better high current accuracy and smaller measurement intervals and lower data variance could further improve the accuracy of extracted parameters.

8 Conclusions

This research has shown that the effect of the lamination processes on PV cells can be measured using low-cost dark I-V testing, allowing for optimization of the process to minimize mechanical damage to PV cells.

Crystalline silicon solar cells are susceptible to cracks, generally not visible to the naked eye, whose propagation can remove a portion of the cells area from the electrical circuit. Lamination of glass-glass PV modules in a single chamber vacuum bag only process appears to be more likely to induce cell cracking than a conventional PV double-chamber laminator, which is proposed to be a result of higher forces being transferred through the encapsulant material into the cells

It appears that introducing membrane pressure at a later stage in the heating cycle, once the encapsulant is almost melted, may prevent the mechanical damage, however this delaying of the vacuum stage must be done so in a way that gas is not trapped within the module.

8.1 Future Work

Future work could be conducted to investigate the effects of altering the time in the process at which the vacuum is applied to determine if later application when the encapsulant is heated reduces the magnitude of shunt defects observed.

The design of prototypes should also be modified to better isolate the cause of mechanical damage during the fabrication procedure, to achieve this a conductive adhesive could be used to adhere the tabbing ribbon to the solder cell which would completely remove the tab soldering process and its resulting residual stress.

References

- Abergel, T., Delmastro, C., Monschauer, Y., Lane, K., & Opperman, M. (2021, November). *Tracking buildings 2021*. International Energy Agency
<https://www.iea.org/reports/tracking-buildings-2021>
- Advanced Solar Power. (2020, July 23). *ASP-STI*. Retrieved August 22, 2021, from
<https://cdn.enfsolar.com/Product/pdf/Crystalline/5f8939be9d873.pdf>
- Ahmad, J., Ciocia, A., Fichera, S., Murtaza, A. F., & Spertino, F. (2019). Detection of typical defects in silicon photovoltaic modules and application for plants with distributed MPPT configuration. *Energies*, 12(23), Article 4547.
<https://doi.org/10.3390/en12234547>
- Ahsan, S. M. & Khan, H. A. (2019). Performance comparison of CdTe thin film modules with c-Si modules under low irradiance. *IET Renewable Power Generation*, 13(11), 1920–1926. <https://doi.org/10.1049/iet-rpg.2018.5479>
- Aleo Solar. (2020, February 18). *Elegante 200W*. Retrieved September 3, 2021, from
https://www.aleo-solar.com/app/uploads/2016/01/GG_Elegante_200W_5BB_EN_web-2.pdf
- Almaden Morocco. (2021, January 5). *SEAC40T: Dual glass module / Perc monocrystalline cells*. Retrieved September 13, 2021, from
<https://www.almaden.ma/products/#1565818162610-d5ad3238-406e>
- Almora, O., Baran, D., Bazan, G. C., Berger, C., Cabrera, C. I., Catchpole, K. R., Erten-Ela, S., Guo, F., Hauch, J., Ho-Baille, A. W. Y., Jacobsson, T. J., Janssen, R. A. J., Kirchartz, T., Kopidakis, N., Li, Y., Loi, M. A., Lunt, R. R., Mathew, X., McGehee, M. D., ...Brabec, C. J. (2020). Device performance of emerging photovoltaic materials (Version 1). *Advanced Energy Materials*, 11(11), Article 2002774.
<https://doi.org/10.1002/aenm.202002774>
- Antec Solar. (2014). *BIPV - Downloads*. Retrieved August 16, 2021, from <https://www.antec-solar.de/bipv-en-us/downloads-en-us/>
- Ballif, C., Perret-Aebi, L.-E., Lufkin, S., & Rey, E. (2018). Integrated thinking for photovoltaics in buildings. *Nature Energy*, 3(6), 438–442. <https://doi.org/10.1038/s41560-018-0176-2>

- Baoding Jiasheng Photovoltaic Technology. (2021, January 19). *Green building materials*. Retrieved March 8, 2022, from <http://www.gainsolar.cn/en/product/index.html>
- Başol, B. M., & McCandless, B. (2014). Brief review of cadmium telluride-based photovoltaic technologies. *Journal of Photonics for Energy*, 4(1), Article 040996. <https://doi.org/10.1117/1.JPE.4.040996>
- Bisol Group. (2021, April 20). *BISOL Lumina: High-transparency monocrystalline PV modules*. Retrieved September 3, 2021, from <https://www.bisol.com/premium>
- Booth, H. (2010). Laser processing in industrial solar module manufacturing. *Journal of Laser Micro/Nanoengineering*, 5(3), 183–191. <https://doi.org/10.2961/jlmn.2010.03.0001>
- Borgers, T., Govaerts, J., Voroshazi, E., Jambaldinni, S., O’Sullivan, B., Singh, S., Debucquoy, M., Szlufcik, J., & Poortmans, J. (2017). A woven fabric for interconnecting back-contact solar cells. *Progress in Photovoltaics: Research and Applications*, 25(7), 569–582. <https://doi.org/10.1002/pip.2851>
- Bornemann, S. (2019, June 26–28). *Controlling lamination result of EVA laminating films for several lamination processes* [Poster presentation]. Glass Performance Days 2019, Tampere, Finland. https://www.youtube.com/watch?v=prNH09KoG-w&ab_channel=GPDGlassPerformanceDays
- Brecl, K., Topič, M., & Smole, F. (2005). A detailed study of monolithic contacts and electrical losses in a large-area thin-film module. *Progress in Photovoltaics: Research and Applications*, 13(4), 297–310. <https://doi.org/10.1002/pip.589>
- British Standards Institution. (2018a). *Photovoltaic (PV) module safety qualification - Part 1: Requirements for construction* (BS EN IEC 61730-1:2018). <https://bsol.bsigroup.com/>
- British Standards Institution. (2018b). *Photovoltaic (PV) module safety qualification - Part 2: Requirements for testing* (BS EN IEC 61730-2:2018). <https://bsol.bsigroup.com/>
- British Standards Institution. (2018c). *Photovoltaic (PV) modules - Type approval, design and safety qualification - Retesting* (PD IEC/TS 62915:2018). <https://bsol.bsigroup.com>
- British Standards Institution. (2020b). *Measurement procedures for materials used in photovoltaic modules - Part 5-2: Edge seals - Durability evaluation guideline* (PD IEC TS 62788-5-2:2020). <https://bsol.bsigroup.com>
- British Standards Institution. (2021a). *Terrestrial photovoltaic (PV) modules - Design qualification and type approval - Part 1: Test requirements* (BS EN IEC 61215-1:2021). <https://bsol.bsigroup.com>

- British Standards Institution. (2021b). *Terrestrial photovoltaic (PV) modules - Design qualification and type approval - Part 2: Test procedures* (BS EN IEC 61215-2:2021). <https://bsol.bsigroup.com>
- Callister, W. D., & Rethwisch, D. G. (2018). *Materials science and engineering: An introduction* (10th ed.). John Wiley & Sons.
- Carrot, C., Bendaoud, A., & Pillon, C. (2015). Polyvinyl butyral. In O. Olagoke & A. Kolapo (Eds.), *Handbook of thermoplastics* (pp. 107–156). CRC Press. <https://doi.org/10.1201/b19190-4>
- Cattaneo, G., Faes, A., Li, H.-Y., Galliano, F., Gragert, M., Yao, Y., Grischke, R., Söderstrom, T., Despiessse, M., Ballif, C., & Perret-Aebi, L.-E. (2015). Lamination process and encapsulation materials for glass–glass PV module design. *Photovoltaics International*, 27, 1–8. https://www.researchgate.net/publication/273444004_Lamination_process_and_encapsulation_materials_for_glass-glass_PV_module_design
- Chen, B.-M., Peng, C.-Y., Cho, J.-L., & Porter, G. A. (2015). Optimization of Solar Module Encapsulant Lamination by Optical Constant Determination of Ethylene-Vinyl Acetate. *International Journal of Photoenergy*, 2015, 1–7. <https://doi.org/10.1155/2015/276404>
- Corti, P., Bonomo, P., Frontini, F., Macé, P., & Bosch, E. (2020). *Building integrated photovoltaics: A practical handbook for solar buildings' stakeholders: Status report 2020*. SUPSI - Becquerel Institute. https://solarchitecture.ch/wp-content/uploads/2020/11/201022_BIPV_web_V01.pdf
- CS Wismar. (2020). *Brilliant*. Sonnenstromfabrik. Retrieved August 17, 2021, from <https://www.sonnenstromfabrik.com/en/products/brilliant/>
- de Oliveira, M. C. C., Diniz, A. S. A. C., Viana, M. M., & Lins, V. D. F. C. (2018). The causes and effects of degradation of encapsulant ethylene vinyl acetate copolymer (EVA) in crystalline silicon photovoltaic modules: A review. *Renewable and Sustainable Energy Reviews*, 81, 2299–2317. <https://doi.org/10.1016/j.rser.2017.06.039>
- del Prado Santamaria, R., Dos Reis Benatto, G. A., Lancia, A. A. S., Garaj, M., Thorsteinsson, S., Poulsen, P. B., & Spataru, S. V. (2021). Characterization of electrical parameters of cracked crystalline silicon solar cells in photovoltaic modules. *2021 IEEE 48th Photovoltaic Specialists Conference (PVSC)*, 846–853. <https://doi.org/10.1109/PVSC43889.2021.9519081>

- Detollenaere, A., Masson, G., Kaizuka, I., Jäger-Waldau, A., & Donoso, J. (2021, April 27). *Snapshot of global PV markets 2021*. (Report No. IEA-PVPS T1-39:2021). International Energy Agency - Photovoltaic Power Systems Programme. https://iea-pvps.org/wp-content/uploads/2021/04/IEA_PVPS_Snapshot_2021-V3.pdf
- Dietrich, S., Pander, M., Sander, M., Schulze, S. H., & Ebert, M. (2010). Mechanical and thermomechanical assessment of encapsulated solar cells by finite-element-simulation. In *Reliability of photovoltaic cells, modules, components, and systems III* (Vol. 7773, p. 77730F). International Society for Optics and Photonics. <https://doi.org/10.1117/12.860661>
- Drabczyk, K., & Panek, P. (2012). A comparative study of EVA with and without thermal history for different lamination process parameters. *Materials Science and Engineering: B*, 177(15), 1378–1383. <https://doi.org/10.1016/j.mseb.2012.04.009>
- ENF Solar. (n.d.). *Solar panel manufacturers*. Retrieved June 9, 2021, from <https://www.enfsolar.com/directory/panel>
- Ertex Solartechnik. (n.d.). *Semi-transparent modules*. Ertex Solar. Retrieved October 17, 2021, from <https://www.ertex-solar.at/en/products/semi-transparent-modules/>
- Feldman, D., Wu, K., & Margolis, R. (2021, July 12). *H1 2021 solar industry update* (Report No. NREL/PR-7A40-80427). National Renewable Energy Laboratory. <https://www.nrel.gov/docs/fy21osti/80427.pdf>
- Folienwerk Wolfen. (2014). *Handling guide - evguard® laminating film*. <https://difsk.sk/wp-content/uploads/2017/11/Handling-Guide-evguard.pdf>
- Fthenakis, V., & Zweibel, K. (2003). *CdTe PV: Real and perceived EHS risks* (Report No. NREL/CP-520-33561). National Renewable Energy Lab. <https://doi.org/10.2172/1808491>
- Fuchs, D., & Sigmund, H. (1986). Analysis of the current-voltage characteristic of solar cells. *Solid-State Electronics*, 29(8), 791–795. [https://doi.org/10.1016/0038-1101\(86\)90181-4](https://doi.org/10.1016/0038-1101(86)90181-4)
- G.James Glass & Aluminium. (2007). *G.James glass handbook*. Retrieved October 10, 2021, from https://professional.gjames.com/__data/assets/pdf_file/0004/134923/gjames_glass_handbook.pdf
- Gečys, P., Markauskas, E., Nishiwaki, S., Buecheler, S., De Loor, R., Burn, A., Romano, V., & Račiukaitis, G. (2017). CIGS thin-film solar module processing: case of high-speed laser scribing. *Scientific Reports*, 7, Article 40502. <https://doi.org/10.1038/srep40502>

- Ghosh, A. (2020). Potential of building integrated and attached/applied photovoltaic (BIPV/BAPV) for adaptive less energy-hungry building's skin: A comprehensive review. *Journal of Cleaner Production*, 276, Article 123343. <https://doi.org/10.1016/j.jclepro.2020.123343>
- Global Industry Analysts. (2021). *Building integrated photovoltaics (BIPV): Global market trajectory and analytics*. <https://www.strategyr.com/market-report-building-integrated-photovoltaics-bipv-forecasts-global-industry-analysts-inc.asp#sthash.fE17VTUo.dpbs>
- Grand View Research. (2021, February). *Building-integrated photovoltaics market report, 2021-2028* (Report No. GVR-1-68038-301-0). <https://www.grandviewresearch.com/industry-analysis/building-integrated-photovoltaics-bipv-market>
- Green, M. A., Dunlop, E. D., Hohl-Ebinger, J., Yoshita, M., Kopidakis, N., & Hao, X. (2021). Solar cell efficiency tables (Version 58). *Progress in photovoltaics: Research and Applications*, 29(7), 657–667. <https://doi.org/10.1002/pip.3444>
- Li, H.-Y., Luo, Y., Ballif, C., & Perret-Aebi, L.-E. (2015). Modeling of voids evolution in the encapsulation process of photovoltaic modules. *Polymers & Polymer Composites*, 23(6), 375–388. <https://doi.org/10.1177/096739111502300603>
- International Electrotechnical Commission. (2020). *Photovoltaics in buildings - Part 1: Requirements for building-integrated photovoltaic modules* (IEC 63092-1:2020). <https://www.standards.govt.nz/>
- International Energy Agency. (2021, September). *Key world energy statistics 2021*. <https://www.iea.org/reports/key-world-energy-statistics-2021>
- Jilani, A., Abdel-wahab, M. S., & Hammad, A. H. (2017). Advance deposition techniques for thin film and coating. In N. Nikitenkov (Ed.), *Modern technologies for creating the thin-film systems and coatings* (pp. 137–149). InTechOpen. <https://doi.org/10.5772/65702>
- Jordan, D. C., & Kurtz, S. R. (2013). Photovoltaic degradation rates - An analytical review. *Progress in Photovoltaics: Research and Applications*, 21(1), 12–29. <https://doi.org/10.1002/pip.1182>
- Jordan, D. C., Kurtz, S. R., VanSant, K., & Newmiller, J. (2016). Compendium of photovoltaic degradation rates. *Progress in Photovoltaics: Research and Applications*, 24(7), 978–989. <https://doi.org/10.1002/pip.2744>

- Kajari-Schröder, S., Kunze, I., & Köntges, M. (2012). Criticality of cracks in PV modules. *Energy Procedia*, 27, 658–663. <https://doi.org/10.1016/j.egypro.2012.07.125>
- Kaminski, A., Marchand, J. J., Fave, A., & Laugier, A. (1997). A new method of parameters extraction from dark I-V curve. *Conference record of the twenty sixth IEEE photovoltaic specialists conference - 1997*, 203 – 206. <https://doi.org/10.1109/PVSC.1997.654064>
- Kempe, M. D., Dameron, A. A., Moricone, T. J., & Reese, M. O. (2010). Evaluation and modeling of edge-seal materials for photovoltaic applications. *2010 35th IEEE Photovoltaic Specialists Conference*, 256-261. <https://doi.org/10.1109/pvsc.2010.5614463>
- King, D. L., Hansen, B. R., Kratochvil, J. A., & Quintana, M. A. (1997, September). Dark current-voltage measurements on photovoltaic modules as a diagnostic or manufacturing tool. *Conference Record of the Twenty Sixth IEEE Photovoltaic Specialists Conference - 1997*, 1125–1128. <https://doi.org/10.1109/pvsc.1997.654286>
- Klinkert, T. (2015). *Comprehension and optimisation of the co-evaporation deposition of Cu(In,Ga)Se₂ absorber layers for very high efficiency thin film solar cells* [Doctoral thesis, Pierre and Marie Curie University]. HAL. <https://tel.archives-ouvertes.fr/tel-01130052>
- Köntges, M., Kurtz, S., Packard, C., Jahn, U., Berger, K. A., Kato, K., Friessen, T., Liu, H., Van Iseghem, M., Wohlgemuth, J., Miller, D., Kempe, M., Hacke, P., Reil, F., Bogdanski, N., Herrmann, W., Buerhop-Luts, C., Razongles, G., & Friesen, G. (2014, March). *Performance and reliability of photovoltaic systems: Subtask 3.2: Review of failures of photovoltaic modules* (Report No. IEA-PVPS T13-01:2014). International Energy Agency - Photovoltaic Power Systems Programme. https://iea-pvps.org/wp-content/uploads/2020/01/IEA-PVPS_T13-01_2014_Review_of_Failures_of_Photovoltaic_Modules_Final.pdf
- Kuk, S., Wang, Z., Yu, H., Nam, C.-Y., Jeong, J.-H., & Hwang, D. (2019). Nanosecond laser scribing for see-through CIGS thin film solar cells. *Progress in Photovoltaics: Research and Applications*, 28(2), 135–147. <https://doi.org/10.1002/pip.3219>
- Kuntsche, J., Schuster, M., & Schneider, J. (2019). Engineering design of laminated safety glass considering the shear coupling: A review. *Glass Structures & Engineering*, 4(2), 209–228. <https://doi.org/10.1007/s40940-019-00097-3>

- Kuraray. (2022, February). *Architectural glazing: Laminated glass interlayers*. Retrieved May 4, 2022, from <https://www.trosifol.com/salessupport/downloads/product-brochures/>
- Lange, R. F. M., Luo, Y., Polo, R., & Zahnd, J. (2011). The lamination of (multi)crystalline and thin film based photovoltaic modules. *Progress in Photovoltaics: Research and Applications*, 19(2), 127–133. <https://doi.org/10.1002/pip.993>
- Lee, K., Um, H.-D., Choi, D., Park, J., Kim, N., Kim, H., & Seo, K. (2020a). The development of transparent photovoltaics. *Cell Reports Physical Science*, 1(8), Article 100143. <https://doi.org/10.1016/j.xcrp.2020.100143>
- Lee, K., Kim, N., Kim, K., Um, H.-D., Jin, W., Choi, D., Park, J., Park, K. J., Lee, S., & Seo, K. (2020b). Neutral-colored transparent crystalline silicon photovoltaics. *Joule*, 4(1), 235–246. <https://doi.org/10.1016/j.joule.2019.11.008>
- Lee, T. D., & Ebong, A. U. (2017). A review of thin film solar cell technologies and challenges. *Renewable and Sustainable Energy Reviews*, 70, 1286–1297. <https://doi.org/10.1016/j.rser.2016.12.028>
- Li, Z., Ma, T., Yang, H., Lu, L., & Wang, R. (2021). Transparent and colored solar photovoltaics for building integration. *Solar RRL*, 5(3), Article 2000614. <https://doi.org/10.1002/solr.202000614>
- Macsun Solar Energy Technology. (2016, December 14). *BIPV Solar Panel Specification*. http://www.macsunsolar.com/uploadfiles/20161214_152445.pdf
- Marion, B., Deceglie, M. G., & Silverman, T. J. (2014). Analysis of measured photovoltaic module performance for Florida, Oregon, and Colorado locations. *Solar Energy*, 110, 736–744. <https://doi.org/10.1016/j.solener.2014.10.017>
- Martín, M., Centelles, X., Solé, A., Barreneche, C., Fernández, A. I., & Cabeza, L. F. (2020). Polymeric interlayer materials for laminated glass: A review. *Construction and Building Materials*, 230, Article 116897. <https://doi.org/10.1016/j.conbuildmat.2019.116897>
- Mat Desa, M. K., Sapeai, S., Azhari, A. W., Sopian, K., Sulaiman, M. Y., Amin, N., & Zaidi, S. H. (2016). Silicon back contact solar cell configuration: A pathway towards higher efficiency. *Renewable and Sustainable Energy Reviews*, 60, 1516–1532. <https://doi.org/10.1016/j.rser.2016.03.004>

- Mavromatakis, F., Vignola, F., & Marion, B. (2017). Low irradiance losses of photovoltaic modules. *Solar Energy*, 157, 496–506. <https://doi.org/10.1016/j.solener.2017.08.062>
- Meinardi, F., Bruni, F., & Brovelli, S. (2017). Luminescent solar concentrators for building-integrated photovoltaics. *Nature Reviews Materials*, 2(12), Article 17072. <https://doi.org/10.1038/natrevmats.2017.72>
- Ministry of Business, Innovation and Employment. (2021). *Data tables for electricity* [Dataset]. <https://www.mbie.govt.nz/building-and-energy/energy-and-natural-resources/energy-statistics-and-modelling/energy-statistics/electricity-statistics/>
- Mittag, M., Vogt, L., Herzog, C., Pfreundt, A., Shahid, J., Neuhaus, D. H., & Wirth, W. (2019, September 9-13). Thermal modelling of photovoltaic modules in operation and production. *36th EU PV Solar Energy Conference and Exhibition*, 892–900. <https://doi.org/10.4229/EUPVSEC20192019-4CO.2.4>
- Novergy Energy Solutions. (n.d.). *BIPV solar panels: Detailed specifications*. Retrieved March 9, 2022, from <https://www.novergysolar.com/products/solar-panels/solar-bipv-module/>
- Novotny, M., Poot, B. (2016). Influence of temperature on laminated glass performances assembled with various interlayers. *Challenging Glass Conference Proceedings*, 5, 219–232. <https://proceedings.challengingglass.com/index.php/cgc/article/view/202/199>
https://www.novergysolar.com/wp-content/uploads/2019/09/Double_Glass_Specification-1.jpg
- NRSun. (2018a, September 18). *NRS - ASX: Amorphous silicon tandem cell (a-Si/μ-Si)*. Retrieved August 22, 2021, from <http://nrsun.eu/mt-content/uploads/2018/11/nrs-asx-amorphous-silicon.pdf>
- NRSun. (2018b, September 18). *NRS - CTT: Cadmium Telluride (CdTe)*. Retrieved August 26, 2021, from <http://nrsun.eu/mt-content/uploads/2018/11/nrs-ct-transparency.pdf>
- NSG Group. (2021, January). *Pilkington Sunplus™ BIPV*. [https://assetmanager-ws.pilkington.com/fileservlet.aspx?cmd=get_file&ref=GL062&cd=cd](https://assetmanager.ws.pilkington.com/fileservlet.aspx?cmd=get_file&ref=GL062&cd=cd)
- Ogbomo, O. O., Amalu, E. H., Ekere, N. N., & Olagbegi, P. O. (2017). A review of photovoltaic module technologies for increased performance in tropical climate. *Renewable and Sustainable Energy Reviews*, 75, 1225–1238. <https://doi.org/10.1016/j.rser.2016.11.109>
- Onyx Solar. (2021, September 15). *Onyx: Technical guide*. http://onyxsolardownloads.com/docs/ALL-YOU-NEED/Technical_Guide.pdf

- Özkalay, E., Friesen, G., Caccivio, M., Bonomo, P., Fairbrother, A., Ballif, C., & Virtuani, A. (2022). Operating temperatures and diurnal temperature variations of modules installed in open-rack and typical BIPV configurations. *IEEE Journal of Photovoltaics*, 12(1), 133–140. <https://doi.org/10.1109/JPHOTOV.2021.3114988>
- Phillips, S., Bett, A., Burger, B., Friedrich, L., Kost, C., Nold, S., Pepper, D., Preu, R., Rentsch, J., Stryi-Hipp, G., Wirth, H., & Warmuth, W. (2022, February 24). *Photovoltaics report*. Fraunhofer Institute for Solar Energy Systems. <https://www.ise.fraunhofer.de/content/dam/ise/de/documents/publications/studies/Photovoltaics-Report.pdf>
- Pingel, S., Frank, O., Winkler, M., Daryan, S., Geipel, T., Hoehne, H., & Berghold, J. (2010). Potential induced degradation of solar cells and panels. *2010 35th IEEE Photovoltaics Specialist Conference*, 2817–2822. <https://doi.org/10.1109/pvsc.2010.5616823>
- Polysolar. (2019, September 23). *PS-ASG-Series panels: STC product specifications for a-Si thin-film glass/glass laminate BIPV glazing units*. Retrieved May 13, 2022, from <https://www.polysolar.co.uk/Datasheets/PS-ASG%20Technical%20Specification%20Sheet.pdf>
- Polysolar. (2021a, March 16). *PS-MC-ST series panels: STC product specifications for c-Si monocrystalline silicon bifacial glass/glass laminate BIPV*. Retrieved August 10, 2021, from https://www.polysolar.co.uk/domestic/_domestic-info-specifications
- Polysolar. (2021b, August 9). *PS-CT series panels: STC product specifications for CdTe thin-film glass/glass laminate transparent glazing units*. Retrieved September 20, 2021, from <https://www.polysolar.co.uk/Datasheets/PS-CT-Transparent%20Technical%20Specification%20Sheet.pdf>
- Powell, R. C., Dorer, G. L., Jayamaha, U. & Hanak, J. J. (1998, September). *Technology support for initiation of high-throughput processing of thin-film CdTe PV modules: Phase III final technical report, 14 March 1997–1 April 1998* (Report No. NREL/SR-520-25422). National Renewable Energy Laboratory. <https://www.nrel.gov/docs/legosti/old/25422.pdf>
- Pujol Group. (2020). *Evalam visual UV+ & AB-AR elastic properties*. <https://www.evalam.net/en/productos/evalam-visual/>
- PVSITES. (2016, October). *BIPV market and stakeholder analysis and needs*. <https://www.pvsites.eu/downloads/download/report-bipv-market-and-stakeholder-analysis-and-ne>

- Rekow, M., Murison, R., Panarello, T., Dunsy, C., Dinkel, C., Nikumb, S., Pern, J., & Mansfield, L. (2010, October). CIGS P1, P2, P3 scribing processes using a pulse programmable industrial fiber laser. *Proceedings of the 25th European Photovoltaic Solar Energy Conference and Exhibition / 5th World Conference on Photovoltaic Energy Conversion*, 2862–2871. <https://doi.org/10.4229/25thEUPVSEC2010-3DO.5.5>
- Ritzen, M. J., Vroon, Z. A. E. P., Rovers, R., & Geurts, C. P. W. (2017). Comparative performance assessment of a non-ventilated and ventilated BIPV rooftop configurations in the Netherlands. *Solar Energy*, 146, 389–400. <https://doi.org/10.1016/j.solener.2017.02.042>
- Roberts, S., & Guariento, N. (2009). *Building integrated photovoltaics: A handbook*. Birkhäuser. <https://doi.org/10.1007/978-3-0346-0486-4>
- Romeo, A., & Artegiani, E. (2021). CdTe-based thin film solar cells: Past, present and future. *Energies*, 14(6), Article 1684. <https://doi.org/10.3390/en14061684>
- Rowell, M. W., Daroczi, S. G., Harwood, D. W. J., & Gabor, A. M. (2018). The effect of laminate construction and temperature cycling on the fracture strength and performance of encapsulated solar cells. *2018 IEEE 7th World Conference on Photovoltaic Energy Conversion (WCPEC)(A Joint Conference of 45th IEEE PVSC, 28th PVSEC & 34th EU PVSEC)*, 3927–3931. <https://doi.org/10.1109/pvsc.2018.8547978>
- Rose, D. H., & Powell, R. C. (2002). *Technology support for high-throughput processing of thin-film CdTe PV modules: Final technical report, April 1998—October 2001* (Report No. NREL/SR-520-32041). National Renewable Energy Laboratory. <https://www.nrel.gov/docs/fy02osti/32041.pdf>
- Ruike New Energy. (n.d.). *Products and Technology*. Retrieved November 11, 2021, from <http://www.rksolar.com.cn/en/h-col-136.html>
- Sai, H., Matsui, T., Kumagi, H., & Matsubura, K. (2018). Thin-film microcrystalline silicon solar cells: 11.9% efficiency and beyond. *Applied Physics Express* 11(2), Article 022301. <https://doi.org/10.7567/APEX.11.022301>
- Sample, T., & Virtuani, A. (2009). Modification to the standard reference environment (SRE) for nominal cell temperature (NOCT) to account for building integration. *Proceedings of the 24th European Photovoltaic Solar Energy Conference*. 3332–3337. <https://doi.org/10.4229/24thEUPVSEC2009-4AV.3.13>

- Satpathy, R. K., & Pamuru, V. (2020). *Solar PV power: Design, manufacturing and applications from sand to systems*. Academic Press. <https://doi.org/10.1016/C2018-0-02530-X>
- Schmitt, J. (1989). *Plasma-assisted method for thin-film fabrication*. (U.S. Patent No. 4,798,739). United States Patent and Trademark Office. <https://patents.google.com/patent/US4798739A/en?q=US+4%2c798%2c739>
- Schneller, E. J., Brooker, R. P., Shiradkar, N. S., Rodgers, M. P., Dhere, N. G., Davis, K. O., Seigneur, H. P., Mohajeri, N., Wohlgemuth, J., Scardera, G., Rudack, A. C., & Schoenfeld, W. V. (2016). Manufacturing metrology for c-Si module reliability and durability part III: Module manufacturing. *Renewable and Sustainable Energy Reviews*, 59, 992–1016. <https://doi.org/10.1016/j.rser.2015.12.215>
- Shin, H., Han, E., Park, N., & Kim, D. (2018). Thermal residual stress analysis of soldering and lamination processes for fabrication of crystalline silicon photovoltaic modules. *Energies*, 11(12), Article 3256. <https://doi.org/10.3390/en11123256>
- Sidali, T., Bou, A., Coutancier, D., Chassaing, E., Theys, B., Barakel, D., Garuz, R., Thoulon, P.-Y., & Lincot, D. (2018). Semi-transparent photovoltaic glazing based on electrodeposited CIGS solar cells on patterned molybdenum/glass substrates. *EPJ Photovoltaics*, 9, Article 2. <https://doi.org/10.1051/epjpv/2017009>
- Sinha, A., Sulas-Kern, D. B., Owen-Bellini, M., Spinella, L., Uličná, S., Ayala Pelaez, S., Johnston, S., & Schelhas, L. T. (2021). Glass/glass photovoltaic module reliability and degradation: A review. *Journal of Physics D: Applied Physics*, 54(41), Article 413002. <https://doi.org/10.1088/1361-6463/ac1462>
- Smith, B. L., Woodhouse, M., Horowitz, K. A. W., Silverman, T. J., Zuboy, J., Margolis, R. M. (2021, November). *Photovoltaic (PV) module technologies: 2020 benchmark costs and technology evolution framework results* (Report No. NREL/TP-7A40-78173). National Renewable Energy Laboratory. <https://www.nrel.gov/docs/fy22osti/78173.pdf>
- Solitec. (2021, August 15). *Solid pro 54 cell: Glass/glass frameless*. https://www.solitec.eu/storage/app/media/M54_285W_Solid_Pro_Transparency_25.pdf
- Song, W. J. R., Tippabhotla, S. L., Tay, A. A. O., & Budiman, A. S. (2018). Effect of interconnect geometry on the evolution of stresses in solar photovoltaic laminate during and after lamination. *Solar Energy Materials and Solar Cells*, 187, 241–248. <https://doi.org/10.1016/j.solmat.2018.07.026>

- Spataru, S. V., Sera, D., Hacke, P., Kerekes, T., & Teodorescu, R. (2015). Fault identification in crystalline silicon PV modules by complementary analysis of the light and dark current–voltage characteristics. *Progress in Photovoltaics: Research and Applications*, 24(4), 517–532. <https://doi.org/10.1002/pip.2571>
- Stadler, A. (2012). Transparent conducting oxides—An up-to-date overview. *Materials*, 5(12), 661–683. <https://doi.org/10.3390/ma5040661>
- Standards New Zealand. (2008). *Glazing in buildings - Part 1: Glass selection and glazing* (NZS 4223.1:2008). <https://www.standards.govt.nz/>
- Suckow, S. (2014). *2/3-Diode Fit*. <http://nanohub.org/resources/14300>
- Sulkis, M. C. (2019). *Characterization of encapsulant and edge seal materials for flexible solar cell packaging* [Master's thesis, Georgia Institute of Technology]. Georgia Tech Library. <http://hdl.handle.net/1853/61307>
- Takeoka, A., Kouzuma, S., Tanaka, H., Inoue, H., Murata, K., Morizane, M., Nakamura, N., Nishiwaki, H., Ohnishi, M., Nakano, S., & Kuwano, Y. (1993). Development and application of see-through a-Si solar cells. *Solar Energy Materials and Solar Cells*, 29(3), 243–252. [https://doi.org/10.1016/0927-0248\(93\)90039-6](https://doi.org/10.1016/0927-0248(93)90039-6)
- United Nations Environment Programme. (2021, October 19). *2021 global status report for buildings and construction: Towards a zero-emissions, efficient and resilient buildings and construction sector*. <https://www.unep.org/resources/report/2021-global-status-report-buildings-and-construction>
- United Nations Framework Convention of Climate Change. (2016, January 29). *Report of the conference of the parties on its twenty-first session, held in Paris from 30 November to 13 December 2015: Part two: Action taken by the conference of the parties at its twenty-first session* (Report No. FCCC/CP/2015/10/Add.1). <https://unfccc.int/resource/docs/2015/cop21/eng/10a01.pdf#page=2>
- Vieira, R. G., de Araújo, F. M. U., Dhimish, M., & Guerra, M. I. S. (2020). A comprehensive review on bypass diode application on photovoltaic modules. *Energies* 13(10), Article 2472. <https://doi.org/10.3390/en13102472>
- Virtuani, A., Pavanello, D., & Friesen, G. (2010). Overview of temperature coefficients of different thin film photovoltaic technologies. *25th European Photovoltaic Solar Energy Conference and Exhibition / 5th World Conference on Photovoltaic Energy Conversion*, 4246–4254. <https://doi.org/10.4229/25thEUPVSEC2010-4AV.3.83>

- Weihai China Glass Solar. (n.d.). *Transparent solar module*. Retrieved March 9, 2022, from <http://www.cgsolar.com/en/ProductInfo.asp?id=34>
- Wilson, G. M., Al-Jassim, M., Metzger, W. K., Glunz, S. W., Verlinden, P., Xiong, G., Mansfield, L. M., Stanberry, B. J., Zhu, K., Yan, Y., Berry, J. J., Ptak, A. J., Dimroth, F., Kayes, B. M., Tamboli, A. C., Peibst, R., Catchpole, K., Reese, M. O., Klinga, C. S., ... Sulas-Kern, D. B. (2020). The 2020 photovoltaic technologies roadmap. *Journal of Physics D: Applied Physics*, 53(49), Article 493001. <https://doi.org/10.1088/1361-6463/ab9c6a>
- Woodhouse, M. A., Smith, B., Ramdas, A., & Margolis, R. M. (2019). *Crystalline silicon photovoltaic module manufacturing costs and sustainable pricing: 1H 2018 benchmark and cost reduction road map* (Report No. NREL/TP-6A20-72134). National Renewable Energy Lab. <https://doi.org/10.2172/1495719>
- Yang, C., Liu, D., Bates, M., Barr, M. C., & Lunt, R. R. (2019). How to accurately report transparent solar cells. *Joule*, 3(8), 1803–1809. <https://doi.org/10.1016/j.joule.2019.06.005>
- Yeop Myong, S., & Won Jeon, s. (2015). Design of esthetic color for thin-film silicon semi-transparent photovoltaic modules. *Solar Energy Materials and Solar Cells*, 143, 422–449. <https://doi.org/10.1016/j.solmat.2015.07.042>
- Zanetti, I., Bonomo, P., Frontini, F., Saretta, E., van den Donker, M., Vossen, F., & Folkerts, W. (2017). *Building integrated photovoltaics: Product overview for solar buildings skins: Status report 2017*. SUPSI - SEAC. <https://resources.solarbusinesshub.com/images/reports/179.pdf>
- Zhang, J., Liu, Y., Ding, K., Feng, L., Hamelmann, F. U., & Chen, X. (2020). Model parameter analysis of cracked photovoltaic module under outdoor conditions. *2020 47th IEEE Photovoltaic Specialists Conference (PVSC)*, 2509–2512. <https://doi.org/10.1109/PVSC45281.2020.9300720>
- Zhang, Y., Samuel, I. D. W., Wang, T., & Lidzey, D. G. (2018). Current status of outdoor lifetime testing of organic photovoltaics. *Advanced Science*, 5(8), Article 1800434. <https://doi.org/10.1002/advs.201800434>

A Market Analysis and Product Overview

An extensive analysis of glass-glass STPV products was conducted to evaluate the technologies and levels of performance currently available, to extract comparable data opaque and coloured products were excluded. The manufacturers of such modules were found using an online database (ENF Solar, n.d.) dedicated to documenting photovoltaic manufacturers and products in the PV industry.

Around 200 companies listed as STPV manufacturers, (about 150 c-Si and 50 thin-film), were analysed with those providing sufficiently detailed datasheets being selected, a small portion of the devices included may not be structurally suitable for BIPV usage however they have almost indistinguishable differences in terms of transparency and PCE.





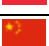





Manufacturer		Technology	Source
Advanced Solar Power		CdTe	(Advanced Solar Power, 2020)
Aleo Solar		Mono c-Si	(Aleo Solar, 2020)
Almaden Morocco		Mono c-Si	(Almaden Morocco, 2021)
Antec Solar		CdTe	(Antec Solar, 2014)
Baoding Jiasheng Photovoltaic Technology		Poly c-Si	(Baoding Jiasheng Photovoltaic Technology, 2021)
BISOL Group		Mono c-Si	(BISOL Group, 2021)
Ertex Solar		Mono & Poly c-Si	(Ertex Solartechnik, n.d.)
Macsun Solar Energy Technology		Mono c-Si	(Macsun Solar Energy Technology, 2016)
Novergy Energy Solutions		Mono & Poly c-Si	(Novergy Energy Solutions, n.d.)
NRSun		CdTe & Micromorph	(NRSun, 2018a & 2018b)
Onyx Solar		Mono c-Si & a-Si	(Onyx Solar, 2020)
Polysolar		c-Si, CdTe & a-Si	(Polysolar, 2019, 2021a & 2021b)
Ruike New Energy		CdTe	(Ruike New Energy, n.d.)
Solitek		Mono c-Si	(Solitek, 2021)
Sonnenstromfabrik		Mono c-Si	(CS Wismar, 2020)
Weihai China Glass Solar		a-Si	(Weihai China Glass Solar, n.d.)

Table 21: Commercial semi-transparent PV module manufacturers

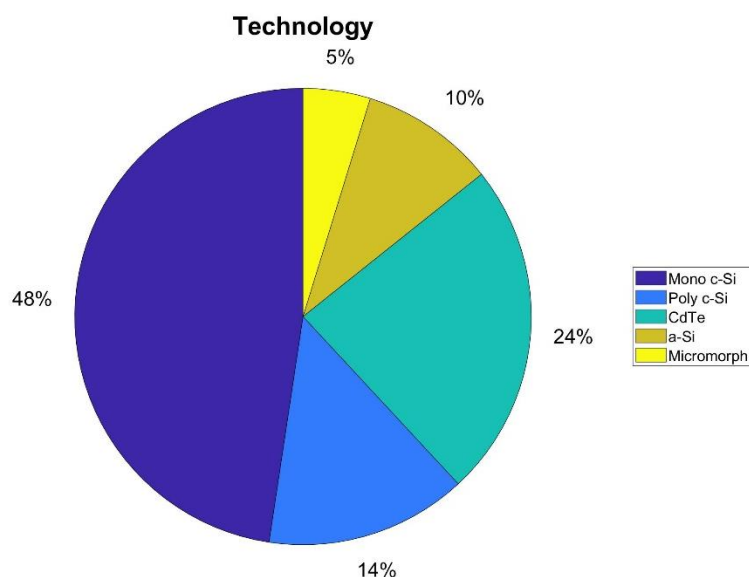


Figure 62: PV technologies used in commercial STPV products (Table 21)

Even with such a small sample size the percentage of products using c-Si cells (62%), (combined mono- and poly-silicon in Figure 62), aligns well with the predicted BIPV market shares for this technology. CdTe was the most popular thin-film material as should be expected due to its low manufacturing cost and relatively high efficiencies. The absence of CIGS products is also expected, due to the difficulties in P4 scribing

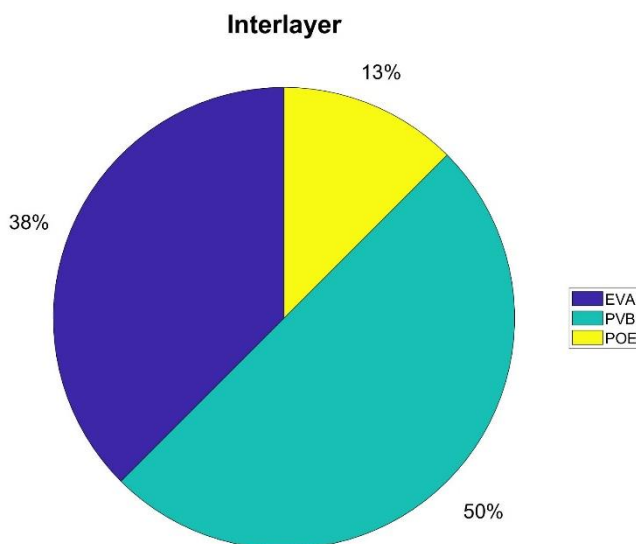


Figure 63: Interlayer materials used in commercial STPV products (Table 21)

Some products were offered with multiple interlayer options which in almost all cases was a choice between PVB or EVA as graphed in Figure 63, this is probably to account for differences in humidity for different climates, in which an EVA is more suitable due to the lower moisture permeation. POE was used in a few crystalline products and the majority of these products guaranteed much lower degradation rates. It is worth noting that not all transparent PV products

analysed are suitable for BIPV, and interlayer properties required for rack-mounted glass-glass PV may be less than a BIPV product.

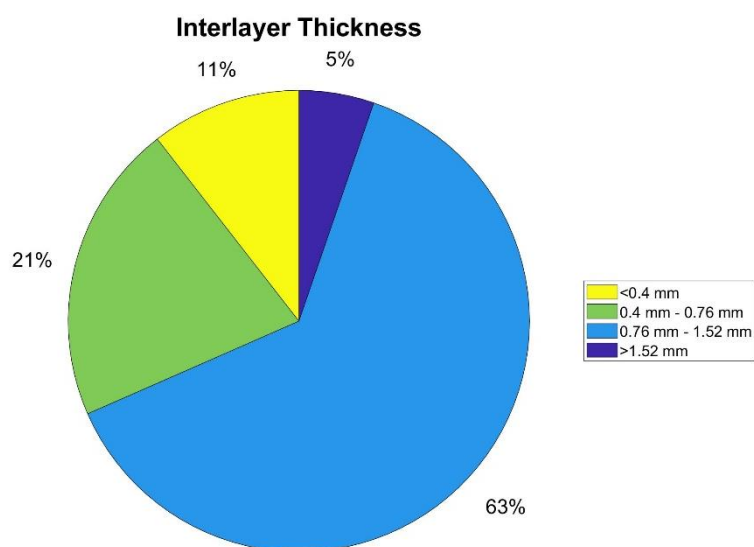


Figure 64: Interlayer thicknesses in commercial STPV product (Table 21)

The majority of products used an interlayer thickness between 0.76 mm and 1.52 mm (Refer to Figure 64 above), which corresponds to 2 or 4 layers of standard PVB foil (0.38 mm). For thin-film modules only the typical thicknesses corresponded to 1 – 2 layers of encapsulant while almost all crystalline modules used 4 layers of encapsulant.

B Laminated Glass Modelling

As discussed in Chapter 2.2.2 when a load is applied to a laminated glass sheet some partial degree of shear transfer occurs, in which stresses developed in one glass sheet are transferred through the interlayer into the other sheet.

Commonly a shear transfer coefficient is used to describe the degree of shear transfer, where a value of 1 indicates full transfer (monolithic limit) and 0 means no transfer occurs (layered limit). The coefficient is dependent on a number of parameters such as load type and glass dimensions but is most heavily influenced by the time-temperature dependent shear stiffness $G(T,t)$ of the interlayer material.

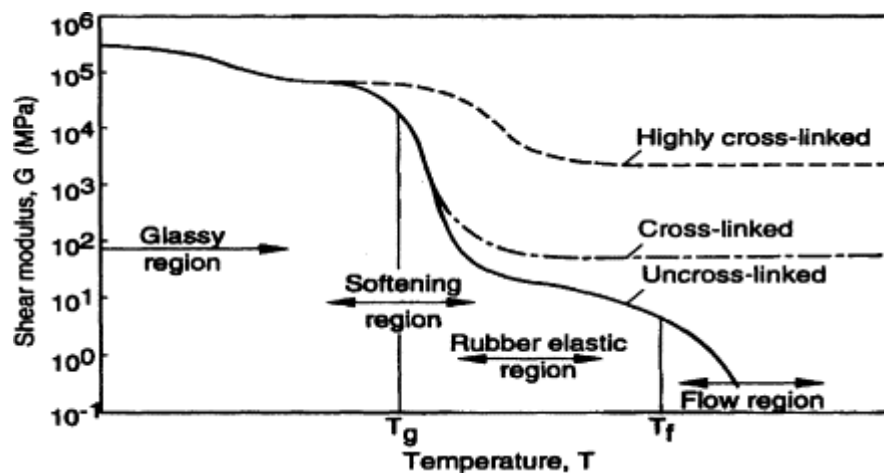


Figure 65: Polymer stiffness dependence on temperature

This is of particular interest for the design of glass-glass BIPV as the solar absorptance of PV cells leads to higher temperatures than in typical glazings, causing heating of the interlayer and therefore lower laminate stiffness. This is one of the main structural performance differences between BIPV products and their equivalent traditional glazings they intend to replace, design processes for BIPV must consider much higher operating conditions in order to correctly specify laminated glass thicknesses.

For the purpose of calculating laminate behaviour under static loading the Wölfel-Bennison effective thickness model is utilized. This model compensates for the interlayer behaviour by calculating an effective thickness of monolithic glass which represents the laminates structural behaviour based on the dimensions and interlayer properties under a given loading condition. This relation assumes that only small strains are considered which is a suitable simplification in the case of non-fractured laminates. Another simplification specifically for PV laminates is ignoring the small increase to bending stiffness arising from the introduction of the PV cells and interconnects, and the shear transfer from the glass to the cells.

The model and equations defining the shear coefficient and effective thicknesses are reproduced from the work of Wölfel (1987, as cited in Kuntsche et al., 2019). The application of this effective thickness model has extended into certain national glass standards for design specification and is especially useful for stiffer interlayers such as Ionomer where standard non-shear calculations would give exceedingly conservative results leading to unnecessarily thick and costly glass laminates. For the purpose of all calculations presented the following assumptions and values are used:

Property	Value	Justification
Glass Elastic Modulus (E)	70 GPa	NZS 4223-1:2008 Clause 2.1.5
Glass thickness (d)	3.8 mm	Minimum thickness for 4 mm nominal glass
Interlayer thickness (d_Q)	1.52 mm	Design thickness used in PV prototypes
Glass laminate span (a)	1000 mm	Arbitrary medium sized glazing
Loading case coefficient	9.6	As specified for UDL in Kuntsche et al (2019)
Interlayer shear stiffness	Variable	Taken from G(T,t) tabulated manufacturer data

Table 22: Variable and values used in shear bonding calculations

$$K = \frac{A E d * d_Q}{2 G a^2} \quad (B.1)$$

$$W = \frac{1}{K + 1} \quad (B.2)$$

$$d_\delta = \sqrt[3]{2d^3 + 6dW(d_Q + d)^2} \quad (B.3)$$

$$d_\sigma = \sqrt{\frac{2d^3 + 6dW(d_Q + d)^2}{d + W(d_Q + d)}} \quad (B.4)$$

$$\sigma_{eff} = \frac{3w_{UDL} * a^2}{4d_\sigma^2} \quad (B.5)$$

The area of interest is the laminate behaviour at about 50 – 60 °C which is the expected maximum temperature range for vertical BIPV with ventilation, short load durations are investigated (3 seconds) because they are more likely to occur in conjunction with high temperatures due to gusts of wind etc, whereas sustained wind loads would lower temperatures due to convective cooling. Also the shear stiffness of highly crosslinked polymers tends to drop of rapidly and plateau (See both Figure 65 and Figure 66), meaning that calculations at longer

loads and higher temperatures do not reveal additional information. Results of this analysis summarised in Figure 67, Figure 68 and Figure 69 indicate that the increased temperature due to solar absorption of embedded PV cells has a significant impact on the mechanical properties of the photovoltaic laminate, with stresses in glass plies reaching 30-40% higher at around 50°C compared to room temperature.

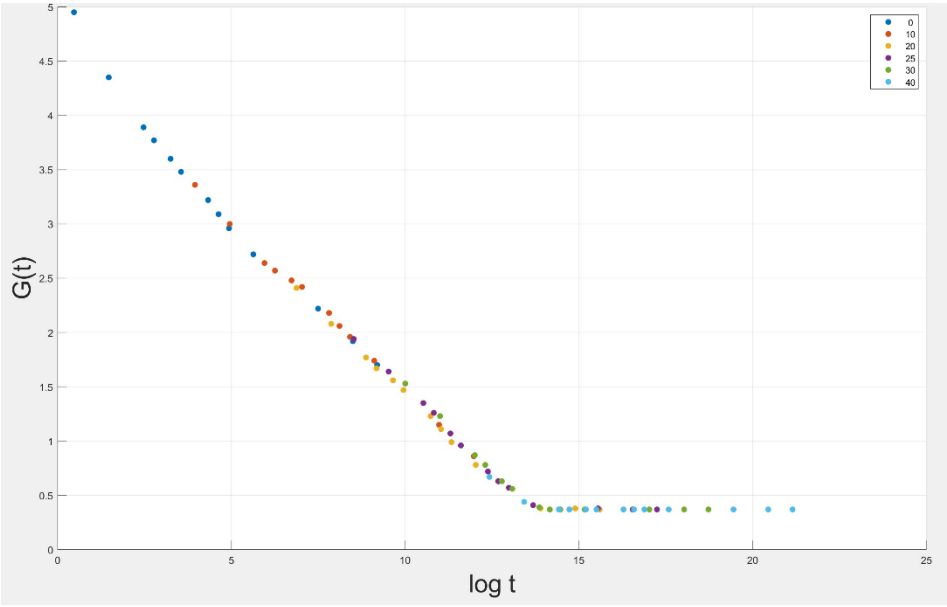


Figure 66: Shear modulus master curve for EVALAM Visual UV+

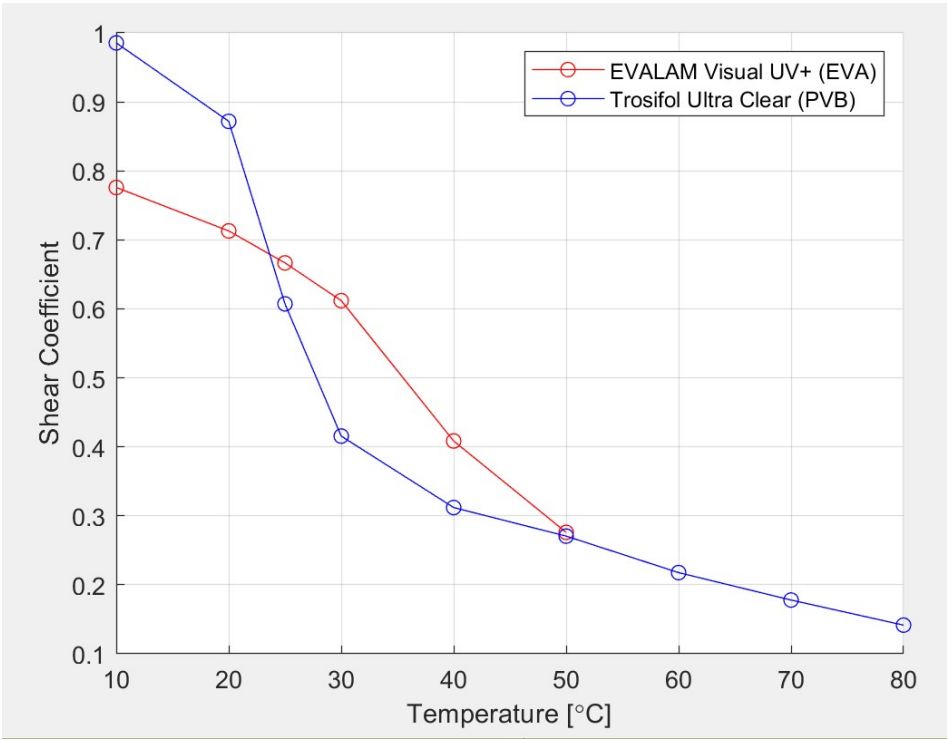


Figure 67: Shear coefficient vs temperature

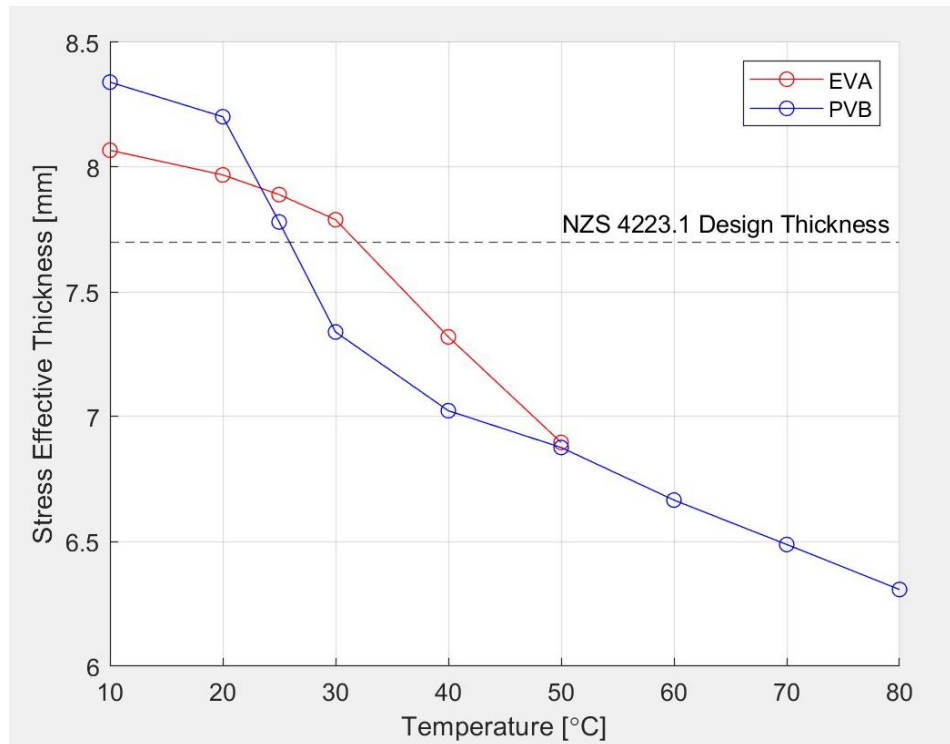


Figure 68: Stress effective thickness vs temperature

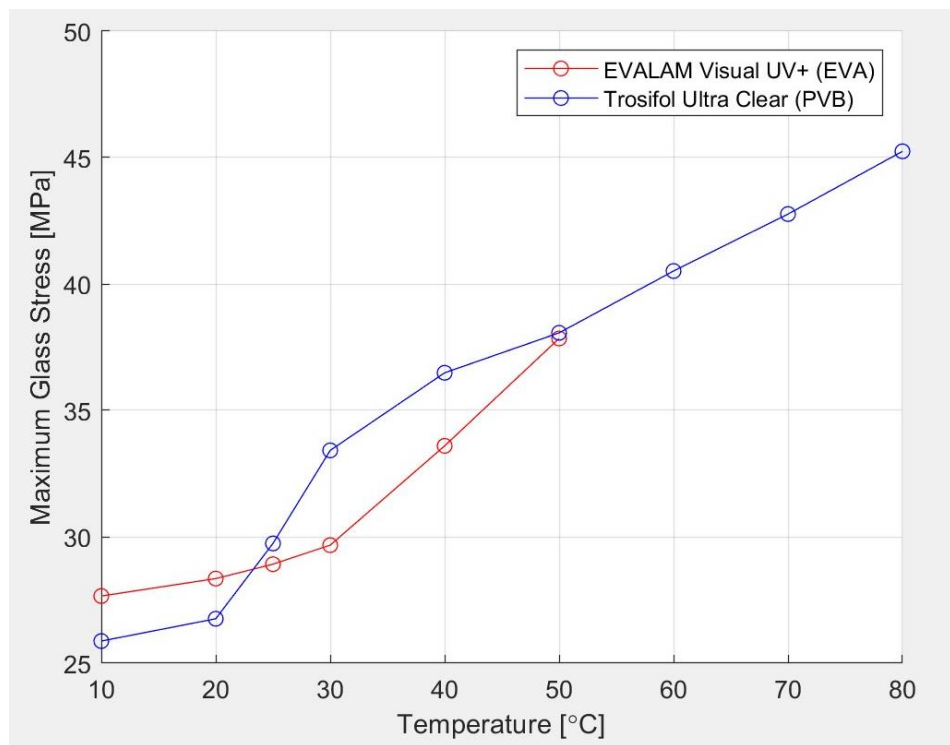


Figure 69: Maximum glass stress vs temperature

C Cell Characterization Results

Parameter	D12-T	D14-T	D21-T	D22-T	D23-T	D24-T
Initial R_s	14.85 m Ω	14.20 m Ω	12.11 m Ω	12.39 m Ω	11.93 m Ω	12.28 m Ω
Final R_s	13.54 m Ω	13.18 m Ω	--	13.43 m Ω	13.76 m Ω	13.64 m Ω
ΔR_s	-8.83 %	-7.16 %	--	+8.34 %	15.34 %	11.10 %
Initial R_{sh}	5006.0 Ω	3010.6 Ω	4928.6 Ω	8431.2 Ω	2285.3 Ω	1680.4 Ω
Final R_{sh}	627.2 Ω	285.8 Ω	540.9 Ω	404.9 Ω	466.0 Ω	618.1 Ω
ΔR_{sh}	-87.47 %	-90.51 %	-89.02 %	-95.20 %	-79.61 %	-63.22 %
Initial I_{O2}	7.42 x 10 ⁻⁶	1.31 x 10 ⁻⁵	2.09 x 10 ⁻⁵	3.29 x 10 ⁻⁵	3.66 x 10 ⁻⁵	2.99 x 10 ⁻⁵
Final I_{O2}	2.88 x 10 ⁻⁵	4.30 x 10 ⁻⁵	--	5.65 x 10 ⁻⁵	4.35 x 10 ⁻⁵	4.41 x 10 ⁻⁵
ΔI_{O2}	+288.0 %	+228.4 %	--	+71.55 %	+18.65 %	+47.32 %
Initial n_2	1.874	1.812	2.015	1.985	2.003	1.971
Final n_2	2.017	2.047	--	2.120	2.051	2.056
Δn_2	+7.66 %	+12.95%	--	+6.81 %	+2.39 %	+4.27 %
Initial I_{O1}	2.18 x 10 ⁻¹⁰	4.93 x 10 ⁻¹¹	1.81 x 10 ⁻¹⁰	8.89 x 10 ⁻¹¹	4.85 x 10 ⁻¹¹	4.35 x 10 ⁻¹¹
Final I_{O1}	4.74 x 10 ⁻¹¹	6.00 x 10 ⁻¹¹	--	5.38 x 10 ⁻¹¹	6.26 x 10 ⁻¹¹	5.84 x 10 ⁻¹¹
ΔI_{O1}	-78.26 %	+21.52 %	--	-39.46 %	+29.13 %	+34.40 %
Initial n_1	1.003	1.001	1.000	1.041	1.013	1.000
Final n_1	1.000	1.007	--	1.000	1.003	1.000
Δn_1	-0.29 %	-0.60 %	--	-3.94 %	-0.96%	0.00 %

Table 23: Complete cell characterization results